Doctoral Thesis

Synthesis, Characterization and Catalytic Investigations of Pt-Based Binary (Bimetallic) and Ternary (Trimetallic) Nanoparticles

---

A Thesis Presented to the

Faculty of Engineering and the Built Environment
University of Cape Town

and

Faculty of Science and Engineering
Macquarie University (Sydney, Australia)

In Fulfilment of the Requirements of the
Degree of Doctor of Philosophy

By

Gerard Malefane Leteba

Supervisors: Prof. Candace Lang

Dr. Pieter Levecque

Declaration

I know the meaning of plagiarism and declare that all of the work in the thesis document, save for that which is properly acknowledged, is my own both in concept and execution, apart from the customary assistance from my supervisors.

I hereby declare that I wrote this document myself with the help of no more than the mentioned literature and ancillary means.

Up to this point, this document was not published or presented to any other examinations office in the same or similar form.

Signed by candidate

12/04/2016

Gerard Leteba **Date**

Abstract

This work tests the hypothesis that nanoparticles of 75 at.% platinum (Pt) composition and anisotropic morphology, will outperform standard catalysts in (PEMFC) hydrogen fuel cells. A survey of the scientific literature on this topic is first presented. The synthetic strategies which were developed for the preparation of novel Pt-based binary (bimetallic) and ternary (trimetallic) nanoparticles, containing nickel (Ni), cobalt (Co) and/or vanadium (V), are then described. The synthesis protocols for solution-grown colloidal nanoparticles all required the heat-up of a chemical mixture (of metal precursors, surfactants as stabilizers, solvents and/or reductants) from room temperature to high temperatures (up to 310 °C), for thermal decomposition or thermal co-reduction. These protocols were successful in producing nanostructures of high quality, with exceptional solubility in polar solvents such as chloroform after repeated washing and drying. Detailed microstructural investigations of the synthesized nanoparticles were carried out using scanning transmission electron microscopy (STEM), TEM and X-ray diffraction (XRD). The nanoparticles were anisotropic with composition around 75 at.% Pt. Depending on the particular synthesis protocol, the as-prepared nanoparticles exhibited different morphologies, surface facets, size and structure (alloy or core-shell).

To measure the oxygen reduction reaction (ORR) functionality of these nanoparticles, electrochemical measurements were conducted, including cyclic voltammetry (CV), carbon monoxide stripping voltammetry (CO-stripping) and rotating disk electrode measurements (RDE). These measurements determined (a) electrochemical surface area, (b) mass-specific activity and (c) area-specific activity; which were used to compare the performance of the synthesized nanoparticles with the performance of a standard catalyst. The synthesised nanoparticles, containing 75 at.% Pt and having anisotropic morphologies, exhibited better catalytic functionality than the standard catalysts currently in widespread use. The enhanced functionality of these alloy nanostructures is attributed to their anisotropic nature and structure (mixed or core-shell). It is shown accordingly that high surface area nanoparticles, with platinum composition around 75 at.%, are more effective than the best catalysts currently in use. Subsequently, electrochemical measurements were used to determine longevity: catalytic functionality was measured after cycling for considerably longer than the norm in nanoparticle research (5000 cycles). These measurements show a decay in catalytic activity after prolonged potential cycles, although the final value is similar to the initial value for commercial Pt catalyst. This decay is suggestive of alloying dissolution and surface facet deformation; further work is recommended.

Acknowledgements

The following work was accomplished under the supervision of Prof. Candace Lang (Macquarie University, Australia) and Dr. Pieter Levecque (University of Cape Town, South Africa).

First and foremost, my wholehearted gratitude goes to my supervisors, Prof. Candace Lang and Dr. Pieter Levecque, for their tremendous supervision, encouragement and infinite support throughout the path of my all-inclusive studies. The freedom they gave me to explore and pursue my own research ideas is genuinely appreciated. These distinct experiences have not only greatly augmented my university career, but have also established a platform for my future career.

I express my special and deepest thanks to Prof. Candace Lang for giving me an opportunity to pursue my research studies overseas. Her indulgent support and encouragement have contributed a lot more in sustaining my work ethic toward achieving my career mission statement. I thank her and Mr. Daniel McGill for uncountable scientific and sundry friendly discussions.

Special thanks to Mr. Mohammed Jaffer for an illuminating introduction to transmission electron microscopy (TEM) at the University of Cape Town and Dr. David Mitchell from the Centre for Electron Microscopy at the University of Wollongong, Australia, for his high resolution STEM (HR-STEM) meritorious expertise and assistance. I wish to extend my special appreciation to Dr. David Mitchell for the wonderful scientific and many pleasant discussions.

Most importantly, I would also like to extend my huge thanks to Cotutelle International Macquarie University Research Excellence Scholarship (iMQRES), Canon Collins Educational and Legal Assistance Trust and HySA (Hydrogen South Africa) for their generous financial support.

I also wish to express my gratitude for my fellow colleagues and members of the Centre for Materials Engineering, namely Mrs. Penny Park-Ross (University of Cape Town) for her far-reaching scientific contributions, Nicholas Tse and Wendy Tao (Macquarie University) for their incredible hospitality at the inception of my stay in Sydney and for their incredible assistance with various experimental aspects of the research work. Most importantly, Helen Xu for her exceptional assistance with XRD measurements.

Table of Contents

CHAPTER 1 INTRODUCTION

The combustion of fossil fuels reduces a finite resource and also creates environmental and health concerns. Within the energy industry, a core research drive is to discover ways of reducing both depletion of fossil fuels and atmospheric pollution emissions, while also meeting escalating energy demands[1-4]. The development of proton exchange membrane fuel cells (PEMFCs), which generate power by converting hydrogen fuel energy directly into electricity, provides an alternative, clean source of energy[1, 4, 5]. PEMFCs rely extensively on platinum (Pt) nanoparticles as a standard catalyst; however the high cost of Pt is a barrier to the widespread commercialization of PEMFCs. A principal research drive is therefore to increase the cost efficiency of catalyst nanoparticles by alloying platinum with other, cheaper, metals. Effort has accordingly been directed towards the design and engineering of novel binary (bimetallic) and ternary (trimetallic) Pt-based nanoparticles, but good control over composition and surface properties remains elusive.

In the present work, nanoalloys (Pt with other metals) and their synthesis has been systematically explored with the intention of developing a robust, repeatable route to formation of optimal nanoparticles for PEMFC catalysis. In the following sections, an overview is given of PEMFCs, electrodes and electrocatalysts, and the design of Pt contact electrocatalysts for the oxygen reduction reaction (ORR). More detail appears in Chapter 2. This introductory chapter ends with delineation of the Research Hypothesis and the Research Objectives of this project.

1.1 Proton Exchange Membrane Fuel Cells (PEMFCs)

The most promising efforts at clean energy production are directed toward the development of PEMFC technology[6-8]. PEMFCs, based on hydrogen fuel utilization to power automotive, stationary and portable devices, meet the fundamental requirements for energy sources that are cleaner and more efficient than those currently in widespread use. A fuel cell is an electrochemical device that operates as a continuous flow system into which the fuel, hydrogen (H_2) and the oxidant, oxygen (O_2) are continuously fed and electricity is continuously generated, as shown in Figure 1.1[9].

The two catalytic electrodes (anode and cathode) of the PEMFC are separated by an electrolyte known as the proton exchange membrane (PEM). The PEM supports the electrocatalysts, carried on carbon, required to facilitate the necessary redox electrochemistry. It also serves as an electrical insulator, permitting only positively charged ions (protons) to pass through it from anode (-), to cathode (+). The negatively charged electrons are forced to travel along an external circuit from the anode to the cathode, thereby generating electricity in the form of current. The PEM also acts as a physical barrier to suppress the mixing of the fuel and the oxidant[1, 3, 4, 9].

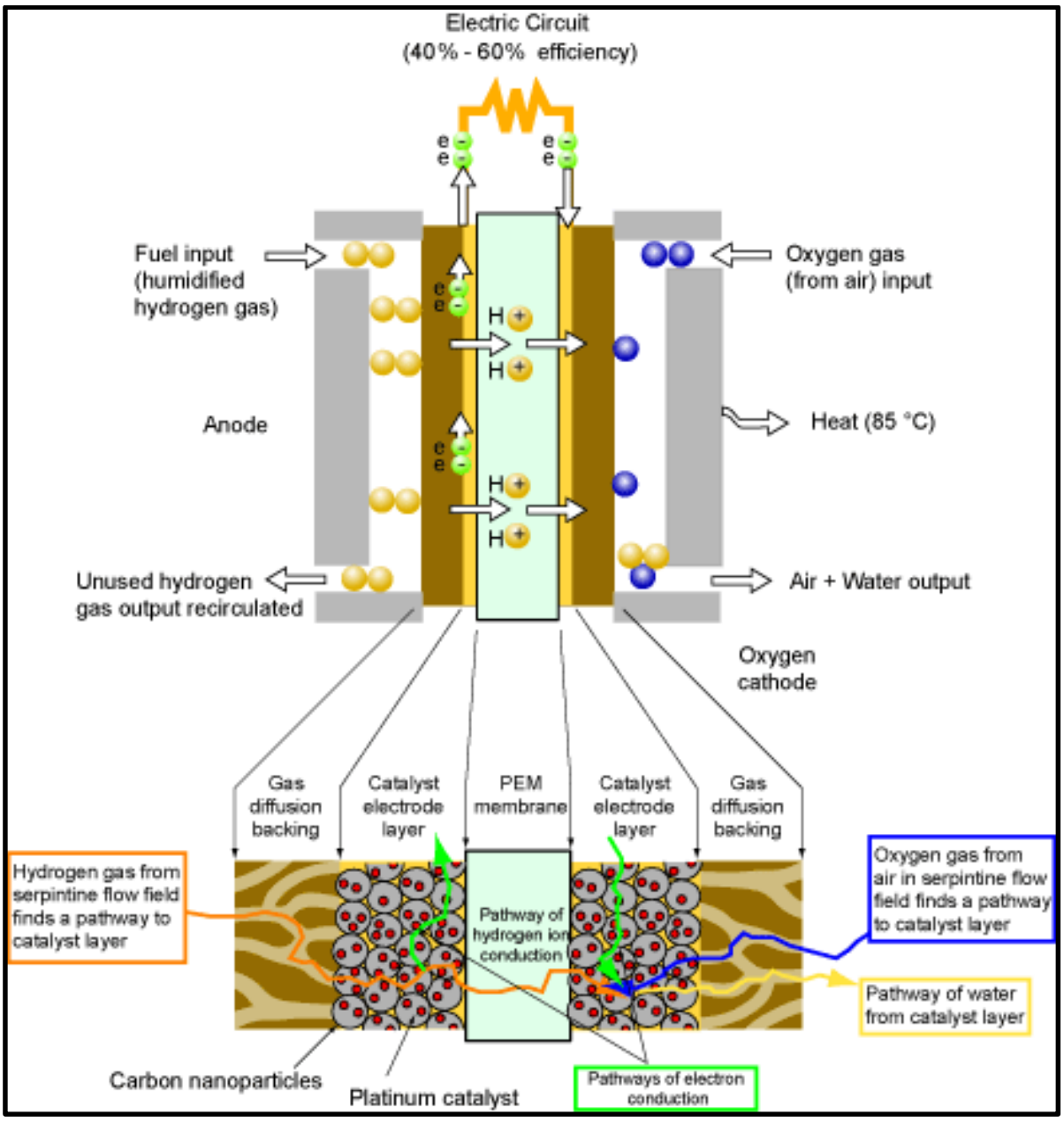

Figure 1.1: Diagram of a proton exchange membrane (PEM) hydrogen fuel cell principle (after NIST)[9].

The PEMFC reactants (H_2 and O_2) are supplied from external sources and electricity is produced for as long as fuel is supplied. Fuel cells thus have a constant feed of fresh reactants into the cell and potentially an unlimited lifetime. Since the by-products of the fuel cell are water (H_2O) and excess (waste) heat, PEMFCs hold the prospect of harnessing power devoid of greenhouse gas emissions, provided that the hydrogen fuel consumed is generated in a 'clean' manner[1, 3]. The development of PEMFCs as electrical current generators thus has the potential to play a key role in a future 'hydrogen economy'. Functioning effectively, fuel cells can extract more energy from fuel (40-60% efficiency) than traditional internal combustion engines (~30%)[1].

Perhaps the most interesting characteristic of the fuel cell is that its thermodynamic efficiency is not limited by the Carnot cycle (the ratio between useful energy output and energy input), unlike combustion engines such as steam and gas turbines, because power is generated through a chemical process. Instead, the efficiency of the hydrogen fuel cell is directly related to the overpotential, the difference between the thermodynamically predicted (prescribed) voltage and the experimental voltage achieved, of the simultaneous half-reactions at each electrode[4].

1.2 Electrode Reactions in the PEMFC

The predominant reactions occurring at the anode and cathode of the PEMFC are the hydrogen oxidation reaction (HOR) and the oxygen reduction reaction (ORR), respectively. In a conventional PEMFC at ambient temperatures, the reaction kinetics at the anode and cathode are different: the ORR kinetics are sluggish in comparison to the HOR. State-of-the-art anode and cathode electrocatalysts for PEMFCs are Pt or Pt alloy nanoparticles carried on high surface area carbon supports[4, 5, 10]. Pure Pt nanoparticles are currently the best electrocatalysts for both anode and cathode reactions, facilitating the following reactions[4, 11]:

Anode HOR: $H_{2\,(g)} \rightarrow 2H^+ + 2e^-$ $E° = 0$ V vs. SHE (Standard Hydrogen Electrode)

Cathode ORR: $\frac{1}{2}O_{2\,(g)} + 2H^+ + 2e^- \rightarrow H_2O_{\,(l)}$ $E° = 1.23$ V vs. SHE

This process involves the splitting of hydrogen gas molecules into protons (H^+) and electrons (e^-). The protons diffuse through the PEM to the cathode whereas the liberated electrons flow

through the external circuit to the cathode, creating an electric current. At the cathode, oxygen is reduced and combines with the protons and electrons donated by oxidized hydrogen to form water[4, 11].

The overall reaction, $E_{cell} = E_{cathode} - E_{anode}$, of these two simultaneous half-reactions at 25°C and standard atmospheric pressure is given by[4]:

Net reaction: $H_{2\,(g)} + \frac{1}{2}O_{2\,(g)} \rightarrow H_2O_{\,(l)}$ $E° = 1.23$ V vs. SHE

The net cell reaction is the spontaneous formation of water, heat and electricity from the HOR and ORR. The contribution of protons (H^+) in both anodic and cathodic reactions compels the PEMFCs to operate in an acidic environment (medium)[4, 11]. The net PEMFC reaction is similar to the exothermic reaction process of hydrogen combustion:

$H_{2\,(g)} + \frac{1}{2}O_{2\,(g)} \rightarrow H_2O$ + heat.

The heat or enthalpy of formation associated with liquid water and the overall fuel cell reaction is $\Delta H = -286$ kJ/mol at 25°C and 1 atmospheric pressure. The negative (-) sign of the enthalpy represents an exothermic reaction; the energy is dissipated as heat. Therefore, the net reaction of a hydrogen fuel cell can be written as follows:

$H_{2\,(g)} + \frac{1}{2}O_{2\,(g)} \rightarrow H_2O_{\,(l)}$ + 286 kJ/mol[4].

At 25°C and 1 atmospheric pressure, the reactants (H_2 and O_2) and water are in gaseous state and liquid form, respectively. The enthalpy of the HOR, 286 kJ/mol, is also known as the hydrogen heating value (HHV)[4].

The substantial dissimilarity in the reaction kinetics between the anodic and cathodic catalytic reactions (i.e. between the HOR and ORR), utilizing pure platinum (Pt) as the sole electrocatalyst, has led to several investigations aimed at accelerating the ORR. Efforts are currently directed at the development of highly functional binary and ternary electrocatalysts, containing platinum with cheaper metals, for the problematic multi-electron ORR.

1.3 Design of Pt-based Contact Electrocatalysts for ORR

The fuel cell industry relies entirely on supported metal nanoparticles to catalyze reactions associated with direct fuel cells[12-21]. Carbon supports are the most widely employed materials for carrying nanocatalysts in fuel cell reactions[5, 13-16, 19, 20, 22]. In heterogeneous catalysis, the catalytic reactions occur on the surface of the nanocatalyst and the kinetics of the reactions are thus influenced mainly by the catalyst's surface atoms[23]. The structural parameters and kinetic effects that influence the functionality of metal nanocatalysts are shown in Figure 1.2[23, 24].

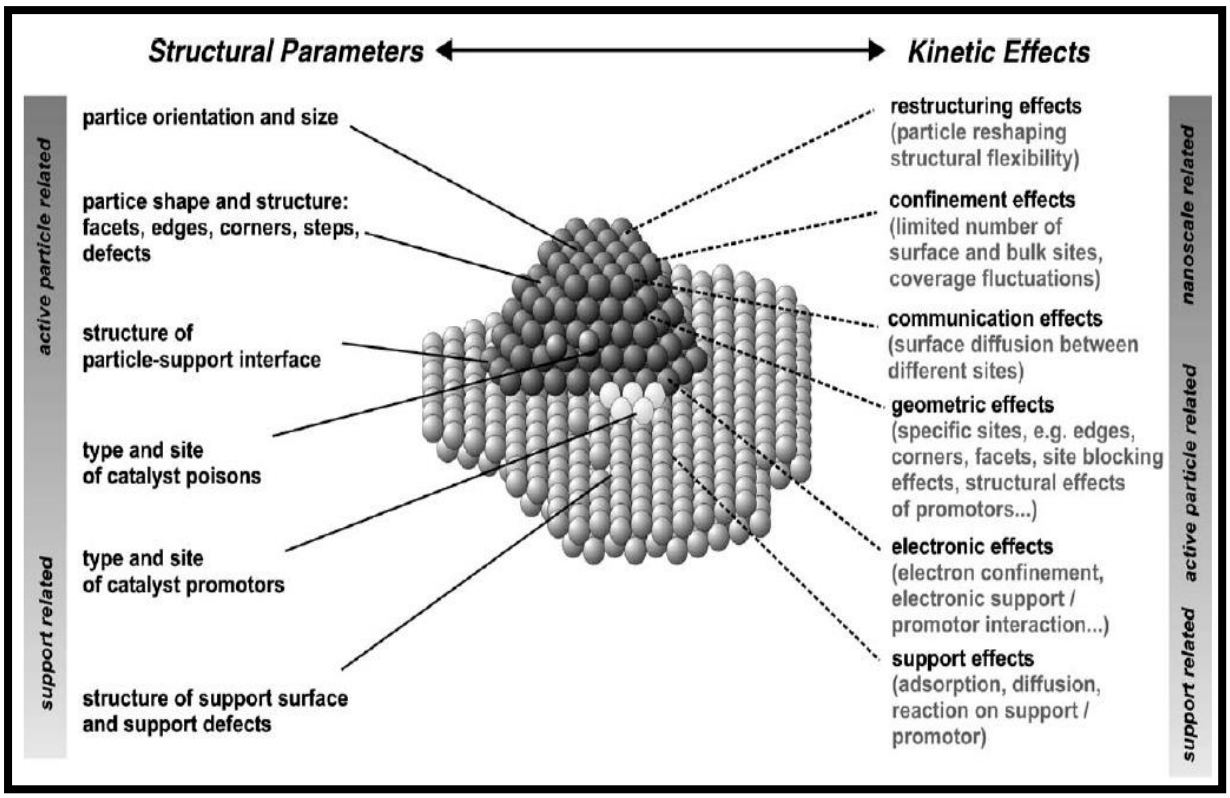

Figure 1.2: Structural parameters and kinetic effects on supported metal catalysts (after Libuda and Freund)[23, 24].

Support-carried multimetallic nanoparticles are more finely tunable than single-metal nanocatalysts and are the key determinants of both activity and selectivity properties[23, 24]. Therefore, contact nanocatalysts of alloyed structures can exhibit enhanced catalytic activity, relative to pure metal nanoparticles. Core-shell nanoparticles, constructed from a cheap metal core and a highly active shell such as Pt, can improve the (expensive but active) shell metal's use-efficiency[25]. Core/shell nanoparticles are also potentially highly stable, and can be recycled and reused several times without exhibiting significant losses in functionality and selectivity[25]. The development of Pt-based bimetallic nanocatalysts, achievable by alloying Pt

(the most efficient single-metal catalyst in PEMFCs) with inexpensive and less catalytically active non-noble metals (such as Co, Ni, Fe, Cd, Cu, Zn, Cr, Mn), is thus the most viable approach in not only reducing the cost of the catalyst, but also improving its catalytic properties and providing high stability[2, 25-31].

Bimetallic nanoparticles are well-known to display superior catalytic properties due to synergistic catalytic effects between the two metals[32-39]. The enhancement in functionality of the major Pt catalyst by the incorporation of a second metal is therefore the focus of investigations to understand and optimize the structure/composition/activity relationships in these nanoparticle catalysts[40-44]. Since the catalytic activity of nanoparticles depends sensitively on their structural characteristics, the key challenge is to maintain good control over the homogeneity, composition, size, morphology and dispersion of nanocatalysts during synthesis[26, 45]. Therefore, by tuning those structural characteristics which are well-known to influence the activity, selectivity and stability of bimetallic nanoparticles, novel catalysts with unusual properties can be created to facilitate specific catalytic reactions[23, 46-48].

Although alloying is a well-studied phenomenon, the regulation of segregated nucleation and growth in bimetallic nanoparticles is complicated by the different thermodynamic and kinetic characteristics of two or more different elements under the same reaction conditions. The controllable synthesis of bimetallic nanoparticles thus remains an area requiring investigation. In particular, the synthesis of binary and ternary nanoparticles by high-temperature reduction, using careful control of the experimental parameters, has not yet been fully investigated.

1.4 Research Hypothesis

The catalytic functionality of multimetallic nanoparticles improves with increasing nanoparticle angularity; and also improves with increasing platinum content. The research presented here, explores the hypothesis that there exists an optimum morphology (faceted surface) and composition (high Pt) which can deliver good catalytic functionality with a reduction in cost, as illustrated in Figure 1.3.

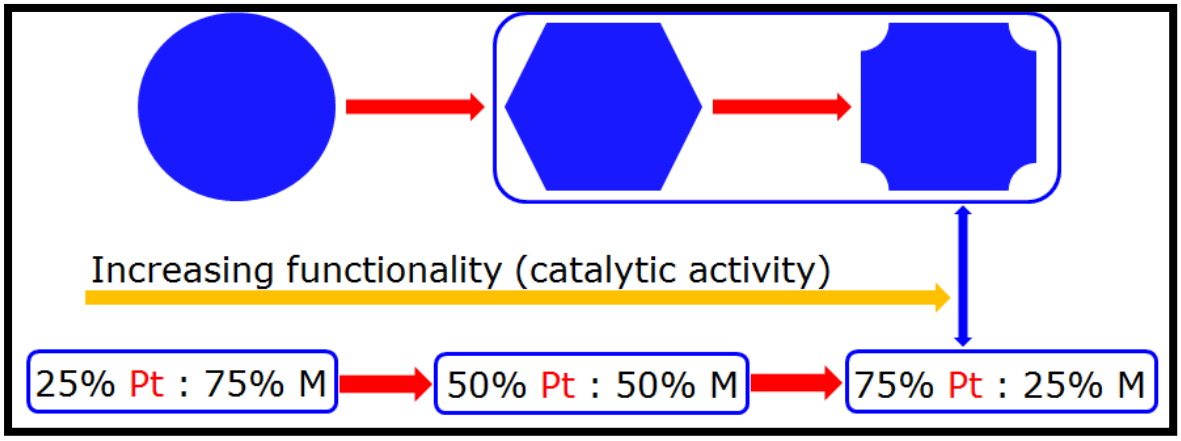

Figure 1.3: Illustration of Research Hypothesis.

1.5 Project Objectives

- Develop high temperature, chemical solution-based synthetic protocols for the fabrication of both mixed and core-shell platinum (Pt)-based nanoparticles containing nickel (Ni), cobalt (Co) and vanadium (V)
  - Select optimum synthesis strategies
  - Synthesize well-defined morphology-directed novel bimetallic (binary) and trimetallic (ternary) nanoparticles for the oxygen reduction reaction (ORR)
- Support the as-synthesized binary and ternary alloy nanoparticles onto carbon carriers (supports)
  - Characterise the effect of carriers on nanoparticles
- Perform electrochemical characterization to evaluate the catalytic functionality of the novel bimetallic and trimetallic nanoparticles
  - Deduce structure-composition-activity relationships of these nanoparticles

CHAPTER 2 LITERATURE REVIEW

2.1 Metal Nanoparticles

Nanoparticles, defined as particles in a size range of 1 – 100 nm, are well-known to possess many unique properties which are necessary for industrial processes[49-52]. In particular the properties of metals at the nanoscale, including catalytic properties, differ significantly from those of the bulk form. These novel properties arise from the nanoparticles' morphology, monodispersity, size and crystal structure[12]. The fabrication of nanoparticles with outstanding structural properties is thus sought after for a multitude of applications. A variety of metallic nanoparticles are currently under investigation for catalytic applications in gas sensors, energy storage, optoelectronics, magnetic resonance imaging and biomedicine[33, 53-66]. In catalysis, a high surface area is necessary to optimise catalysis; there is hence a pressing need for nanoparticles with large area-to-volume ratios, low coordination number, and more edges and corners[67-70]. This need drives the development of chemically reactive, catalytically active, robust and cost-effective nanocatalysts to increase the reaction rate[1].

There are two approaches to prepare nanoparticles: the "top-down approach" and the "bottom-up approach"[43, 44, 53, 71-76], as shown in Figure 2.1[73, 77]. The former approach utilizes physical methods such as ball milling or attrition, whereas the latter employs chemical solution-based synthetic protocols[53, 72, 73, 75, 76]. Deploying the top-down route, large-scale production of nanoparticles can be achieved. However, to obtain uniform-sized nanoparticles and manipulate their size is very difficult. In comparison, the bottom-up approach presents a powerful tool to synthesize well-defined and uniform-sized nanoparticles with controlled size[43, 53, 71, 73, 75, 76].

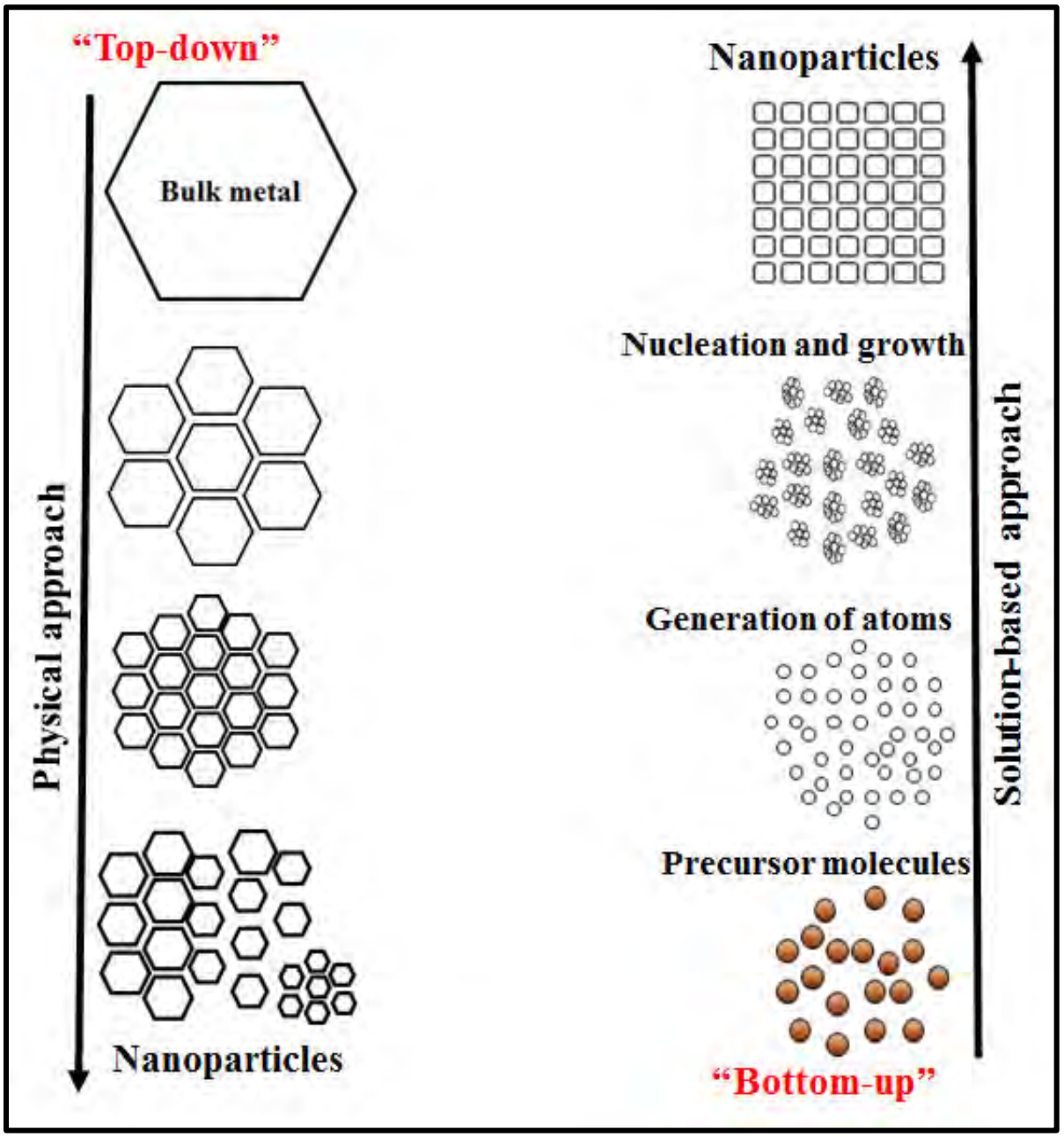

Figure 2.1: Schematic illustration of synthetic approaches of metal nanoparticles (redrawn after Toshima and Yonezawa)[73, 77].

Solution-based synthetic strategies thus offer an approach for synthesizing well-defined crystallographic, facet-directed, multifunctional electrocatalysts exhibiting superior electrocatalytic activity. Consequently, the solution-based "bottom-up" synthesis routes provide accuracy in the design of the preferred structural properties of the catalyst including the size, shape-and composition-controlled growth[78-80]. The adjustment of key reaction parameters, using the solution-based synthetic approaches to prepare nanoparticles, can lead to the formation of high-index facets showing enhanced chemical and thermal stability under both oxidising and reducing conditions, as well as at high temperatures. Thus, high-index Pt-based

nanoparticles are expected to display outstanding catalytic activity and selectivity even in harsh acidic reaction conditions, rendering them good candidates for fuel cell application[81].

2.1.1. Bimetallic Nanoparticles

In bimetallic nanoparticles, a great diversity of structures may exist as a result of unusual distributions of atoms from individual metal elements[73]. These atomic arrangements are distinct from pure elemental nanoparticles, from pure metals in bulk form and from bulk alloys. In nanoparticle-catalysed fuel cells[1] and sensors[82-84], research into bi-(and tri-) metallic catalysts has stemmed from the prohibitively high cost of the standard catalyst, platinum (Pt)[1, 85]. The detailed investigation of microstructural evolutionary characteristics such as size, dispersity, surface structure, composition and morphology, which determine the catalytic performance of binary and ternary nanoalloys, is deemed fundamental for catalytic applications[86]. The design and engineering of bimetallic nanoparticles thus emerges as an active area of research, with the aim of fabricating highly functional, cost-effective catalysts on a large scale.

A further advantage of bimetallic nanoparticles lies in their stability (prolonged lifetime). A core negative aspect of monometallic particles is their instability at extremely small diameters. However, this can be solved by synthesizing bimetallic nanoparticles instead of elementary metal nanoparticles[25-27]. For example, recent studies have shown that single-crystal (bulk) crystallographic-facet-directed Pt_3Ni (111) surfaces exhibit approximately 90 times enhanced functionality relative to the state-of-the-art Pt/C electrocatalysts for ORR, as shown in Figure 2.2[87]. The considerable difference in catalytic performance can be attributed to the changes of the d-band centre (ε_d), evolution of novel surface atomic arrangements (surface configurations) of Pt as a result of alloying effects and decreases in coverage of hydroxyl group species (OH_{ads}) owing to the integration of nickel (Ni) atoms[87]. The challenge that arises from these results, is the development of binary nanoparticles (such as Pt_3Ni) with (111) surface facets exposed, for ORR catalysis.

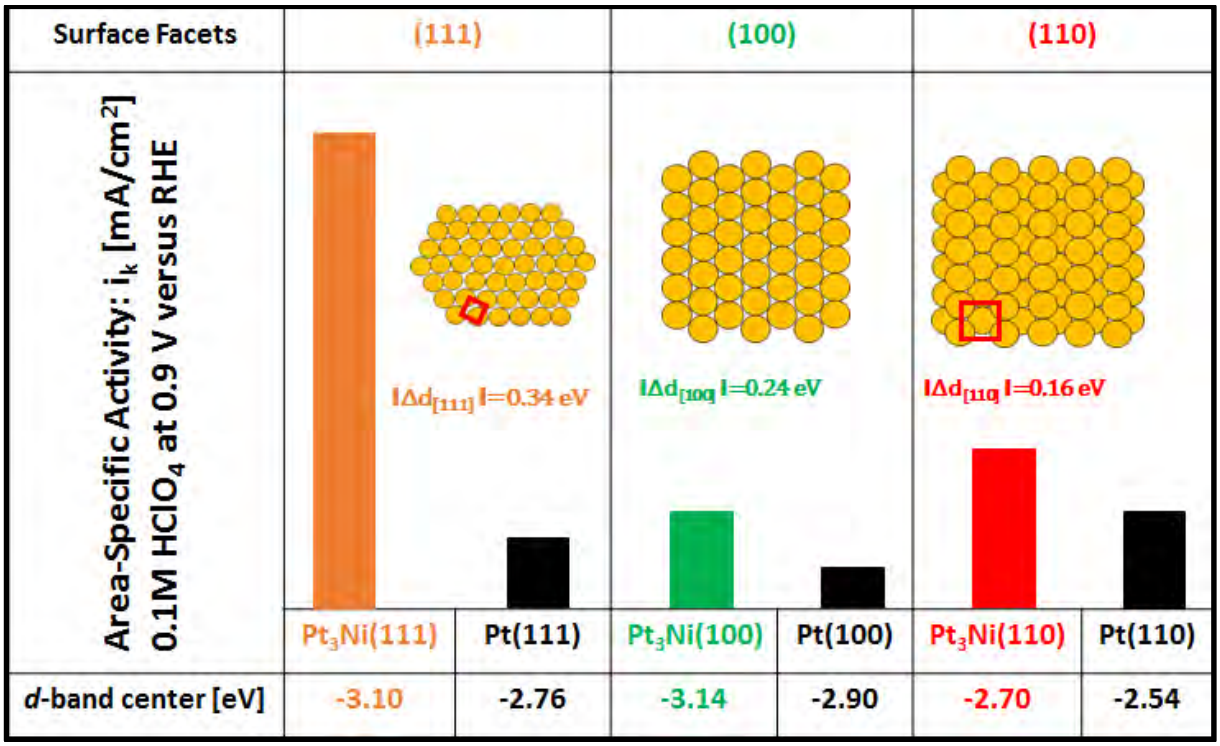

Figure 2.2: Surface structural and compositional influences on specific activity of ORR-catalyzed by Pt_3Ni and Pt electrocatalysts (redrawn after Stamenkovic *et al.*)[87].

The preparation of particles with very small sizes and distinct shapes with more facets, corners, steps and kinks ensures that the larger active sites or surfaces are more exposed, and can thus initiate and facilitate the catalytic processes[23, 24]. The exploration of high performance Pt-based bimetallic and trimetallic electrocatalysts still remains the area of greatest importance since the catalytic activity of catalysts depends entirely on the surface structural properties. The rational design strategies for Pt-based electrocatalysts for the ORR are outlined in Figure 2.3[6]. Recent studies have shown that more open-framework Pt_3Ni nanostructures display enhanced functionality towards ORR[88]. The catalysts are characterized according to their nature and the support utilized, followed by the structural properties and composition.

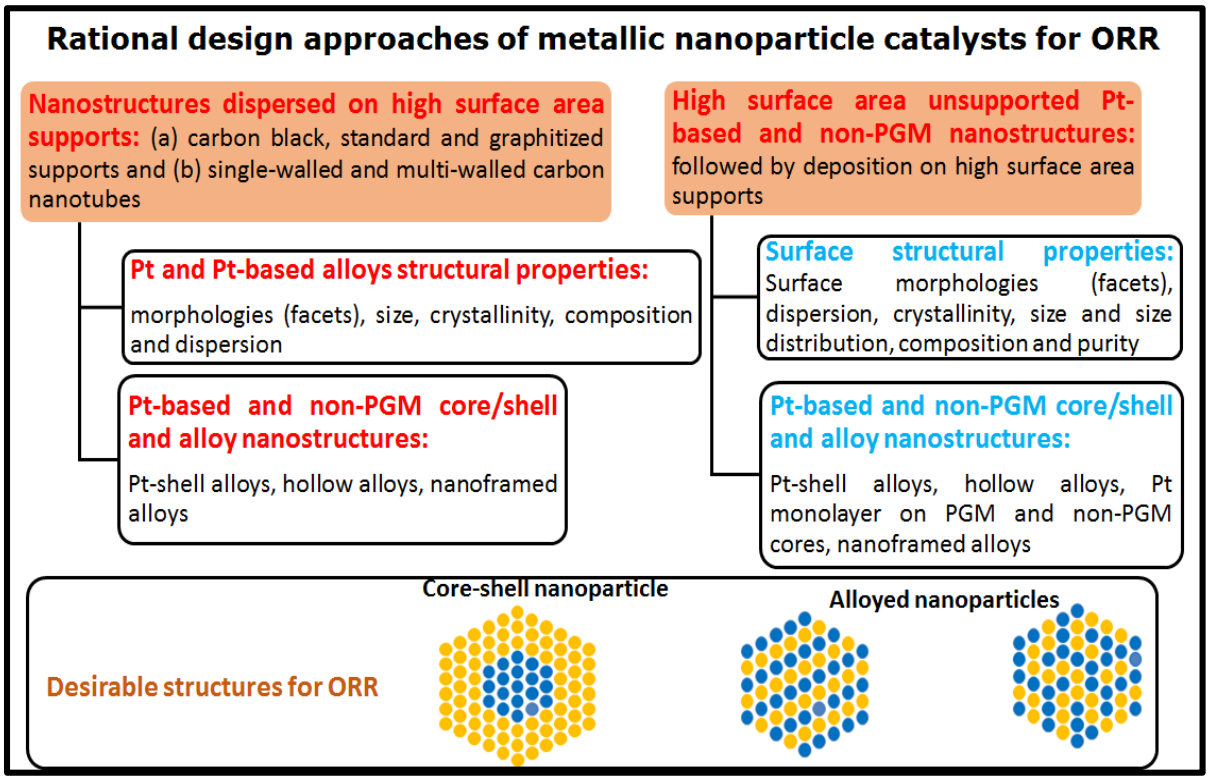

Figure 2.3: The rational design methods of high performance Pt-based contact electrocatalysts for ORR (redrawn after Debe)[6].

Bimetallic nanoparticles are known to display superior catalytic properties that can aid in facilitating reactions due to synergistic catalytic effects between the two metals[32-39]. The enhancement in functionality of the major Pt catalyst by the incorporation of the second metal as the promoter can be induced by: (a) structural (bifunctional) effects – modification of the local bonding geometry, (b) ensemble (morphological) effects – changes in the distribution of the active surface sites, thereby creating different reaction mechanisms and (c) ligand (electronic) effects – the promoter metal modifies the electronic properties of the well-known catalytically active Pt metal to influence the adsorption/desorption of the reactants/intermediates/poisons[89, 90].

Bimetallic nanoparticles exhibit synergistic catalytic effects completely dissimilar to either their monometallic or bulk alloyed counterparts[26, 44, 66, 69, 89-99]. The surface properties of this novel class of mixed-metal nanoparticles are profoundly influenced by the incorporation of a second metal, which can enhance their efficacy, selectivity, stability and resistance to poisoning relative to the monometallic nanoparticle[1, 44, 54, 91, 97, 100-110]. This improvement in catalyst functionality has been attributed to geometrical ensemble and/or ligand effects, detailed

below[45, 89, 90, 94, 111, 112], resulting in the modification of electronic and chemical properties[104, 106, 107, 111-115].

(a) The geometrical ensemble is defined by the number of surface atoms required for the induction of catalytic process[89, 90]. The d-band center of an admetal influences the change in electronic properties on the surface of another metal. The geometry of the structure (the mean metal-metal bond length) is different from the bulk metal, giving rise to strain effects which modify the electronic structure of the metal as a result of changes in orbital overlap. The d-orbital overlap decreases due to a tensile strain subjected to surface atoms, narrowing the d-band and shifting the d-band center closer to the Fermi level. Comparatively, the increase in d-orbital overlap (broadening the d-band and lowering the d-band center) occurs when the surface atoms are subjected to a compressive strain[104, 111].

(b) The ligand effect is associated with the electronic modifications induced by the interaction between two metals[45, 90, 94]. The electronic environment of a metal atom changes in the presence of other metals. This contributes to the change in its electronic structure, hence its chemical properties. The modification in the d-orbitals of transition metal surfaces, which participate largely in bonding interaction with the reactants, arises by alloying with other metals or promoters[104, 112, 115-117]. These novel characteristics comprising the electronic and chemical properties of bimetallic nanoparticles constitute a promising class of catalyst at nanoscale, with improved performance, selectivity and life-span[23].

The functionality of Pt towards the ORR is governed by its adsorption energy, the dissociation energy of the O-O bond and the binding energy on the active Pt surface sites. These Pt energies are strongly influenced by its electronic structure (Pt *d*-band vacancy) and the geometric effect (the Pt-Pt interatomic distance)[118]. However, the incorporation of promoter metals modifies: (a) the Pt electronic structure by increasing the Pt *d*-band vacancy which, in turn, induces strong metal-O_2 interaction and then weakening of the O-O bonds and (b) the geometric effect via lattice contraction, thereby creating favourable Pt-Pt interatomic distances essential for the dissociative adsorption of O_2[4, 118, 119].

High performance electrocatalysts are evaluated in terms of functionality, selectivity, stability and resistance to poisoning of the catalyst surface[1, 39, 54, 91, 92, 120, 121]. The electrocatalysts

employed in PEMFCs, experience poisoning by carbon monoxide (CO) or aldehyde (CHO) species, which bind strongly to a metallic catalyst surface and thereby hinder the functionality of the catalyst. This CO or CHO poisoning eventuality can be overcome by the development of poison-resistant Pt-based alloyed electrocatalysts[25, 122-124]. In this case, highly reactive metals can aid the oxidation of CO- or CHO-containing species by adsorbing the oxygen-rich molecules on poisoned Pt sites[25, 123, 124]. Thus, the ability to design novel anode and cathode CO- or CHO-tolerant electrocatalysts, efficient in splitting hydrogen and oxygen respectively, for PEMFC applications can be realized through the effective colloidal "bottom-up" synthesis of Pt-based bimetallic nanocatalysts[79, 80, 122, 125].

2.2 Chemical Solution-Based Synthesis of Bimetallic Nanoparticles

Synthesis of highly-quality bimetallic nanoparticles with tunable size, morphology, composition and structure requires good control, and manipulation, of the synthesis parameters[52]. This is best offered in synthesis from metal precursor salts, which allows manipulation of a wide variety of experimental parameters. Achieving the correct size- and shape-evolution properties, and compositional regulation, of colloidal bimetallic nanoparticles, demands precise control over the experimental parameters[10]. Intensive research efforts are devoted to the development of viable and precise synthetic routes which can lead to the unique structural properties of monodisperse nanoparticles[10]. The development of reproducible synthetic routes for the preparation of bimetallic nanoparticles is important from both a scientific and a technological point of view[52]: rigorous investigation will contribute to an understanding of how the addition of a second metal influences the catalyst activity, stability and selectivity of metallic nanoparticles.

Depending on the synthetic techniques employed to prepare nanoparticles[69], structures such as particle-in-particle, particle-on-particle (heterostructure), aggregated nanoparticles, core-shell nanoparticles, alloyed particles, separate nanoparticles and super core-shell nanoparticle can be achieved[26, 60], as shown in Figure 2.4[60]. The final structure of bimetallic nanoparticles is determined by the distribution of the two distinct metal atoms[69, 73].

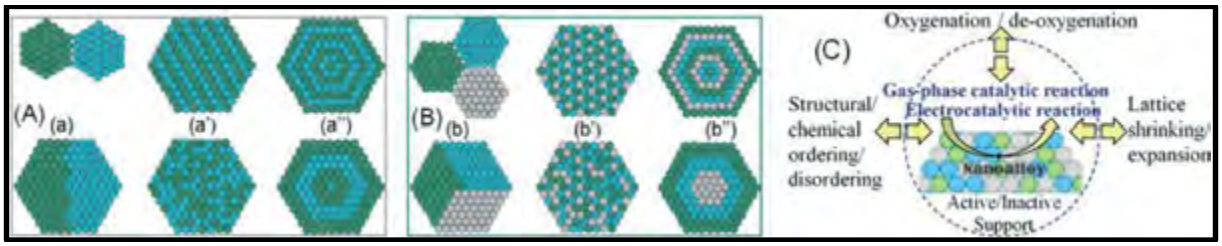

Figure 2.4: Schematic illustration of possible structures of (A) bimetallic and (B) trimetallic nanoalloys. (C) Correlation between functionality and the catalyst structure (after Shan *et al.*)[60].

The design of the chemical solution-based synthetic routes involves selection of appropriate chemical reactions, reactants, solvents, surfactants, temperature of reduction, reducers and reaction time[73, 126]. Solution-based chemical synthetic techniques comprising co-reduction[25, 73, 98], thermal decomposition[25], seeded-growth (sequential reduction)[25, 67, 73, 98] and galvanic replacement reactions[25] have been successfully developed and employed to synthesize bimetallic nanoparticle structures.

2.2.1 Co-Reduction

The reduction of metal precursor salts in a suitable solvent is the most common method for synthesizing monometallic nanoparticles. The same principle applies during the preparation of bimetallic nanoparticles where two metal salts are reduced together[25, 26, 73, 98]. However, it is difficult to simultaneously reduce and control the nucleation process of two metal types because of the differences in the reduction potential and chemical behaviours of two types of metals. In order to avoid separate nucleation of the two metals, appropriate reducing agents (reductants or reducers) and an appropriate reaction system must be selected[39, 127-130]. The use of strong reductants such as hydrazine, sodium borohydride and tetrabutyl ammonium borohydride makes it difficult to control the morphology and size of bimetallic nanoparticles. In addition, the use of inappropriate surfactants poses problems due to the difficulty of manipulating segregated nucleation, particle growth processes and the degree of agglomeration[131]. The reduction of metal salts with strong reductants requires the use of suitable surfactants, precisely designed reaction mixtures and reduction conditions. In contrast, the nucleation and growth process are better controlled when weak reductants are used[39, 127-130, 132]. In the presence of appropriate surfactants, reducers and reaction system to control separate nucleation and growth process, bimetallic nanoparticles with well-defined shape, narrow size distribution, controlled composition and desired structure can be produced.

The structure of bimetallic nanoparticles is controllable by co-reducing two metals with distinct redox reduction potentials[25, 73]. Generally, the metal with high reduction potential is reduced first, followed by the one with low reduction potential. The final structure of bimetallic nanoparticles is determined by the chemical behaviour of a second metal reduced around the surface of the pre-synthesized seeds of the first metal. This method favours the formation of core-shell nanoparticles only when the distribution of the deposited atoms is even and not suppressed on certain facets. However, when the deposition process occurs only on specific facets without any diffusion of atoms into the preformed seeds, heterostructures are formed. When the atoms of second metal diffuse into the crystal lattice of the first metal, alloyed nanoparticles are produced[25, 73].

The chemical behaviour of metals is closely associated with the intrinsic properties, with the thermodynamically stable state favoured[25]. Nevertheless, the favoured thermodynamic stable state of bimetallic nanomaterials can be altered by reaction conditions such as the selection of solvents, ligands and surfactants. For instance: co-reduction of metals A and B, with the reduction potential of A higher than that of B leads to the formation of A_{core}-B_{shell} nanoparticles. The reverse, B_{core}-$A_{shell,}$ occurs when surfactant that binds strongly to A is introduced into the processing system. In most cases the co-reduction route results in the creation of alloyed instead of core-shell nanoparticles[25].

High-quality nanoparticles with tunable size and morphology can be prepared by the co-reduction process; particle growth rate can be manipulated by the addition of appropriate surfactants, foreign ions, ligands and/or adjusting other reaction parameters such as temperature and time[73, 126]. The surfactants and solvents have different adsorption energy to the crystal surface, directing the size- and shape-evolution of bimetallic nanoparticles by inhibiting the incorporation rate of added atoms onto the surfaces. It is therefore the nature and concentration of additives in the reduction reaction mixtures that influence and determine nanoparticle growth. The reductants also play a fundamental role in manipulating the reduction kinetics, thereby controlling the crystallinity of seeds in the nucleation stage and the final morphology of bimetallic nanoparticles. Furthermore, the morphology of nanoparticles can be controlled by tuning the precursor salts, surfactants and reaction conditions. By altering the molar ratio of two metal precursors, the composition of the final product can be controlled. To obtain the composition of bimetallic products consistent with the feed ratio is quite difficult

due to the incomplete diffusion or incorporation of the second metal atoms into the preformed seeds of the first metal[73].

Temperature, time and other reaction parameters greatly influence the degree of diffusion[54]. For example, metals with low reduction potential require a longer time of reduction than those with high reduction potential under the same processing conditions. The synthesis of light transition metals is more complicated and demands good control over experimental parameters as a result of the low reduction potential of their corresponding metal ions compared to those of the noble metal ions. The reduction of light transition metal ions to zero-valent state is very difficult. Besides, these metal nanoparticles have a high instability to oxidation and are easily oxidized. However, these light metals are very important during the formation of bimetallic nanoparticles[73].

2.2.2 Thermal Decomposition (Thermolysis)

Thermal decomposition (thermolysis) is a high-temperature solution-phase synthesis route that involves temperatures of reduction in the range of 150 – 310 °C for the duration of least 30 – 60 minutes, employing both high boiling point surfactants and solvents[25, 26, 30, 52, 54, 98]. The high boiling point solvents commonly employed include benzyl ether (boiling point: 295 – 298°C), octyl ether (boiling point: 286 – 287 °C), 1,2-dichlobenzene (boiling point: 180 °C), 1-octadecene (boiling point: 315 °C) and many more[54, 133], in the presence of inert gases (argon or nitrogen) to exclude oxidation. In some cases, high boiling point surfactants such as oleylamine (boiling point: 348 – 350 °C), tri-n-butylamine (boiling point: 214 – 216 °C), trioctylamine (boiling point: 365 – 367 °C), oleic acid (boiling point: 194 – 195 °C), trioctylphosphine (boiling point: 284 – 291 °C), N-methyldioctylamine (boiling point: 162 – 165 °C), oleyl alcohol (boiling point: 330 – 360 °C) and dioctylamine (281 °C)[54, 133], can also be deployed as both solvents and reducers. Therefore, the reduction of metal ions is greatly influenced by the temperature of reduction and surfactants. The thermolysis route produces highly monodisperse nanoparticles of controlled composition, size, shape and internal structure. The preparation of uniform nanoparticles has been achieved using this method, requiring less or no size-selective process in most cases[54]. The diameter of nanoparticles can be determined by the nucleation rate and termination time. The reaction conditions including

time, temperature, concentration and chemistry of reagents and surfactants can be adjusted to control the size of nanoparticles[54, 133].

Generally, the size of nanoparticles increases with increasing reaction time and with increasing temperature of reduction, due to the rapid addition of material to the preformed nuclei. Bimetallic nanoparticles can be prepared by coupling the reduction and the decomposition process, so that one metal ion is reduced with a reducer and the other is thermally decomposed[25, 54, 134]. By controlling the molar ratio of two different metal precursor salts to that of the surfactants, both nanoparticle size and the composition of the final product can be adjusted.[25] On the other hand, the thermolysis process can be used to thermally decompose two types of organometallic precursors independently to prepare bimetallic nanoparticles[25, 135-139]. The composition of the final product is never consistent with the feed ratio of the two metal precursors due to the differences in the reduction rates under the same reaction conditions[25]. The thermal decomposition of two distinct organometallic compounds occurs at different temperatures: in other words, no matter what reduction route is employed (co-reduction and decomposition or simultaneous thermal reduction of the two organometallic precursors), the composition of the final product is always distinct from that of the feed molar ratio of the precursors[25].

During the synthesis of bimetallic nanoparticles, the inclusion of more than one metal precursor salt does not guarantee equal modes of atomic distribution of two kinds of metals to form metal-metal bonds as a result of different reaction kinetics[25]. The difference in reaction kinetics can also induce the formation of separate monometallic phases of nanoparticles. To overcome these undesirable hallmarks, two kinds of precursor salts adopted as a single-source are employed[137]. For instance, single carbonyl precursor salts such as $Pt_3Fe(CO)_{15}$, $FeNi_5(CO)_{13}$, $FeCo_3(CO)_{12}$ and $Fe_4Pt(CO)_{16}$ have been used to synthesize bimetallic nanoparticles via the thermal decomposition process[54, 137]. This promotes the formation of new metal-metal bonds between two elements, resulting in the synthesis of bimetallic alloys with no phase segregation and controlled composition. In this regard, the composition of the final bimetallic nanoparticles is consistent with the initial feed molar ratio of two metal precursor salts[25].

2.2.3 Seeded-Growth Mechanism

Seeded-growth is a powerful route for preparing bimetallic nanoparticles of core-shell and hererostructures, which are difficult to synthesize employing other preparative strategies[25, 26, 67, 140-145]. Core-shell nanoparticles are obtained when the deposition of the second metal atoms on the surface of the preformed seeds of the first metal is uniform[25, 67, 73]. However, if the deposition occurs only on a specific site of the seed, the formation of heterostructures is favoured. The synthesis of bimetallic nanoparticles using seeded-growth requires both heterogeneous nucleation and simple growth via atomic incorporation[25]. In other words, homogeneous nucleation should be avoided. Using reaction parameters such as high reaction temperature and strong reductants (reducers), to provide enough energy to impede the resulting formation of segregated monometallic nanoparticles, offers thermodynamic requirements for the successful fabrication of bimetallic nanoparticles[25, 146].

The physical parameters that have a great influence on the heterogeneous nucleation and particle growth comprise the lattice mismatch, correlation of surface and interfacial energies as well as the differences electronegativity between two metals[99]. This is due to the interaction between the second metal atoms and the preformed seeds during the seeded-growth mechanism. The initial structure, shape and size of seeding nanoparticles can direct the nucleation and growth mode of the deposition metal. The deposition is usually favoured on the site with the smallest curvature radius on the seed surface. This seed surface is highly active, acting as the nucleation site. Thus, the role played by the seeding nanoparticle shape can be attributed to the dissimilar properties of crystal planes. Additionally, the size of seed nanoparticles can also influence the heterogeneous nucleation and can direct the morphological evolution of the bimetallic nanoparticles. Even though the seeded-growth system presents an effective technique to synthesize core-shell and heterostructure bimetallic nanoparticles, alloyed nanoparticles are still favoured in some cases[25].

The successful preparation of core-shell nanoparticles demands the exclusion of surfactants during the reduction or thermal decomposition of the second metal ions for deposition and incorporation onto the surface of the pre-synthesized seeds. That is, the preformed nanoparticles (seeds) of a different metal to form a core are separated, purified to eliminate any excess surfactants, dried and finally re-suspended in a suitable solvent. The second metal

precursor salt to be reduced and form a shell is selected based on the degree of its solubility to that particular solvent prior to its reduction or thermal decomposition. In this case, slow reducers and low temperatures or the decomposition temperature can be selected to avoid rapid and segregated nucleation and growth, resulting in agglomerated nanoparticles[147].

2.2.4 Galvanic Replacement Reaction

Galvanic replacement reaction (GRR) is the displacement process where noble and active metals displace the highly reactive (less active) metals in solutions. This synthesis approach is similar to the seeded-growth mechanism in the seeded-growth process. However, in the seeded-growth mechanism, the preformed metal nanoparticles are not oxidized and serve as seeds for the second metal overgrowth, whereas in the galvanic replacement reaction the pre-synthesized metal nanoparticles serve as sacrificial templates and get partially consumed[25]. Recent studies have shown that the GRR is the most powerful technique for controlling and dictating surface structural properties such as the size, surface facets, composition and also creating more complex nanostructures[148-151]. Generally, via the galvanic reactions the synthesis of bimetallic nanoparticles can be achieved[152-155]. Recent studies have shown that the GRR is the most powerful technique for controlling and dictating surface structural properties such as the size, surface facets, composition and also creating more complex nanostructures. Generally, via the galvanic reactions the synthesis of bimetallic nanoparticles can be achieved[152-155].

Compositional evolution can be varied and tuned by mixing and partially displacing the templates via the homogeneous mixture or sequential addition of more than one type of metal precursor salts. Since the GRR distorts the initial surface structures of the metallic template, proper adjustment of the reaction kinetics is required. In addition, altering the reaction factors such as the temperature, nature and concentration of the precursor salts, can affect the displacement process[156, 157]. There are two key factors that should be taken into consideration during the preparation of bimetallic nanoparticles using the galvanic replacement route: (a) incomplete consumption of the as-synthesized metal template by ensuring that the amount of secondary metal ions is less than the critical value and (b) retention of the morphology of the metal template, for which good control over the reaction kinetics is of profound importance. Therefore, the reaction kinetics determines the structure of the final product. For example, slow and even galvanic reaction on the surface of a metal template favours the formation of core-

shell bimetallic nanoparticles. When the reaction kinetics induce fast inter-diffusion between the metal template and second metal atoms, alloyed nanoparticles can be synthesized[25]. More complex nanostructures can be achieved through the preferential/selective oxidation and dissolution of the metallic template atoms[151]. A wide range of nanostructures exhibiting more open surface structures characterized by complex porous and hollow interiors with well-controlled compositions have been reported elsewhere[148-150].

2.2.5 Electrochemical Reduction

The preparation of size-controlled metal nanoparticles in colloidal solution has been achieved by the electrochemical reduction method, as presented in Figure 2.5[158]. This reduction route involves the creation of metal atoms from the bulk metal. The anode serves as the metal source and becomes oxidized in the presence of a quaternary ammonium salt, which behaves as both the electrolyte and the stabilizer[159]. At the anode, the precursor metal ions are generated and reduced by electrons produced from the cathode to yield colloidal metal nanoparticles[158].

Bimetallic nanoparticles have also been obtained by deploying this reduction technique[159, 160]. The size of the nanoparticles can be controlled by the current density, with increasing current density resulting in the formation of smaller nanoparticles[158]. The main advantages to this method comprise low cost, high yields, easy particle isolation and good control over the final composition of bimetallic nanoparticles[73, 158].

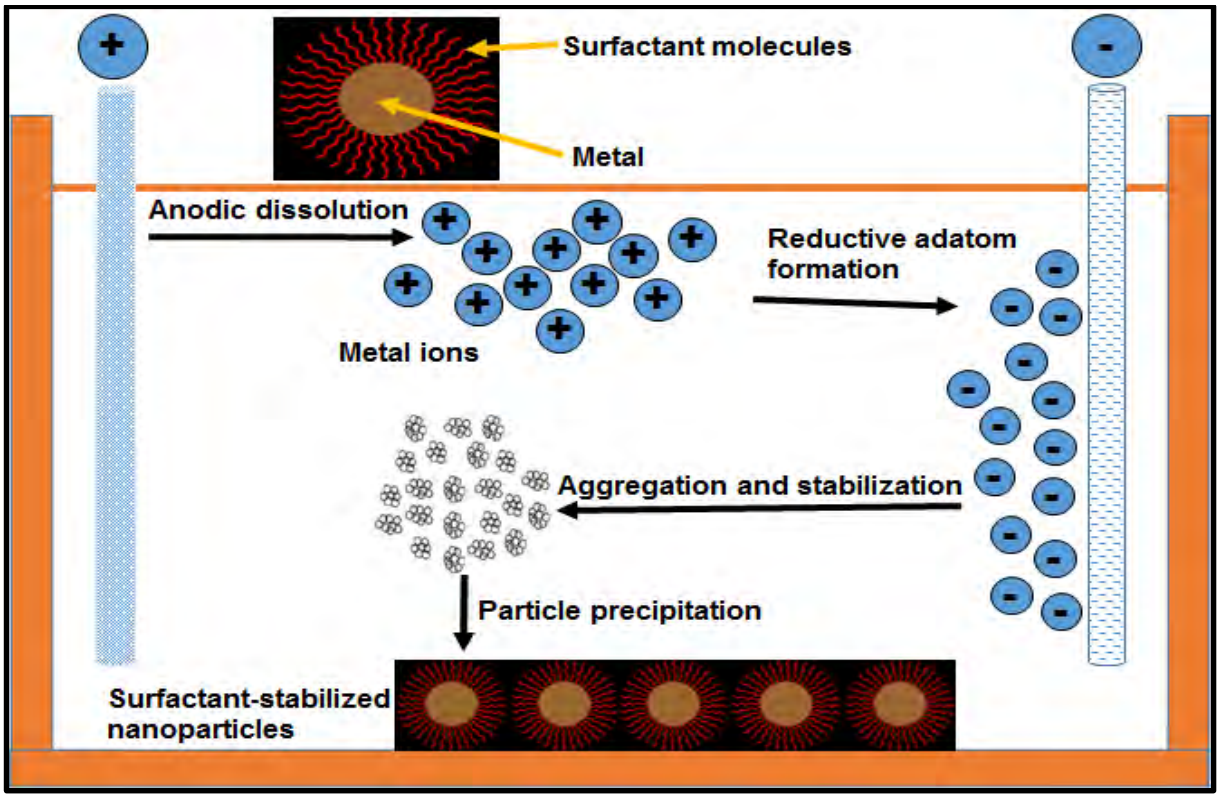

Figure 2.5: Schematic illustration of electrochemically synthesized metal nanoparticles (redrawn after Reetz and Helbig)[158].

2.3 Characterization of Bimetallic Nanoparticles

Detailed characterization of bimetallic nanoparticles to determine their structural aspects comprising size, morphology, composition, dispersity and aggregation state obtained via chemical solution-phase synthetic methods are of vital importance[26]. The structural properties of bimetallic nanoparticles depend entirely on a number of experimental parameters such as the synthesis protocols, heat treatments, variables, promoters, nature of the carrier and composition[44]. The homogeneity of particle size and shape reveals the nature and physical traits of nanosized structures. In order to obtain the information about the characteristic features of nanoparticles, the following characterization techniques have been developed and utilized, as detailed in Table 2.1.

Table 2.1: Characterization methods employed for the structural investigation of nanoparticles.

Characterization Method	Structure Information
Transmission Electron Microscopy (TEM)	Size, morphology, dispersion, crystal structure, presence of agglomerates
Energy Dispersive X-ray (EDX) Spectroscopy	Elemental composition, alloying
Ultraviolet (UV)-Visible Spectroscopy	Plasmon bands, formation of bimetallic nanoparticles, aggregates
Scanning Probe Microscopy (SPM)	Surfaces and structure (including atoms)
X-ray diffraction (XRD)	Elemental composition, alloying extent
X-ray photoelectron Spectroscopy (XPS)	Oxidation states, elemental composition, alloying, existence of impurities
Small angle X-ray Scattering (SAXS)	Size (core + ligand shell)
Extended X-ray Absorption Fine Structure (EXAFS) Spectroscopy	Atomic number, distance, coordination number of atoms surrounding the element
X-ray Absorption Near-Edge Structure (XANES) Spectroscopy	Oxidation state, orbital occupancy
Nuclear Magnetic Resonance (NMR) Spectroscopy	Electronic environment of metal atoms, adsorbed organic molecules on nanoparticle surface

2.3.1 Transmission Electron Microscopy (TEM)

TEM, which involves passing of electrons through the sample, provides visual information on the degree of aggregation, size, size distribution and shape[73, 122, 161]. Samples for TEM characterization are prepared by placing a drop of colloidal nanoparticulate solution onto a carbon film supported by a copper grid and allowing the suitable solvent to evaporate either at ambient conditions or by using a drying lamp. Nanoparticles of heavy metal elements compared to those of light metals give high contrast in the presence of any passivating surface active agents (surfactants)[26, 73]. To obtain better contrast in the case of light metal nanoparticles, very thin carbon support films are required[73].

(a) High resolution TEM (HRTEM) offers resolution at the sub-nm level and provides information not only on the size and morphology, but also on the crystallinity of nanoparticles via atomic spacing measurements, coupled with the electron diffraction pattern. Furthermore, particle growth can be directly observed by in-situ TEM for supported metal nanoparticles[26, 161].

(b) The energy-dispersive X-ray spectroscopy (EDX, EDS) is employed in conjunction with HRTEM to determine the elemental or chemical composition of individual bimetallic nanoparticles[161-163]. The electron beam is focused either on a single particle or over a wide area chosen within the sample by TEM to acquire information from individual or many particles. X-rays are emitted due to excitation by electron beam irradiation. The characteristic energy of the emission allows the elements present to be identified. This technique provides analytical data at a scale which is impossible to obtain with other x-ray characterization methods. In the case where there is no visual information to differentiate between alloyed and core-shell nanoparticles, EDS mapping in STEM mode can identify the composition and distribution of elements within a single particle can aid distinguish between alloyed and core-shell structures[161-163].

(c) Scanning transmission electron microscopy (STEM) involves forming a highly focused convergent beam of electrons and scanning this across the specimen, in a manner analogous to that used in scanning electron microscopy (SEM). A range of signals can be used including those electrons which pass through the specimen undeviated. These produce a bright field (BF) image, which is analogous that formed in TEM mode. Of greater use is to form images with electrons which have been incoherently scattered through high angles. This signal has a strong dependence on atomic number and the image intensity varies approximately with the square of the atomic number of the scattering atoms. The detector for this signal is annular to allow the undeviated bright field signal to pass through to the bright field detector below. Images formed with this high angle annular dark field (HAADF) detector are therefore very sensitive to composition. Since the signal is the result of incoherent scattering, atomic resolution images in this mode are directly interpretable – bright regions represent atomic columns. This is often not the case in HRTEM images, which are formed with coherently scattered electrons and suffer from the phase problem. STEM scanning can be integrated with the EDS system to produce chemical x-ray maps to quantify the elemental distributions. STEM was used extensively in

this work to elucidate the internal structure of bimetallic nanoparticles. Materials with similar lattice spacings but distinct atomic numbers can be readily differentiated using STEM-based techniques[161, 164, 165].

2.3.2 Scanning Probe Microscopy

Scanning probe microscopy (SPM) is an effective technique for investigating the surface of nanoparticles and includes atomic force microscopy (AFM) and scanning tunneling microscopy (STM). The surface of the nanoparticle is imaged at high resolution and this is attained by rastering an atomically sharp tip across the surface. The measured strength of interaction is deployed to map out the topography, electronic/magnetic structure or chemistry of the surface[166].

(a) In AFM, a fine tip is brought near the sample and serves to sense the small repulsive force between the probe tip and the surface. The tip is then rastered over the sample to measure the surface topography[26].

(b) STM uses the same principle that applies in AFM. STM involves the application of voltage between the tip and the sample until a tunneling current flows. This tunneling current depends sensitively on the distance between the tip and surface. The tip is rastered across the surface and moved up or down to ensure that the current flow is constant, in the constant current mode. This generates real-space, atomic resolution topographic images of the sample. However, in constant height mode the tunneling current is measured with the tip maintained at a constant height. This provides informative about the electronic structure and topography. Thus, the electronic structure of a surface atom can be measured using STM[26].

2.3.3 Ultraviolet (UV)-visible Spectroscopy (UV-vis)

During the synthesis of nanoparticles, the notable visual colour changes which occur are indicative of the decomposition of precursor salts, hence the reduction of metal ions and the formation of colloidal zero-valent particles in the presence of stabilizers. The disappearance of the metal precursor absorbance (versus wavelength) peak/shoulder is indicative of the formation of nanoparticles. UV-vis spectral changes during the reduction of different metal

ions provide critical information about the formation of bimetallic nanoparticles[73, 167]. To quantitatively differentiate between monometallic and bimetallic nanoparticles, the spectral changes can be used. Furthermore, comparisons of UV-vis spectra of bimetallic nanoparticles with those of physical mixtures of the respective particle dispersions provides information about the bimetallic structure of nanoparticles[168]. Metal nanoparticles of Au, Ag and Cu have distinct colours related specifically to their particle size and exhibit strong absorption bands in the visible light regime. The UV-vis spectra can thus be an important indication and complementary method for the characterization of metal nanoparticles. Although UV-vis is a critical technique to investigate the formation of both monometallic and bimetallic nanoparticles, it cannot be deployed to determine the structural properties of nanoparticles such as size and morphology[73].

2.3.4 X-ray Methods

These are non-destructive analysis methods used in the determination of the solid structure of metal nanoparticles[73, 169].

(a) Powder X-ray diffraction (XRD) can be used to investigate the phase and particle size increase in the case of monometallic nanoparticles[122]. Comparisons can be made between monometallic and bimetallic nanoparticles because the diffraction pattern of the physical mixtures consists of overlapping lines of the two individual monometallic nanoparticles in contrast to the single phase pattern arising from bimetallic nanoparticles. For particles < 1 nm, it is quite difficult to acquire the structural information as XRD peak widths become broader with decreasing particle size. The study of surface-supported nanoparticles is achieved by XRD, to amass information on the structure, crystallinity, lattice spacing, particle size and qualitative elemental or chemical compositions (inferred from lattice parameter relationships) [170].

(b) X-ray absorption spectroscopy (XAS) is a useful technique for probing the internal structures of metal nanoparticles as well as the species adsorbed on their surfaces. The information acquired using this method include the elements present in the nanoparticle and the local atomic environment and geometry, electron density, coordination number, and interatomic distances[171].

(c) Extended X-ray absorption fine structure (EXAFS) is a powerful technique that involves the transmission of an x-ray beam through the sample to determine the x-ray absorption spectrum, from which the metal nanoparticle structure can be obtained[73]. The specific x-ray absorption spectra of individual metal elements provides information on the atomic number, interatomic distance, coordination number of atoms surrounding the element whose absorption edge is investigated and the electron density[26]. For alloyed or core-shell nanoparticles, the number of surrounding atoms of individual adsorbing metal element can be computed, hence an estimation of a possible structure of nanoparticles[122]. In the case where colloidal particle size and dispersions are small, samples for EXAFS investigation require concentrated dispersions whilst still avoiding agglomeration to acquire precise and high quality information[73].

(d) In X-ray absorption near-edge structure (XANES), spectra from the x-ray absorption edge are used. The spectral fine structure and edge position is sensitive to the local bonding environment. This technique can be informative of the vacant orbitals, electronic configuration oxidation state of metals as well as the site symmetry of the absorbing atom. These multiple scattering computations can be compared with experimental XANES spectra to investigate the geometrical arrangements of atoms surrounding the absorbing atom[122].

2.3.5 Metal NMR Spectroscopy

NMR spectroscopy of metal isotopes provides information about the electronic environment of metal atoms in both monometallic and bimetallic nanoparticles by virtue of the NMR shifts induced by free or conduction electrons (known as Knight shifts)[73]. Paramagnetic and ferromagnetic metal nanoparticles may be probed by metal NMR. The coordination of metal atoms can be indicative of bimetallic nanoparticle formation and the electronic properties may provide information on the study of catalytic properties of nanoparticles. The structures of adsorbed organic molecules on the crystal surface of nanoparticles such as the passivating molecules and polymers, can be determined by ^{1}H, ^{13}C and ^{31}P NMR[26, 100, 110, 172, 173].

2.4 The Stabilization of Metal Colloids

Colloidal metal nanoparticles are often directly synthesized in the presence of stabilizers (surfactants) in order to suppress agglomeration and aggregation during synthesis[27, 71, 73, 98, 174-181]. As a result of the high surface area-to-mass ratio of nanoparticles, the excess surface free energy results in formation of unstable colloids[71]. Agglomeration, which reduces the surface energy, leads to a decrease in catalyst functionality during industrial chemical processing (catalysis)[71, 98]. It is therefore of primary interest to harvest metallic nanoparticles in finely dispersed state or as stable colloids[98].

The stabilization of metallic colloids during synthesis is therefore important. Stabilizers serve to arrest nucleation and growth by coating, stabilizing, modifying surface reactivities and inhibiting oxidation of nanoparticles[182]. In addition, stabilizers also mediate size and shape evolution of nanoparticles[12, 27, 71, 73, 98, 177-181]. Surfactants that bind strongly to nanoparticle surfaces or bulky organic molecules slow the rate of growth, forming particles with smaller mean size and also hinder growth on specific facets, resulting in a variety of nanoparticle morphologies[12, 177, 179, 183, 184]. The employment of two or more surfactants also directs the growth rate in distinct crystallographic orientations, hence the evolution of different sizes and shapes of particles[27, 175-177, 179, 180, 184].

Good selection of stabilizers for metallic nanoparticles is another critical parameter for the deployment of particles in catalytic applications. Good stabilizers shield nanoparticles during catalysis but do not passivate the nanoparticle fully to induce drastic loss of catalytic efficacy, as a result of fewer active sites available for catalytic reactions[71]. However, stabilizers that bind weakly to nanoparticle surface and thereby creating more free active sites to induce catalysis may result in the rapid deformation of nanoparticles during the catalytic process. Thus, there must be a good balance between the coating of particle surface and the fraction of active sites available to induce catalysis. Separation and purification of nanoparticles synthesized in wet chemical solutions is of paramount importance in order to harvest the required nanoparticles with clean surfaces. These procedures exclude the impurities and excess surfactants, leaving unwanted preparative by-products or wastes in the solution while allowing the collection of the desirable and impurity-free nanocrystals.

There are two distinct classes to nanoparticle stabilization: electrostatic stabilization and steric stabilization[71, 98, 174, 185].

(a) Electrostatic (van der Waals) stabilization arises due to the Coulombic repulsion between nanoparticles, induced by the electrical double-layer of ions adsorbed at the surface of the particle[71, 98, 174, 185]. The repulsion forces result from the chemisorption of charged species at the particle surface, as shown in Figure 2.6[98, 174]. The ionic compounds that can generate electrostatic hindrance comprise halides, carboxylates or polyoxoanions, in aqueous solutions[98].

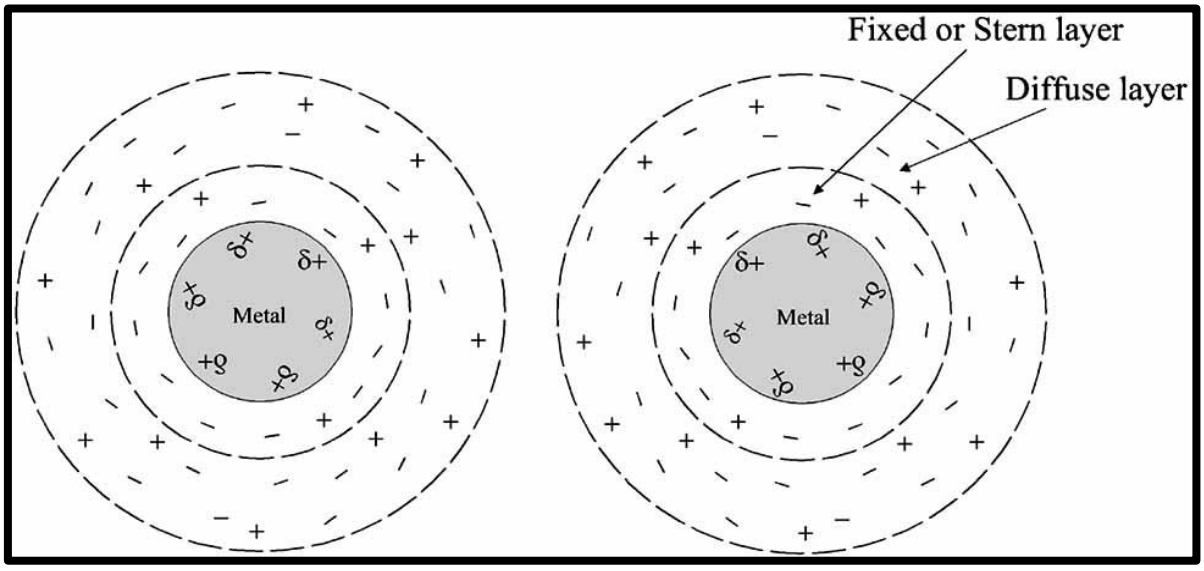

Figure 2.6: Schematic illustration of electrostatic stabilization of metal nanoparticles (after Husein and Nassar)[98, 174].

(b) Steric stabilization (capping ligand) is stimulated by the coordination of bulkier organic molecules such as surfactants, polymers, block copolymers, bulky S and P, long chain alcohols or fatty acids bound to the nanoparticle surface[71, 98, 185], as shown in Figure 2.7. This mode of stabilization can either be employed in organic or in aqueous media, depending on the degree of solubility of the stabilizers[71].

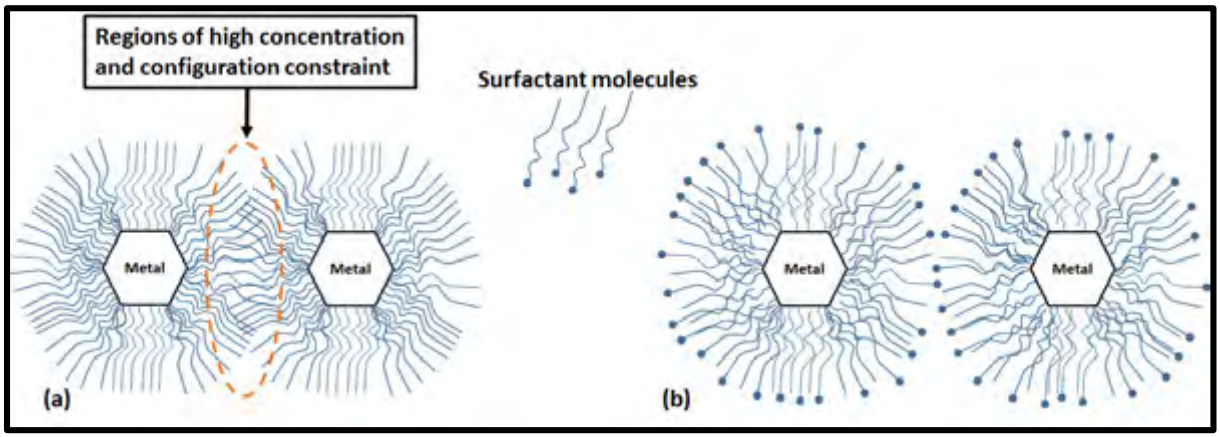

Figure 2.7: Schematic illustration of electrostatic stabilization of metal nanoparticles: (**a**) in organic dispersion medium and (**b**) aqueous dispersion medium (redrawn after Husein and Nassar)[174].

2.4.1 Colloidal Nanoparticle Stabilizers

The stabilization of colloidal metal nanoparticles has been a widely studied field and is achieved by deploying passivating solvent-soluble polymers[70, 186-193], block copolymers[186, 194-197], surfactants[198-202], dendrimers[186, 187, 203-208] and other ligands[1, 181, 209-218].

2.4.1.1 Polymers as Nanoparticle Stabilizers

Polymers are bulky molecules that serve to passivate metal nanoparticles by steric stabilization[70, 186-192]. Polymeric ligands including polyvinylpyrrolidone (PVP)[70, 188-190, 193, 209], polyacrylate[187, 191, 192], polystryrene[219], polyvinylic alcohol (PVA)[193], etc., have been employed to coat metal nanoparticles. PVP and poly(2,5-dimethylphenylene oxide) (PPO) are the commonly used polymeric ligands for nanoparticle passivation and catalysis, as shown in Figure 2.8[220]. This is because they meet both steric and ligand requirements[221]. The selection and variation of these stabilizers can be used to manipulate the size, morphology and quality of the metal nanoparticles in organic (organosols) or aqueous (hydrosols) medium[71].

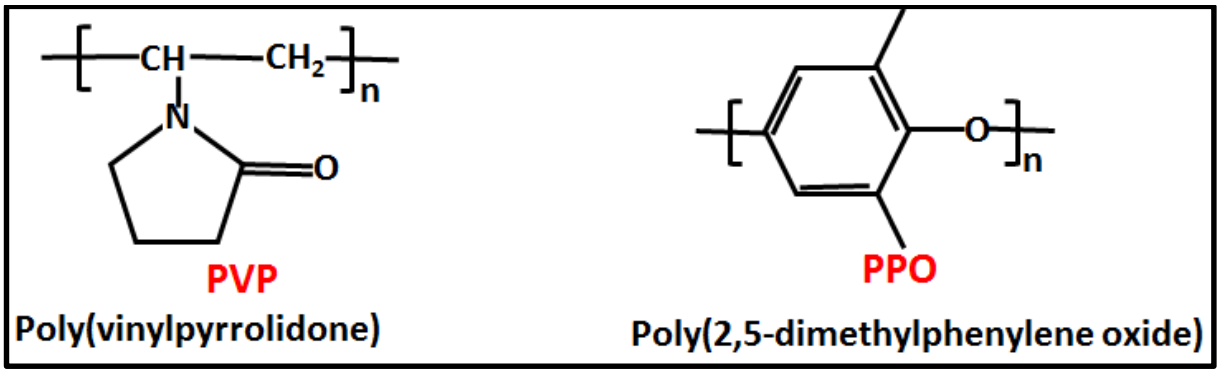

Figure 2.8: Two main polymers used as metal stabilizers for catalysis (redrawn after Andres *et al.*)[220].

2.4.1.2 Block Copolymers as Nanoparticle Stabilizers

Another common method for stabilizing metal nanoparticles involves the use of block copolymers[186, 194, 195]. These block copolymers as stabilizers provide better steric hindrance compared to polymers by themselves. A wide variety of such block copolymer combinations that have been used to stabilize metal nanoparticles include poly(ethene oxide)-block-poly-2-vinylpyridine[194], polystryrene-b-poly-(sodium acrylate)[186], tert-Bu acrylate-2-cinnamoyloxethyl methacrylate[195], polystyrene-b-poly-m-vinyl triphenylphosphine[196, 197], etc.

2.4.1.3 Surfactants as Nanoparticle Stabilizers

Surfactants (surface active agents) also play a critical role in the stabilization of metal nanoparticles and are generally employed to serve as stabilizers of metal nanoparticles synthesized by reducing the precursor metal salts with strong reductants such sodium borohydride ($NaBH_4$). The surfactants provide a combination of both electrostatic and steric stabilization functions. Metal nanoparticles have been stabilized utilizing surfactants such as ($Bu4N^+$)/polyoxoanion[200], tetraoctylammonium bromide (TOABr)[222-226], cetyltrimethylammonium bromide (CTAB)[202, 227-229], sodium bis(2-ethylhexyl) sulfosuccinate (AOT)[230-236], etc. These surfactants possess a polar head group that can generate an electric double layer and a lypophilic side chain that is capable of providing steric repulsion[202].

2.4.1.4 Dendrimers as Nanoparticle Stabilizers

Nearly monodisperse metal nanoparticles have been obtained using dendrimers as stabilizers, with the particles entrapped between the branches[237]. The terminal groups in dendrimers allow for their solubility in only a few organic or aqueous solvents. There are two main families of commercially used dendrimers to prepare stabilized metal nanoparticles: polyamidoamine (PAMAM)-based dendrimers[186, 187, 203-206, 208, 209] and poly(propylene imine) (PPI)-based dendrimers[203, 205-207, 209], as shown in Figure 2.9[206].

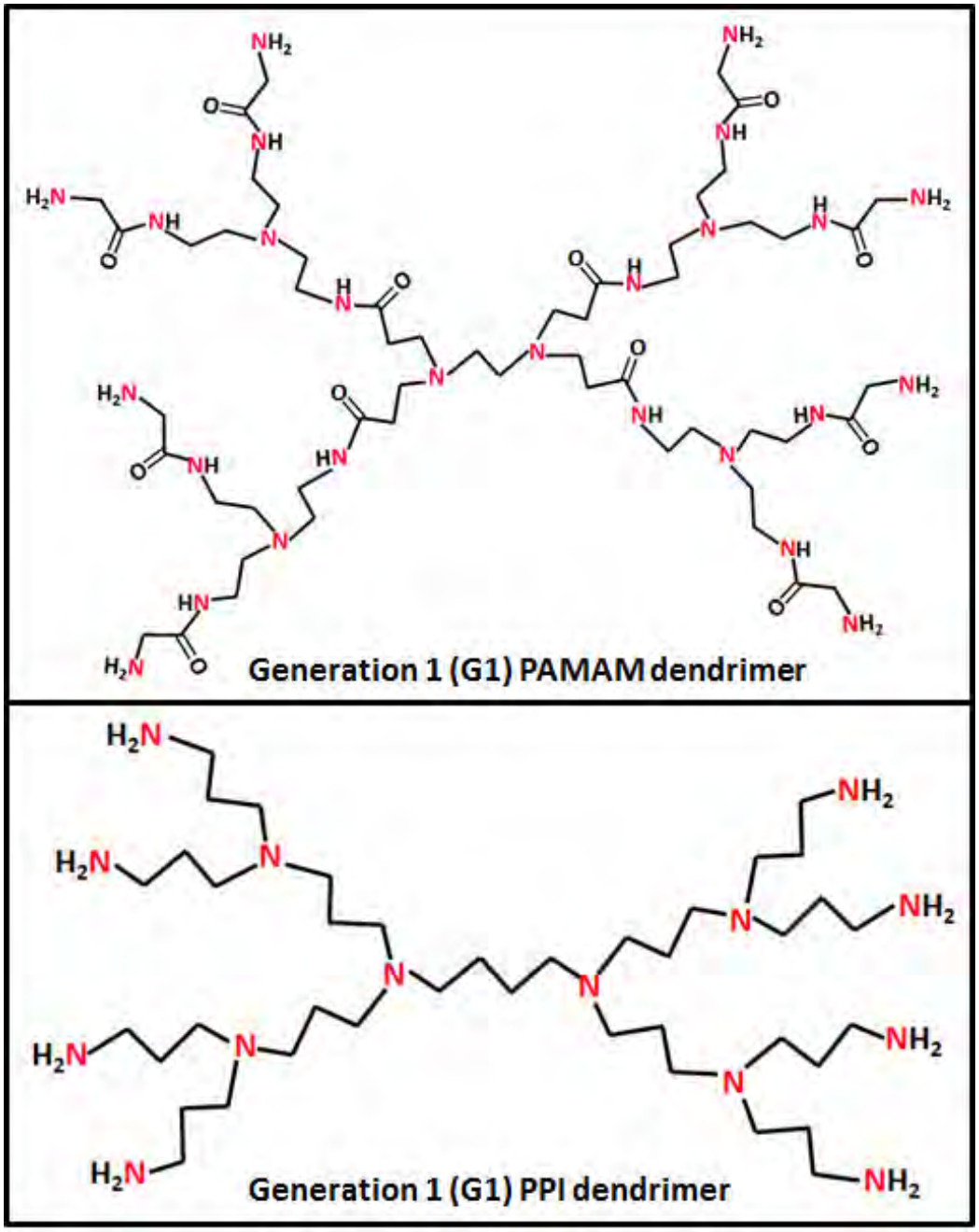

Figure 2.9: Two main dendrimers used as metal stabilizers (redrawn after Crooks *et al.*) [206].

Higher generation dendrimers provide a strong encapsulating function for the passivation of metal nanoparticles[206]. However, too high dendrimer generation can lead to diminished catalytic functionality during catalysis[238]. A good selection of dendrimer generation is therefore an important parameter to be taken into account during synthesis of metal nanoparticle catalysts using dendrimers as protective stabilizing agents[238].

2.4.1.5 Other Ligands as Nanoparticle Stabilizers

Ligands as stabilizers have been utilized to passivate colloidal metal nanoparticles[1, 139, 181, 209-218, 239, 240]. Most commonly, the employment of such stabilizing ligands focuses mainly on the precise molecular development of catalytic nanoparticles, to optimize the parameters that govern the effectiveness of metal catalysts in a wide range of catalytic reactions. Various ligand molecules such phosphines[210-212], thiols[213, 214] and amines[181, 215-218, 239, 240] are the most commonly used stabilizers to passivate metal nanoparticles[1, 209]. Furthermore, high-quality monodisperse nanoparticles comprising metals, metal oxide, alloys and metal-metal oxide heterostructured nanoparticles have been prepared using stabilizing ligands either in single, two or more combinations[54, 241]. In some cases, these stabilizing ligands have been used as mixed organic solvents, stabilizers and reducing agents in an inert atmosphere, for various organometallic precursors to manipulate the size and shape of nanoparticles[139, 180, 183, 184, 218, 240, 242].

2.5 Contact Nanoparticle Catalysts

The field of nanoparticle catalysis is viewed in two key branches: (a) homogeneous catalysis (the catalysts and the reactants are dispersed in a single phase such as a gas or a liquid) and (b) heterogeneous catalysis (the catalysts and the reactants are in different phases with the nanomaterials immobilized on high surface area support materials)[12, 243-246]. In homogeneous catalysis, the catalyst is highly efficient and selective, but the catalyst removal from the reaction media is difficult and it suffers from limited thermal stability[243, 245]. In comparison, heterogeneous catalysis benefits from simple separation and re-usability of catalyst while retaining its high performance in catalytic reactions[243, 245]. The considerable economic significance of contact (supported) nanoparticle catalysts in heterogeneous catalysis is reflected by the degree of their re-usage (recyclability)[25].

Contact monodisperse metal nanoparticles of bimetallic (and trimetallic) in the size range of 1 – 10 nm exhibit more enhanced catalytic functionality than monometallic nanocatalysts[78, 98, 247, 248]. These kinds of catalysts are therefore available to facilitate a variety of current catalytic reactions due to their improved selectivity, efficiency, resistance to poisoning and recyclability[23, 46, 48, 89, 249]. The size, shape, composition and dispersion of such catalysts[12, 23, 25, 44, 67, 238, 249] the basic aspects of the catalytic steps to lower the activation energy towards the desired products[250]. Although contact bimetallic nanoparticles are anticipated to display improved catalytic efficacy in a number of industrial chemical processing reactions due to their tuned surface structure and atomic arrangement of catalysts, their functionality is greatly affected/hampered by the size and shape of nanoparticles, the nature of the carriers, promoters and the methods of preparation[23, 25, 44, 244].

2.5.1 Nature of Supports (carriers)

In heterogeneous catalysis, metal nanoparticles are impregnated (immobilized) onto various solid substrates ranging from metal oxide to carbon supports[13-16, 19-21, 251-267]. The most commonly deployed supports to prepare contact metal nanoparticle catalysts are carbon supports. Depending on the nature of the supports employed, a number of various reactions have been facilitated using nanoparticles impregnated onto different supports as catalysts[14-16, 19, 263, 265]. There are numerous benefits of supported electrocatalysts over bare catalysts: (a) during fuel cell operating conditions, the degree of agglomeration of supported catalysts is minimal, (b) the permeability of the carbon black facilitates gas diffusion to the catalyst's active surface sites, (c) carbon supports are good conductors of electricity; they therefore permit the transfer of electrons from the catalyst sites to the conductive carbon electrodes and then to the external circuit; and (d) finely distributed nanocatalyst particles on carbon supports have optimal contact with the reagents[4, 22]. The functionality of these contact nanocatalysts is, however, greatly influenced by the size, shape and dispersity of metal nanoparticles, the nature of the support, promoters and the preparation route[24, 25].

2.5.1.1 Oxide Supports

Heterogeneous metal nanoparticle catalysts have been prepared by adsorbing metal nanoparticles onto a wide range of oxide carriers[251-263]. These oxides include low surface and

high surface area silica[252], silica monolith[253], MCM-41[256], SBA-15[254, 255], silica gel[251], alumina (Al_2O_3)[257-263], titania[268-270], etc. These oxides are found in different forms, and they have been impregnated with metal nanoparticles for the preparation of oxide-supported metal nanocatalysts for a wide variety of industrial reactions [251-263, 271]. Most of the commercial oxide supports are thermally stable silica-based supports, which makes them suitable for high temperature applications, and suitable for recycling[271].

2.5.1.2 Carbon Supports

Carbon is the most widely employed support for metal nanoparticle catalysts by the adsorption process[13-16, 19-21, 264-267]. Carbon-supported metal nanoparticles have been commonly applied in various important heterogeneous catalysis processes. A wide range of carbon supports for the adsorption of metal nanoparticles have been reported, comprising activated carbon[21], diamond[265], carbon black[264], nanoporous carbon[20], graphite[21], carbon fibers[19], Vulcan XC-72[13-15], carbon nanotubes[15], etc. Of these, carbon nanotubes have been widely utilized as supports for metal nanoparticles. Multi-wall carbon nanotubes have also been used as heterogeneous nanoparticle support due to their high surface area, porosity and pore size distribution[266, 267]. These supported nanocatalysts are applied to facilitate fuel cell reactions, hydrogen sensing and energy storage. However, for fuel cell reactions, the basic surface structural properties of the catalyst support required for optimal electrocatalyst's performance include the following: (a) high surface area, (b) high electrical conductivity, (c) high thermal stability, (d) high chemical stability and (e) high electrochemical stability under fuel cell operating conditions[4, 11, 22].

2.6 Preparation of Contact (Supported) Nanoparticle Catalysts

The preparation of supported metal nanoparticle catalysts for application in heterogeneous catalysis has been achieved by three main routes: (1) synthesis of nanoparticles onto supports by lithographic techniques[47, 166, 272-274], (2) grafting of the nanoparticles onto supports[275-282] and (3) adsorption of the nanoparticles onto supports[13-16, 19-22, 251-271].

2.6.1 Lithographically Synthesized Supported Metal Nanoparticles

Metal nanoparticles supported onto different supports such zeolites (silica and alumina) have been synthesized using electron beam lithography[47, 166, 272-274]. Metal nanocatalysts supported onto silicon wafers[166, 272, 273], silica[47, 272], alumina[47, 274] and titania[47] have also been reported and employed to speed up different industrial chemical reactions.

2.6.2 Grafting of Nanoparticles onto Supports

Supported metal nanocatalysts have also been generated by grafting metal nanoparticles onto solid supports[275-282]. This method benefits from the many chemical bonds available to immobilize metal nanoparticles onto the support. The most commonly used supports with many available chemical bonds to prepare contact metal nanoparticle catalysts include polyacrylamide gels[275-278], polystyrene microspheres[279, 280, 282, 283], etc.

2.6.2.1 Grafting onto Polyacrylamide Gels

Metal nanoparticles have been grafted onto polyacrylamide gels to prepare supported metal nanocatalysts[275-278]. These metal nanoparticle catalysts are immobilized onto polyacrylamide gels with aminoethyl groups[275-278]. The ester functional groups of the stabilizing polymer copolymer polyvinylpyrrolidone (PVP)/methyl polyacrylate copolymer react with the amine functions of the gel to form amide bonds, resulting in the immobilization of the metal nanoparticles. During the immobilization process, the morphology of the particles is retained and there is no metal leaching[275-278].

2.6.2.2 Grafting onto Polystyrene Microspheres

Supported metal nanocatalysts have also been prepared by grafting metal nanoparticles onto polystyrene microspheres[279, 280, 282, 283]. The polystyrene microspheres with surface-grafted poly(N-iso-propylacrylamide) (PNIPAAm) have been deployed as the support for metal nanoparticles, as displayed in Figure 2.10[280, 283]. This grafting process involves the reduction of precursor metal salts in the presence of PNIPAAm as the stabilizing agent and polystyrene nanospheres serving as the support material[280, 283]. Poly(p-hydroxystyrene) grafted onto the

surface of polystyrene nanospheres have also been employed to stabilize supported metal nanoparticles[282].

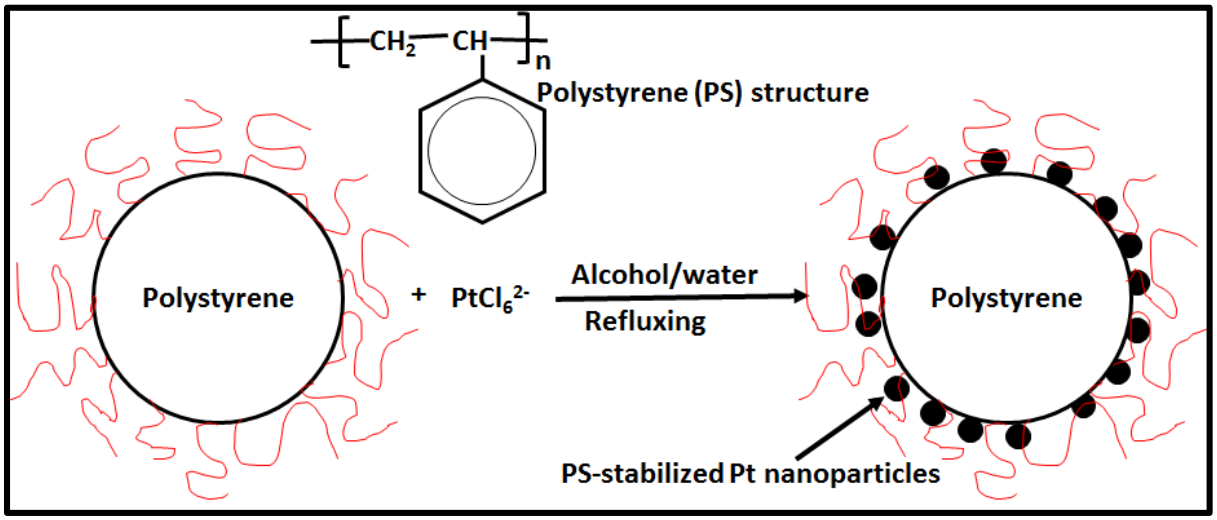

Figure 2.10: Illustration of Pt nanoparticles supported on polystyrene (PS) microspheres (redrawn after Akashi *et al.*)[280, 283].

2.6.3 Adsorption of Nanoparticles onto Supports

The adsorption of colloidal suspension of metal nanoparticles onto various supports is the most widely employed route to prepare contact metal nanocatalysts.[13-16, 19-21, 251-271] This is a three-step process which involves the synthesis of colloidal metal nanoparticles using a chemical solution-based protocol, followed by their impregnation onto the support and finally washing the solid products[98]. Nanoparticles have been impregnated into a variety of supports such as silica[251-256], carbon[13-16, 19-21, 264-267], alumina[257-263], titania[268-270], etc. The most widely used supports to generate heterogeneous metal nanoparticle catalysts are carbon supports.

2.7 Electrochemical Measurements (Characterization Methods) of Electrocatalysts

Electrochemical measurements are heterogeneous reactions performed *ex-situ* in half-cells to evaluate the functionality of electrocatalyst nanomaterials, as shown in Figure 2.11[4]. The catalyst-carbon support-Nafion membrane (solubilized Nafion) and the glassy carbon (GC) disk electrode form the so-called working electrode (the main component of interest during the catalytic evaluation of nanocatalysts). GC is used as the disk material and catalyst immobilizer due to its conductivity and electrochemical inertness over the wide range of electrode potentials

for the screening of the ORR functionality. The Nafion membrane solution functions to adhere or immobilize the electrocatalyst carried on the carbon material to the GC disk [4].

The reference electrode is non-polarizable and functions to reduce the electrolyte solution resistance on the working electrode potential (sustains the steady potential), without interfering with the mass transfer of the reacting species to the surface of the working electrode[4]. High surface area Pt wire is commonly used as the counter electrode material because it is chemically inactive and does not corrode or decompose electrocatalytically. The surface reactions occurring at the Pt wire should not exhibit any mass-transport limitations[4]. The evaluation of the experiments for the catalytic activity of nanocatalysts carried on carbon support materials is performed in the electrolyte solution purged with gases such as nitrogen (N_2), argon (Ar), oxygen (O_2) or carbon monoxide (CO).

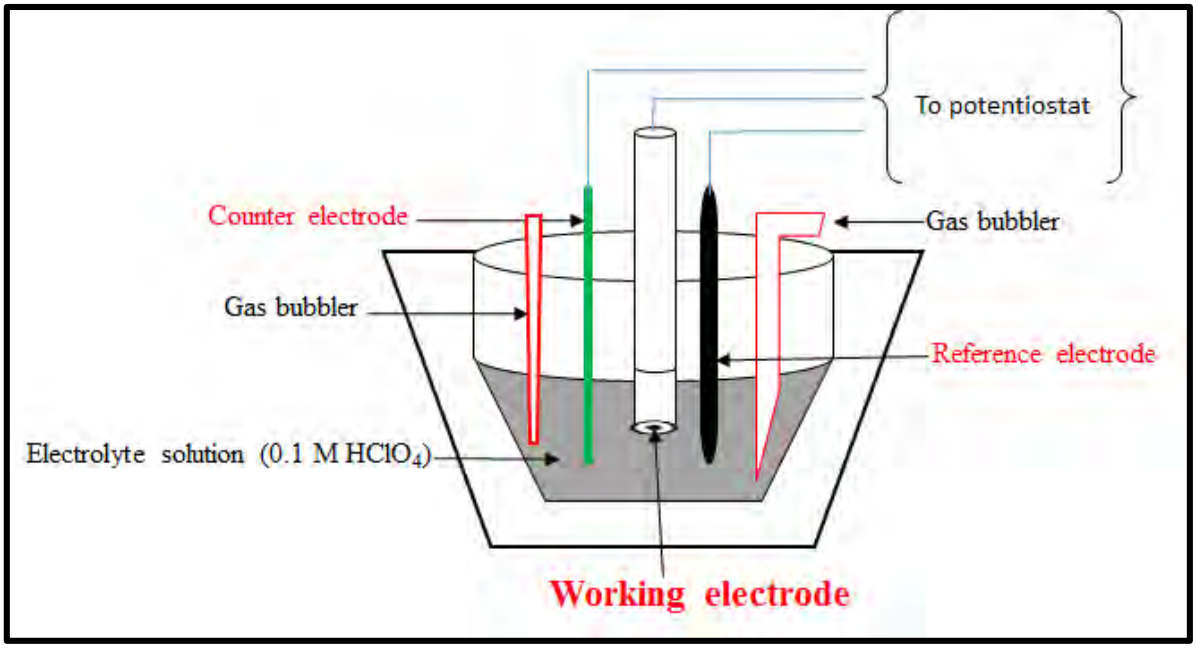

Figure 2.11: Schematic representation of a typical 3-electrode half-cell structure (redrawn after Zhang)[4].

2.7.1 Formulation of the Working Electrode

The catalytic investigation or screening of novel electrocatalysts to study the reaction mechanisms and kinetics is performed by coating clean and mirror polished glassy carbon (GC) electrodes with a layer of catalyst-carbon support-Nafion membrane (solubilized Nafion)[4]. The catalyst inks are formulated by suspending the carbon-carried catalyst in a mixture of

water, alcohol and Nafion-ionomer membrane solution. Depending on the nature of the catalysts, the ink formulation may differ. Good catalyst inks should be homogeneous and yield uniform films over the GC[4]. For instance, hydrophobic stabilizers form inherently hydrophobic colloids whereas hydrophilic stabilizers lead to hydrophilic colloids. Therefore, in order to obtain high quality ink with optimal suspension the alcohol to water ratios must be adjusted[284]. Hydrophobic catalysts may require higher alcohol content to water ratios to achieve uniform and crack-free films while hydrophilic catalysts can suspend well in a simple mixture of Nafion ionomer solution and water[284]. From the initial known amount of catalyst used for the ink suspension and the known volume deposited onto the GC electrode, the amount of catalyst in the thin film can be estimated[284].

2.7.2 Electrolyte Selection

Electrochemical measurements are conducted in dilute aqueous acid solution. The selection of a non-adsorbing electrolyte is key to ensure that no anion species adsorb on active Pt catalyst surface and thereby deactivating its functionality[4]. Halide anions such as chloride (Cl^-), fluoride (F^-), bromide (Br^-) have detrimental effects on the Pt electrocatalysts to facilitate the ORR activity[285-287]. Perchloric acid ($HClO_4$) is most widely used as the electrolyte because its perchlorate anions (ClO_4^-) do not adsorb on the surface of Pt catalysts, thus rendering $HClO_4$ a better candidate for the characterization of PEMFC electrocatalysts[4, 288]. Although Nafion membrane is used as an additive to enhance the adhesion of the carbon-carried catalysts onto the surface of the working electrode, its anion ($CF_3SO_3^-$) is non-adsorbing and does not influence the ORR kinetics[4].

2.7.3 Evaluation of Catalyst Activity

The investigations of the hydrogen oxidation reaction (HOR) and oxygen reduction reaction (ORR) are performed using cyclic voltammetry (CV), or carbon monoxide stripping (CO-stripping) or linear sweep voltammetry (LSV) measurements, respectively. CV provides detailed information of the electrochemical reactions occurring on the electrocatalyst active surface sites whereas rotating ring disk (RDE) offers quantitative evaluation of the kinetics and mechanism of the electrocatalytic reactions. CO-stripping is particularly fundamental for the study of alloyed catalysts as the addition of the promoter metal may affect the hydrogen

adsorption/desorption. RDE is used in the determination of the functionality of electrocatalysts toward the ORR.

2.7.3.1 Cyclic Voltammetry (CV)

CV is a well-established technique for characterizing metal surfaces and investigating electrocatalysts performance in an electrolyte solution[289-291]. For carbon-carried electrocatalysts, detailed investigation of the metal surface characteristics is performed in an aqueous acidic environment[289-291]. Figure 2.12 shows a typical CV of Pt-based electrocatalyst supported on a high surface carbon black (Vulcan XC-72R) in argon-purged aqueous acidic media. The CV voltammogram is divided into three regions: (1) hydrogen regime, (2) double layer regime and (3) oxide growth regime[292].

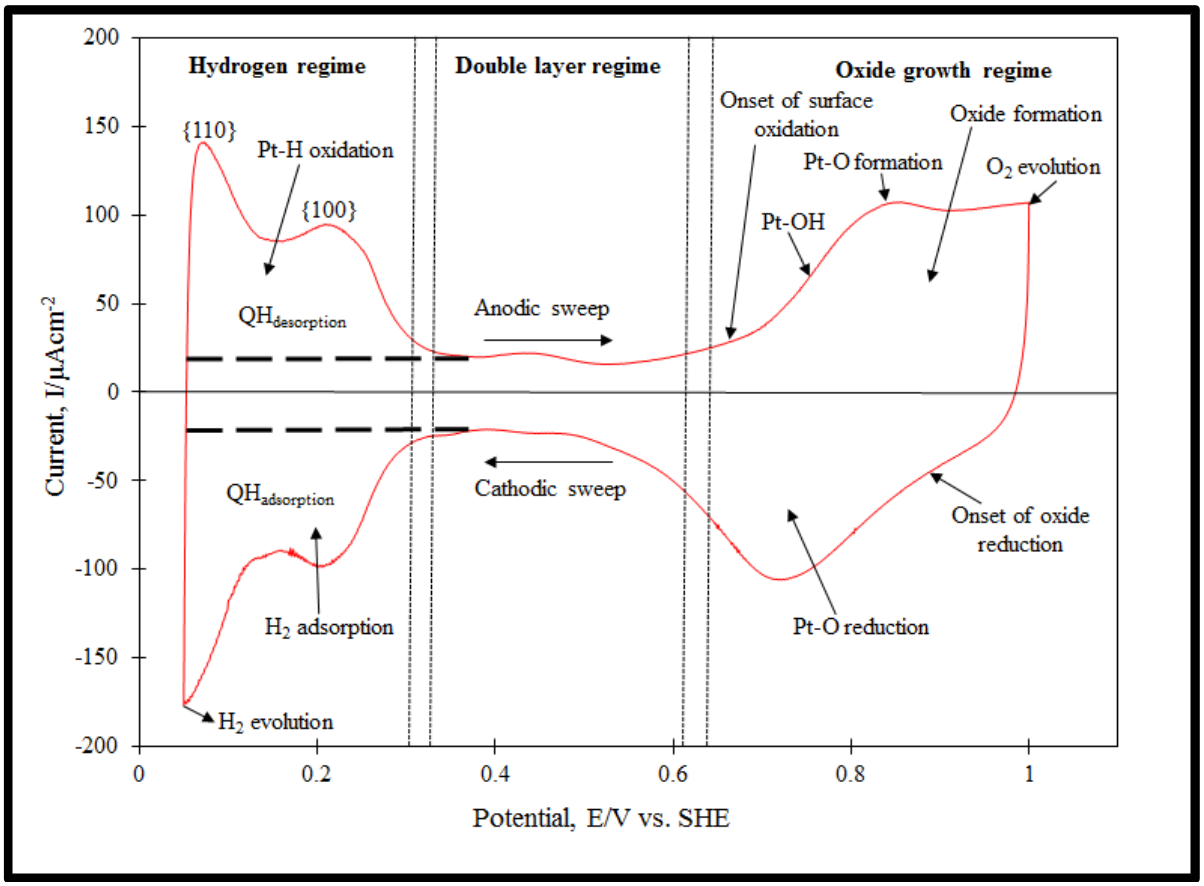

Figure 2.12: Typical cyclic voltammogram of a Pt-based electrocatalyst in Argon (Ar)-saturated 0.1 M $HClO_4$ media (redrawn after Jerkiewicz *et al.*)[292].

(1) **Hydrogen region**: This region is characterized by the underpotential deposition of hydrogen (H_{upd} region) onto the electrocatalyst surface where H_{upd} region represents the

surface-adsorbed/desorbed hydrogen because the process is reversible. During the desorption process (anodic sweep) at lower potentials than 0.3 V (versus standard hydrogen electrode, SHE), the under-potentially deposited $H^+_{(aq)}$ ions are oxidized and the adsorbed hydrogen desorbs from the catalyst surface into the acidic electrolyte[4, 293]:

$$Pt\text{-}H_{ads} \rightarrow Pt + H^+_{(aq)} + e^-$$

Depending on the structure of the electrocatalysts, hydrogen desorption occurs at different Pt catalyst surface sites resulting in distinct hydrogen peaks. At the {110} surface sites, the hydrogen is strongly bound whereas at {100} surface sites the binding is weak[293]. During the cathodic scan, hydrogen adsorption mainly takes place at the {110} and {100} surface sites. These surface sites correspond with the peaks obtained during the anodic scan. Thus, the reduction of $H^+_{(aq)}$ in the electrolyte forms the adsorbed hydrogen adatoms (H_{ads}) at potentials lower than 0.3 V[4]:

$$Pt + H^+_{(aq)} + e^- \rightarrow Pt\text{-}H_{ads}$$

The potential sweeping direction (cathodic scan) of the system is switched off before hydrogen evolution initiates. When the potential approaches zero (and more negative values), the hydrogen evolution occurs as follows[4]:

$$2Pt\text{-}H_{ads} \rightarrow 2Pt + H_2$$

In the hydrogen regime, the adsorption and desorption peaks determine the electrochemical active surface (ECSA) of the electrocatalysts for one electron transferred per catalyst site. The ECSA is calculated from either the hydrogen desorption or adsorption area and is given by the following equation[4, 284]:

$$\text{ECSA } (m^2 g_{Pt}^{-1}) = \left\{ \frac{Q_{H-\text{desorption (or adsorption)}}\ \mu C}{(210\ \mu C\ cm^{-2}) L_{Pt} (mg_{Pt}\ cm^{-2}) A g (cm^2)} \right\}$$

where $Q_{H\text{-desorption or adsorption}}$ ($\mu C\ cm^{-2}$) is the charge measured from the hydrogen desorption (H_{des}) or adsorption (H_{ads}) area, the charge associated with a monolayer of hydrogen adsorbed

on polycrystalline Pt is 210 μC cm^{-2}, L_{Pt} is the working electrode catalyst loading ($mg_{catalyst}$ cm^{-2}) and Ag (cm^2) is the geometric surface area of the glassy carbon electrode[284].

(2) **Double layer region**: The double layer region for Pt occurs at potentials between 0.4 V and 0.7 – 0.8 V. The decrease in current from 0.25 V – 0.7 V (or 0.8 V) is due to the double layer charging, the removal of the H_{ads}, the adsorption of anions and water. This is followed by the formation of OH_{ads} at the catalyst active sites. Below 0.7 – 0.8 V, there are no oxides or hydroxyls formed on the catalyst surface. However, the width of the double layer region is proportional to the current density/sweep rate (the capacitance of the electrode) and is also determined by the surface area of the electrode itself[294].

(3) **Oxide growth region**: The electrochemical oxidation of metal surfaces occurs by direct chemisorption with oxygen molecules or via the oxidation of water in acidic aqueous media. These surface oxide and oxygen-containing intermediate moieties are well-known to hinder the functionality of electrocatalysts toward ORR. The oxide growth on metal surfaces influences the mechanism and reaction kinetics by[295, 296]:

(a) modifying the electronic properties of the metal active sites,

(b) inducing a barrier to charge transfer across the surface of the oxide layer,

(c) affecting the adsorption and desorption of reaction intermediates and products, respectively, at the metal surface, and

(d) influencing the thermodynamics of the reaction at the double layer regime[295, 296].

2.7.3.2 Carbon Monoxide (CO) Stripping Voltammetry

CO-stripping voltammetry is an alternative strategy (operates under the same principle as CV) commonly employed to determine the ECSA of electrocatalysts. During CO-stripping, the electrocatalyst is deliberately poisoned with a monolayer of reversibly adsorbed carbon monoxide (CO_{ads}) by purging the electrolyte with CO gas, followed by purging out any CO gas from the electrolyte not adsorbed on the catalyst surface with argon, under potential control[4,

[297]. Thereafter, the potential scan is performed to induce the electrochemical oxidation of Pt surface adsorbed CO (Pt-CO_{ads}). This method is, however, valid for binary or ternary alloy nanosystems because the incorporation of the promoter metal (alloying metal) might have influence in the hydrogen regime[4, 298].

CO adsorption is confirmed in the double layer regime during the anodic potential scan, resulting in the evolution of a sharp and well-defined transient positive current CO peak, as shown in Figure 2.13[298]. This current is due to the displacement of adsorbed hydrogen (H_{ads}) by CO as CO is the stronger adsorbate than hydrogen[297]:

$$Pt\text{-}H_{ads} + CO \rightarrow Pt\text{-}CO_{(ads)} + H^{+}_{(aq)} + e^{-}$$

The second cycle (dashed line) of both the cathodic and anodic scans exhibits no existence of a CO peak, indicating the complete elimination of excess CO from the electrolyte and that the CO investigation was performed exclusively on the CO_{ads} monolayer (adlayer) on Pt electrocatalysts[297, 298].

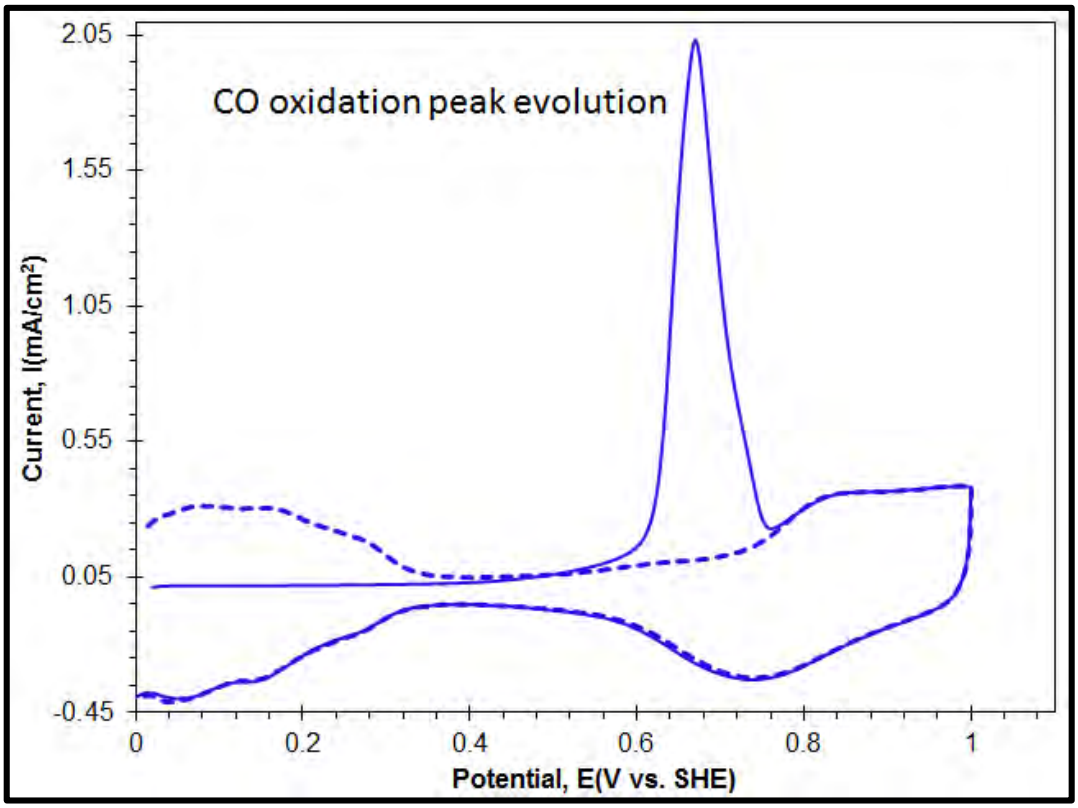

Figure 2.13: CO-stripping voltammetry on Pt-based alloy/Vulcan film supported on a glassy carbon disk electrode in 0.1 M $HClO_4$ at room temperature (redrawn after Sugimoto *et al.*)[298].

During CO adsorption, most H_{ads} are displaced and the oxidation of the remaining H_{ads} creates more CO-free sites. These CO-free regions promote the formation and adsorption of the hydroxyl groups (OH_{ads})[299]. These oxygen-containing species evolve from the dissociation of the adsorbed water. The adsorption of anions and water with the CO_{ads}, more OH_{ads} species are produced, leading to the complete electrochemical CO_{ads} oxidation to CO_2[4]:

$$Pt\text{-}CO_{ads} + H_2O \rightarrow Pt + CO_2 + 2H^+_{(aq)} + 2e^-$$

Therefore, at higher potentials of about $0.4 < E < 0.8$ V, the CO_{ads} adlayer is completely removed. The electrochemical conversion of CO to CO_2 is a two-electron mechanism. The charge associated with stripping one monolayer of adsorbed CO_{ads} adlayer on polycrystalline Pt is 420 μC cm^{-2}, when one Pt atom is covered by one CO molecule in a linear adsorption configuration (Pt-CO_{ads})[300, 301]. In the case where one CO molecule occupies two Pt atoms, in the bridge adsorption configuration (2Pt-CO_{ads}), the charge associated with CO-stripping is 210 μC cm^{-2}[4, 302]. The adsorption of CO on the surface of the Pt is influenced by the potential and thus at potentials near zero (0 V), the CO adsorption follows the linear adsorption structure (Pt-CO_{ads})[303]. The ECSA is therefore calculated by integrating the charge associated with the CO stripping and correlating it with the established value of 420 μC cm^{-2}, as follows[298]:

$$\text{ECSA } (m^2 g_{Pt}^{-1}) = \left\{ \frac{Q_{CO-\text{ adsorption}}\ \mu C}{(420\ \mu C\ cm^{-2}) L_{Pt} (mg_{Pt}\ cm^{-2}) A g (cm^2)} \right\}$$

The full coverage of a CO monolayer on Pt is sufficient to inhibit hydrogen adsorption. As shown in Figure 2.13 (the dashed cycle in blue), the desorption peaks are featureless at potentials < 0.4 V. At higher potentials in the range: $0.4 < E < 0.8$ V, the CO monolayer is removed completely, resulting in the availability of Pt active surface sites for both hydrogen adsorption and desorption. Hence, the re-emergence of the corresponding adsorption and desorption peaks (the solid cycle in blue) is observed[4].

The incomplete oxidation of CO may, however, lead to the formation of a stable CO_{ads} adlayer. In addition, CO-stripping voltammetry is also useful in investigating the reaction mechanism of metal alloys with improved CO tolerance[304-306]. In addition, exposing Pt with CO and its

subsequent electrochemical stripping (removal) is another efficient mechanism of cleaning and improving the functional activity of Pt[297].

2.7.3.3 Rotating Disk Electrode (RDE)

The electrode surface processes involve heterogeneous charge-transfer kinetics and mass transfer that determine the surface concentrations of electroactive species. RDE is used to probe functionality towards ORR in a linear potential sweep fashion. The linear sweep voltammetry (LSV) in Figure 2.14 shows the cathodic polarization curve for the ORR activity, performed on a thin electrocatalyst film immobilized on a glassy carbon (GC) electrode[284].

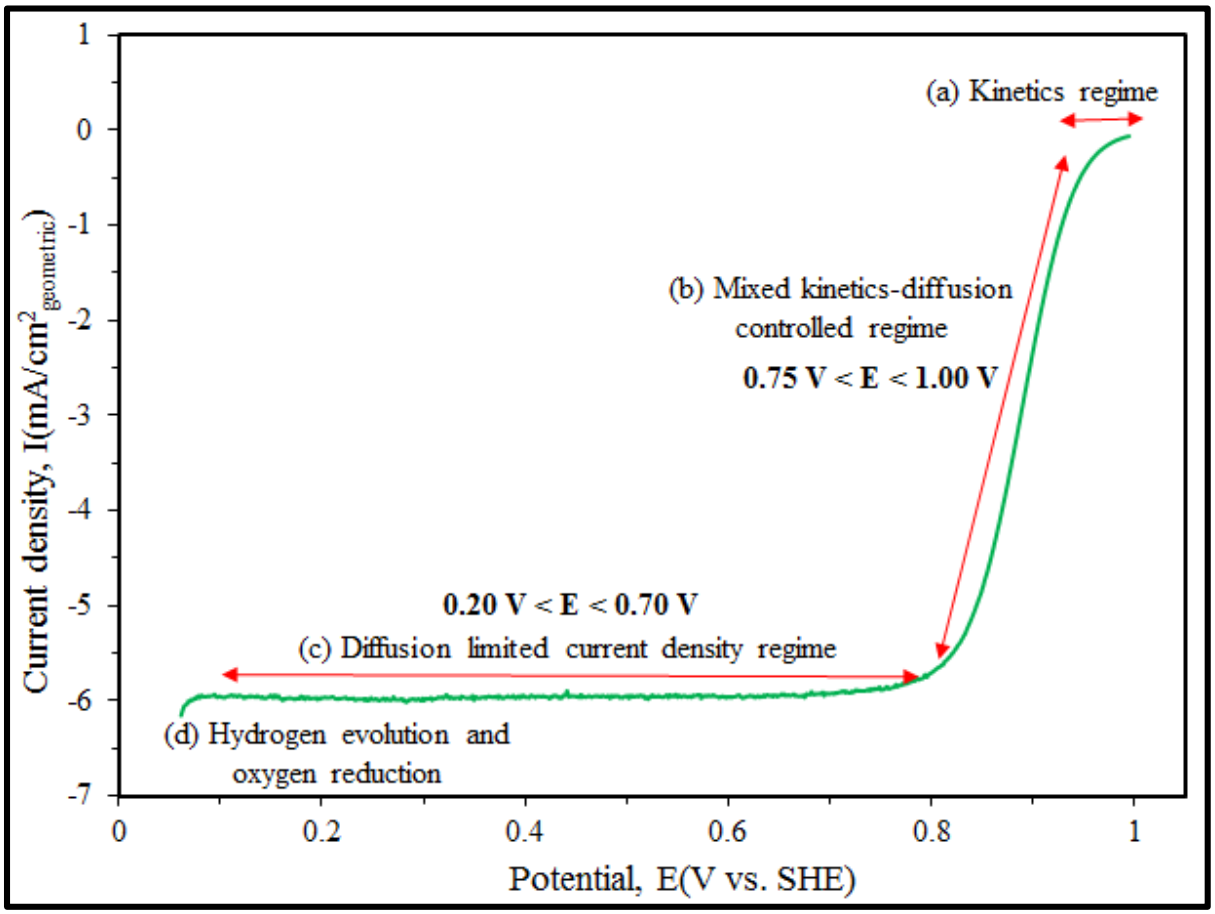

Figure 2.14: A typical cathodic current-potential curve (ORR polarization curve) recorded at 1600 rpm on Pt alloy/Vulcan film immobilized on a glassy carbon disk electrode in an oxygen saturated 0.1 M $HClO_4$ at room temperature (redrawn after Garsany)[284].

The ORR polarization (current-potential) curve in Figure 2.14 is divided into four regimes:

(a) **Kinetics regime** - dissolved oxygen species, which are conveyed from the bulk electrolyte solution to the surface of the working electrode, are influenced by the rotation speed of the RDE. Electro-catalytic reactions occur when electroactive species reach the surface of the working electrode. The reaction onset potential, which occurs at higher potentials enough to persuade the reaction, the current is controlled by the reaction kinetics. At this potential the mass transfer of molecular oxygen becomes less important.

(b) **Mixed kinetics-diffusion controlled regime** - the reaction rate is influenced by the mass transfer rate of the electroactive oxygen species to the electrode surface at a given rotation speed. Within this region, the current is affected by both the reaction kinetics and mass transport rate (surface concentrations of oxygen species). The mass transport increase is determined by the rotating electrode rate. The rate of mass transfer of dissolved oxygen to the electrode surface increases with increasing the RDE rotation speed.

(c) **Diffusion limited current density regime -** the current is approximately constant, resulting in a steady mass transfer profile. Thus, the rate at which dissolved oxygen reaches the electrode surface approaches zero. It is within this regime of complete mass transfer control that the reaction is entirely flow-dependent; thus the rate at which oxygen species move is the rate determining step that affects the transfer of oxygen to the electrode surface.

(d) **Hydrogen evolution and oxygen reduction regime** - as the potential of the system becomes more negative, two simultaneous processes take place where oxygen is reduced and hydrogen evolves:

$$2H_2O + 2e^- \rightarrow H_2 + 2OH^-$$

The potential scan rate with respect to the electrode rotation rate must be sluggish enough to obtain a steady-state reactant species concentration profile. The ORR experimental measurements are performed from 1.03 V (cathodic scan) → 0.05 V (anodic scan) → 1.03 V at the sweep rates of 5, 10 and/or 20 mV/s[284]. At higher scan rates, the capacitive current interferences are higher and contribute to decreased ORR catalytic activity. Although capacitive current contributions are lower at lower scan rates, the ORR functionality is suppressed due to the adsorption of hydroxyl groups (OH_{ads}) on active Pt sites and subsequent

gradual Pt-oxide evolution. In addition, the presence of any impurities in the electrolyte can contaminate the electrode and thereby negatively impacting on the ORR activity[284].

The current density (i) for the ORR electrocatalytic activity is calculated according to Koutecky-Levich equation[11, 307, 308]:

$$\frac{1}{i} = \frac{1}{i_k} + \frac{1}{i_d}$$

where i is the overall disk current density, i_k is the true kinetic current density ($A\ cm^{-2}$) and is determined by the mass transport properties of the RDE, i_d is the diffusion limited current density. i_d can be expressed according to Levich equation as follows:

$$i_d = 0.620 n_e F A {D_{O_2}}^{2/3} V^{-1/6} {C_{O_2}}^{\infty} \omega^{1/2}$$

where n_e is the total number of electrons transferred ($4e^-$), F is the Faraday's constant (96485 C/mol), A is the surface area of the electrode (0.196 cm^2), D_{O_2} is the diffusion coefficient of oxygen (1.93 x 10^{-5} cm^2/s), C_{O_2} is the concentration of dissolved oxygen (1.26 x 10^{-6} mol/cm^3), V is the kinematic viscosity of the electrolyte solution (1.01 x 10^{-2} cm^2/s) at 20 °C and ω is the angular frequency of rotation, $\omega = \frac{2\pi f}{60}$, f is the RDE rotation rate in rpm: for the measurements conducted in 0.1 M $HClO_4$ at 20 °C and 1 atm O_2. The diffusion coefficient of oxygen, the kinematic viscosity of the electrolyte solution and the concentration of dissolved oxygen are classified as non-electrochemical kinetic characteristics required for RDE data analysis. These kinetic parameters are influenced by temperature and the electrolyte solution during the electrochemical measurements[4, 119, 294].

In order to determine the mass-transport free kinetic current (i_k), the ORR measurements are conducted at the rotation speed of 1600 rpm. This rotation rate is used as the benchmark to compare the functionality of electrocatalysts and the ORR polarization limiting current ranges between 5.8 x 10^{-3} – 6 x 10^{-3} A cm^{-2}[87, 309-311]. These limiting current values yield n = 4 for the Levich and Levich-Koutecky plots. Furthermore, background current measurements are performed in deaerated electrolyte solution to account for capacitive current interferences. The difference between the experimentally measured current and the background current yields

mass-transport corrected current. This current is used to evaluate mass-and area-specific activities of catalysts. Since at the limiting current the reaction kinetics occur very fast, the Koutecky-Levich equation can be re-arranged as follows[11, 284, 308, 310, 311];

$$I_k\ (mA\ cm^{-2}) = \frac{I_{lim}\ (mA\ cm^{-2})\ x\ I(mA\ cm^{-2})}{(I_{lim} - I)\ (mA\ cm^{-2})}$$

where $I_{lim} = i_d$ is the measured diffusion limited current density and I_k is the kinetic current (A). The I and I_{lim} are the values calculated from the anodic ORR polarization curve at E = 0.9 V and E = 0.4 V versus SHE, respectively[284].

The Pt mass-specific (I_m) and area-specific (I_s) activities are quantified at E = 0.9 V versus SHE specifically because the contributions from mass-transport losses cannot be totally disregarded at the higher current densities detected below E = 0.9 V[284, 310-312]. Therefore, the Pt mass-specific activity is calculated from the I_k and normalization to the Pt-loading of the GC disk electrode[284, 310-312]:

$$I_{m(0.90V)}(A\ \mathrm{mg_{Pt}}^{-1}) = \frac{I_k\ (A\ cm^{-2})}{L_{\mathrm{Pt}}[\![(\mathrm{mg}]\!]_{\mathrm{Pt}}\ \mathrm{cm}^{-2})}$$

L_{Pt} is the working electrode catalyst loading ($\mathrm{mg_{catalyst}\ cm^{-2}}$) and Ag ($\mathrm{cm^2}$) is the geometric surface area of the glassy carbon electrode.The area-specific activity is determined from the I_k and normalization with the Pt electrochemical surface area (ECSA)[284, 310-312]:

$$I_{s(0.90V)}(mA/cm^2) = \frac{I_k\ (mA)}{ECSA}$$

$$= \frac{I_k\ (A)}{(\mathrm{Q_{H-desorption\ (or\ adsorption)}(C)/210\ \mu C\ cm^{-2})}Ag(\mathrm{cm^2})}$$

2.8 Summary

There is a large body of scientific research on the design, synthesis, characterisation and testing of catalyst nanoparticles. Platinum nanoparticles remain the standard as catalysts for PEMFCs because of their excellent catalytic functionality; the cost, however, of platinum is prohibitive.

Investigations surveyed in this chapter, have been used as a guide to development of synthesis protocols for nanoparticles which are outstanding PEMFC catalysts, improving on the pure platinum standard. The synthesis, characterisation and testing of novel platinum alloy nanoparticles is presented in the following chapters.

CHAPTER 3 METHODS

This chapter describes the experimental methods use to synthesize and characterise alloy nanoparticles. This includes synthesis of Pt alloy nanoparticles, their structure characterisation by TEM and XRD, and electrochemical testing.

3.1 Synthesis of Colloidal Bimetallic and Trimetallic Nanoparticles

The basic requirements for nanoparticle synthesis employing chemical reaction mixtures include metal precursor salts, solvents, surface-active agents (surfactants), and reducing agents (reductants or reducers). In most cases it is necessary to heat the reaction media from room temperature to an appropriate higher temperature to induce reduction of metal precursor salts. The solvents are used to dissolve and ensure the homogeneity of the reaction mixtures prior to synthesis of nanoparticles. The surfactants serve to regulate nanoparticle growth by forming a protective shell, suppressing growth at a particular size, and also inhibit the degree of oxidation of nanoparticles. In this case, the mixtures of two or more different surfactants within the same synthesis system were used to promote anisotropic growth which can be triggered by selective/preferential adsorption of specific surfactants on distinct crystallographic facets of the growing crystals, leading to distinct crystallographic growth directions. Thus, the growth kinetics of nanoparticles can be induced and influenced by the nature of surfactants employed during synthesis. Reductants (reducers) induce the reduction of metal ions by donating electrons, hence become oxidized. Bi- and tri-metallic nanoparticles of a variety of homogeneity, composition, size, morphology and dispersion can be synthesized by deploying different metal precursor salts, solvents, surfactants and reductants. Reduction of two (or more) different metal salts can be carried out by co-reduction, by sequential reduction, or by a combination of the two.

3.1.1 Synthesis of PtNi Binary Nanoparticles

Table 3.1 summarizes the different synthesis protocols deployed for the preparation of Pt-Ni nanoparticles using co-reduction and sequential synthetic procedures in the presence and absence of the reductant. The experimental parameters varied include metal precursor salts, surfactants, reductants and solvents.

Table 3.1: The preparation methods of Pt-based bimetallic nanoparticles.

Precursors[a]	Surfactant(s)[b]	Solvent(s)[c]	Reductant(s)[d]	Approach[e]
3.1.1.1: H_2PtCl_6 + Ni(Ac)	OAm + ODA + OLEA	1-OD	OAm + ODA + OLEA + T	CR
	OAm + ODA + DOA	1-OD	OAm + ODA + DOA + T	CR
	OAm + ODA + TOA	1-OD	OAm + ODA + TOA + T	CR
3.1.1.2: H_2PtCl_6 + Ni(Ac)	OAm + ODA + OLEA	1-OD	OAm + ODA + OLEA + T	SR
	OAm + ODA + DOA	1-OD	OAm + ODA + DOA + T	SR
	OAm + ODA + TOA	1-OD	OAm + ODA + TOA + T	SR
3.1.1.3: H_2PtCl_6 + Ni(Ac)	OAm + ODA + OLEA	1-OD	TBAB	CR
	OAm + ODA + TOA	1-OD	TBAB	CR

[a] H_2PtCl_6 = chloroplatinic acid; Ni(Ac) = nickel (II) acetate, [b] OAm = oleylamine; ODA = octadecylamine; OLEA = oleic acid; DOA = dioctylamine; TOA = trioctylamine; [c] OAm = oleylamine; 1-OD = 1-octadecene; [d]OAm = oleylamine; ODA = octadecylamine; OLEA = oleic acid; TBAB = tetrabutylammonium borohydride; T = reduction temperature [e] CR = co-reduction; SR = sequential reduction

3.1.1.1 Co-reduction by Thermolysis

In a typical synthesis: 0.072 g Ni(Ac) and 0.33 g H_2PtCl_6 (precursor salts), 20 ml OAm, 2.4 g ODA and 20 ml OLEA (surfactants) were dissolved in 25 ml 1-OD (solvent) by sonication (via ultrasound bath) for 20 minutes. The resulting solution was then heated to150 °C, then held for 5 – 10 minutes under vigorous magnetic stirring in a beaker on a hotplate and transferred into a round bottom flask. The resultant pale yellow homogeneous solution was subsequently heated to 240 °C (measured using a thermometer) for 30 – 40 minutes. Both the reduction temperature and the surfactants acted to reduce precursor salts. The effect of surfactants on the structural evolution of these nanoparticles was investigated by replacing OLEA with TOA and DOA while keeping the other reaction parameters identical. The separation-purification-resuspension processes of the as-prepared colloidal solution were repeated several times to remove all the unwanted solvents and surface-unbound surfactants. The black product was finally re-dispersed in chloroform, yielding a dark brown colloidal suspension.

3.1.1.2 Sequential Reduction by Thermolysis

In a standard sequential method: 0.036 g Ni(Ac), 2.4 g ODA, 20 ml OAm and 20 ml OLEA (surfactants) were dissolved in 25 ml 1-OD (solvent) by sonication for 20 minutes and heated at 150 °C until a pale yellow solution was observed under vigorous magnetic stirring. Thereafter, the reaction temperature was raised to 240 °C and maintained for 15 – 20 minutes. The resultant pale brown solution was cooled down to 150 °C, added to 0.17 g H_2PtCl_6 and

sonicated for 20 minutes prior to heating to 240 °C. The reaction mixture was held at this reduction temperature for 30 – 40 minutes. The effect of the surfactants was also investigated by replacing OLEA with DOA and finally TOA. The as-synthesized colloidal nanoparticles were separated and washed several times to eliminate any unwanted solvents and unattached surfactants by addition of excess ethanol.

3.1.1.3 Co-reduction by Reductant

In a standard co-reduction procedure: 0.03 g Ni(Ac) and 0.09 g H_2PtCl_6 (precursor salts), 15 ml OAm, 4.4 g ODA and 15 ml OLEA (surfactants) were dissolved in 25 ml 1-OD (a high boiling point solvent) by sonication for 20 minutes and heated at 150 °C until a pale yellow solution was observed under vigorous magnetic stirring. After the addition of 0.05 g TBAB (reductant), the reaction temperature was subsequently raised to 240 °C and maintained for 30 – 40 minutes. The effect of the surfactants was also investigated by replacing OLEA with TOA. The black products were isolated and purified by the addition of excess ethanol to precipitate the particles. The separation-precipitation process was performed three times to eliminate any unbound surfactants on the surfaces of the nanoparticles, the black product dried and finally re-suspended in chloroform.

3.1.2 Synthesis of Pt-based Binary and Ternary Nanoparticles

Table 3.2: The preparation methods of Pt-based binary and ternary nanoparticles.

Precursors[a]	Surfactant(s)[b]	Solvent(s)[c]	Approach[d]
3.1.2.1: $Pt(acac)_2$ + Ni(Ac)	OAm + TOA + OLEA	1-OD + OAm	CR
3.1.2.2: $Pt(acac)_2$ + Co(Ac)	OAm + TOA + OLEA	1-OD + OAm	CR
3.1.2.3: $Pt(acac)_2$ + Ni(Ac) + Co(Ac)	OAm + TOA + OLEA	1-OD + OAm	CR

[a] $Pt(acac)_2$ = platinum (II) acetylacetonate; Ni(Ac) = nickel (II) acetate; Co(Ac) = cobalt (II) acetate; [b] OAm = oleylamine; TOA = trioctylamine; OLEA = oleic acid; [c] OAm = oleylamine; 1-OD = 1-octadecene; [d] CR = co-reduction

3.1.2.1 Synthesis of PtNi Nanoparticles: Co-reduction by Thermolysis

In a standard co-reduction method: 0.12 g Ni(Ac) and 0.2 g $Pt(acac)_2$ (precursor salts), 20 ml OAm, 15 ml TOA and 5 ml OLEA (surfactants) were dissolved in 25 ml 1-OD (solvent) by sonication for 20 minutes. The resulting solution was then heated at 150 °C for 5 – 10 minutes under vigorous magnetic stirring. The reaction mixture turned into a transparent yellowish

solution and was then transferred into a one-neck round bottom flask and the reaction temperature was raised to 300 °C. The reaction time was 15 – 20 minutes. The resultant dark brown colloidal solution was allowed to cool down to 100 °C, followed by the addition of excess ethanol to precipitate the particles. The separation-precipitation process was repeated three times to remove all unwanted solvents and the surface unattached surfactants; the black final product was dried and re-suspended in chloroform for more in-depth compositional and morphological investigations.

3.1.2.2 Synthesis of PtCo Nanoparticles: Co-reduction by Thermolysis

In a standard co-reduction method: 0.12 g Co(Ac) and 0.2 g $Pt(acac)_2$ (precursor salts), 20 ml OAm , 15 ml TOA and 5 ml OLEA (surfactants) were dissolved in 25 ml 1-OD (solvent) by sonication for 20 minutes. The resulting solution was then heated at 150 °C for 5 – 10 minutes under vigorous magnetic stirring. The corresponding reaction mixture was transferred into a round bottom flask and the reaction temperature was raised to 300 °C. The reaction time was 15 – 20 minutes. The resultant dark brown colloidal solution was allowed to cool down to 100 °C, followed by the addition of excess ethanol to flocculate and precipitate the particles. The separation-precipitation process was carried out three times to remove the solvents and unbound surfactants; the black product was dried and finally re-suspended in chloroform for auxiliary characterization.

3.1.2.3 Synthesis of Pt(NiCo) Nanoparticles: Co-reduction by Thermolysis

In a standard synthetic procedure: 0.06 g Ni(Ac), 0.06 g Co(Ac) and 0.2 g $Pt(acac)_2$ (precursor salts), 20 ml OAm , 15 ml TOA and 5 ml OLEA (surfactants) were dissolved in 25 ml 1-OD (solvent) by sonication for 20 minutes. The resulting mixture was then heated at 150 °C for 5 – 10 minutes under vigorous magnetic stirring. The homogeneous reaction mixture was then transferred into a round bottom flask and the reaction temperature was rapidly raised to 300 °C. The reaction time was 15 – 20 minutes. The resultant dark brown colloidal solution was allowed to cool down to 100 °C, followed by the addition of excess ethanol to precipitate the particles. The separation-precipitation process was performed three times to get rid of all the undesirable solvents and unbound surfactants; the black final product was re-suspended in chloroform for further detailed characterization.

3.1.3 Synthesis of Ternary PtNiV-based alloy Nanoparticles

Table 3.3: The preparation methods of PtNiV ternary nanoparticles.

Precursors[a]	Surfactant(s)[b]	Solvent(s)[c]	Approach[e]
3.1.3.1: H_2PtCl_6 + Ni(Ac) + $V(acac)_3$	OAm + ODA	1-OD + OAm	SR
H_2PtCl_6 + Ni(Ac) + $V(acac)_3$	OAm + ODA + OA	1-OD + OAm + OA	SR

[a] H_2PtCl_6 = chloroplatinic acid; Ni(Ac) = nickel (II) acetate, $V(acac)_3$ = vanadium (III) acetylacetonate [b] OAm = oleylamine; OA = oleyl alcohol; ODA = octadecylamine; [c] OAm = oleylamine; 1-OD = 1-octadecene; [d] OAm = oleylamine; ODA = octadecylamine; OA = oleyl alcohol; [e] SR = sequential reduction

3.1.3.1 Sequential Reduction by Thermolysis

(a) In a typical sequential reduction method: a 0.24 g $V(acac)_3$ metal precursor salt was dissolved in 15 ml OAm and 4.4 g ODA (surfactants) in a high-boiling point, 20 ml 1-OD, followed by sonication for 20 minutes. The resultant solution was then heated to 300°C for 30 minutes and allowed to cool down to 150 °C. Thereafter, 0.06 g Ni(Ac) and 0.33 g H_2PtCl_6 (precursor salts) dissolved in 5 ml OAm and 5 ml 1-OD, were added and the solution was rapidly heated to 310 °C for 30 – 40 minutes. The reduction of the metal precursor salts was influenced by both the reduction temperature and the surfactants. The resulting colloidal solution was allowed to cool to room temperature, followed by the addition of excess ethanol to precipitate the particles. The separation-precipitation process was performed three-four times, the black product was dried and finally re-suspended in chloroform.

(b) A similar protocol was deployed to form ternary V-PtNi nanoparticles but in the presence of OA as an additional surfactant. A 0.24 g $V(acac)_3$ metal precursor salt was dissolved in 15 ml OAm, 10 ml OA and 4.4 g ODA (surfactants) in a high-boiling point, 20 ml 1-OD, followed by sonication for 20 minutes. The resultant solution was then heated to 300 °C for 30 minutes and allowed to cool down to 150 °C. Thereafter, 0.06 g Ni(Ac) and 0.33 g H_2PtCl_6 (precursor salts) dissolved in 5 ml OAm, 5 ml OA and 5 ml 1-OD, were added and the solution was rapidly heated to 310 °C for 30 – 40 minutes. The reduction of the metal precursor salts was induced by both the reduction temperature and the surfactants. The black products were isolated and purified by the addition of excess ethanol to precipitate the particles. The separation-precipitation process was performed three times to eliminate any unbound surfactants on the surfaces of the nanoparticles, the black product dried and finally re-suspended in chloroform.

3.2 Nanoparticle Characterization Techniques

3.2.1 Scanning Transmission Electron Microscopy (STEM)

Specimens for scanning transmission electron microscopy (STEM) investigations were prepared by applying one-drop of a colloidal solution onto standard carbon-supported films on copper grids. These were air dried under ambient conditions. Specimens were analysed using TEM, HRTEM and STEM on a JEOL ARM200F probe-corrected instrument, operating at 200 keV. The chemical compositions of individual nanoparticles were determined using energy dispersive X-ray spectroscopy (EDS) in STEM mode. Spectrum imaging was used in which an EDS spectrum is obtained at each pixel in the STEM Image, to produce a 3D dataset. Rapid acquisition was used (5s per frame) integrated over at least 100 frames. Image drift correction was applied after each frame. Scanning TEM (STEM) imaging used bright field, high angle annular dark field (HAADF) and secondary electron (SE) mode.

3.2.2 XRD Characterization

The black powders of the as-synthesised and unsupported nanoparticles were deposited onto a silicon (Si) wafer support and characterized by powder XRD on an X'Pert Pro multipurpose diffractometer (MPD), using Cu Kα radiation (λ = 1.54056 Å). The diffraction patterns were recorded at a scan rate of 0.106º/s and with a step size of 0.0334º.

3.2.3 Electrochemical Measurements

Prior to electrochemical investigations, the as-prepared nanoparticles were dispersed onto carbon support (Vulcan XC-72R) via a colloidal-deposition strategy, by mixing the nanoparticles and chloroform, followed by sonication for 15 – 20 minutes. The resulting homogeneous reaction dispersion was left in a fume hood overnight to evaporate the chloroform. The resultant carbon-supported materials were further washed with acetone 3 – 4 times and dried in an oven at 60 ºC. The metal loading (wt. %) (mass of active metal divided by weight of active metal and carbon support) for each sample was verified using thermogravimetric analysis (Mettler Toledo TGA/sDTA851e).

All experiments were performed in a standard three electrode setup at room temperature in a 0.1 M $HClO_4$ solution using either Argon 99.999% (Afrox), Oxygen 99.998% (Afrox) and CO 99% (Afrox) as specified. A Pt coil was used as the counter electrode. A mercury/mercurous sulphate reference electrode was used and all potential values were reported against the standard hydrogen electrode (SHE). The readout currents were not corrected for the ohmic iR losses. A Biologic SP300 potentiostat was coupled to a RDE710 Rotator (Gamry instrument). Catalyst inks were prepared by mixing 10 mg of the catalyst with 2 ml of Milli-Q water, 0.4 – 0.5 ml isopropanol and 25 µl Nafion® perfluorinated resin solution (5 wt. % in a mixture of lower aliphatic alcohols and water, contains 45% water). The resultant mixture was sonicated for 15 – 20 minutes using an Ultrasonic bath. The resulting dark-brown homogeneous catalyst ink was aged for 10 – 20 minutes. 10 µl of the ink was then pipetted onto a glassy carbon (GC) electrode (Pine Research Instrumentation, 5 mm disk OD) and dried under ambient conditions for 30 – 60 minutes to evaporate the solvents. The remaining thin black uniform film of Nafion-catalyst-Vulcan on the GC served as the working electrode. Before use the GC electrode was polished to a mirror finish on a Microcloth polishing pad (Buehler) using 1 µm and 0.05 µm alumina paste (Buehler). After rinsing, the WE was ultra-sonicated in Milli-Q water for 10 minutes and left to dry.

(a) Cyclic Voltammetry

In an argon (Ar)-purged electrolyte, the potential of the working electrode was cycled between 0.05 V and 1.00 V vs. SHE at a scan rate of 100 mV/s for 100 cycles to electrochemically clean the catalyst surface. The sweep rate was then reduced to 50 mV/s. and the third cycle at that scan rate was used for analysis. The electrochemically active surface area (ECSA) was calculated by integrating the area under the curve for the hydrogen underpotential deposition region (H_{upd}) assuming a monolayer hydrogen charge of 210 µC/cm^2_{Pt}[313-315].

(b) CO stripping Voltammetry

CO gas was bubbled into the electrolyte solution while holding the potential of the working electrode at 0.1 V vs. SHE. The electrolyte was then purged with argon (Ar) to remove the dissolved CO gas while still holding the potential of the WE at 0.1 V vs. SHE. The potential of the WE was then cycled to 1.00 V vs. SHE at 20 mV/s, followed by a CV cycle as described

above at 20 mV/s. The peak area could then be determined using the baseline CV and a normalisation factor of 420 μg/cm$^2_{Pt}$[316]was used to calculate the ECSA.

(c) Linear Sweep Voltammetry

The potential of the WE was swept from 1.0 V to 0.05 V vs. SHE and back at 10 mV/s. ORR polarization curves were recorded at rotation speeds of 400, 900, 1600 and 2500 rpm. The ORR curves obtained in O_2 saturated electrolyte were corrected for the capacitive current associated with Pt_xM_y/C catalysts, by subtracting a CV measured in an argon saturated electrolyte. All the polarization curves reported in this work were acquired from the rotation speed of 1600 rpm and the current densities were also normalized with reference to the calculated ECSA to evaluate the area-specific activities and mass-specific activities.

***It should be noted here that all the carbon-supported electrocatalysts (Pt_xM_y/C) with the 20 wt.%, 40 wt.% and 60 wt.% metal loadings reported in this thesis were benchmarked against the HiSPEC Alfa Aesar, A Johnson Matthey Company commercial electrocatalysts (Pt/C) with 20 wt.%, 40 wt.% and 60 wt.% metal loadings, respectively*.**

***All the durability measurements of the as-synthesized Pt-based nanostructures were evaluated by potential cycling between 0.05 V and 1.1 V at the sweep rate of 100 mV/s for 5000 cycles in an argon (Ar)-purged 0.1 M $HClO_4$ electrolyte solution*.**

CHAPTER 4 RESULTS

This chapter presents results obtained from successfully synthesized nanoparticles; some discussion of these results is included, for each alloy system and reduction method. More general discussion, of the overall results, is deferred to Chapter 5. Scanning transmission electron microscopy (STEM) and X-ray diffraction (XRD) were both used to investigate the structural properties of as-synthesized nanoparticles; where XRD was not carried out, characterisation was by STEM alone. The sizes of the nanostructures were calculated by measuring their diameter, from arbitrarily selected areas of STEM micrographs, using both ImageJ software[317] and an offline DigitalMicrograph (DM) software. The structural characteristics were found to vary, depending on both the alloy system and the reduction method. The following sections thus present results according to alloy system and reduction method. Electrochemical measurements were conducted to measure the oxygen reduction reaction (ORR) functionality of these nanoparticles. For selected nanoparticles, durability was also investigated. All the synthesised nanoparticles exhibited improved catalytic functionality relative to the Pt/C electrocatalysts which are currently in use.

4.1 Co-reduction by Thermolysis: PtNi Binary Nanoparticles

4.1.1 Scanning Transmission Electron Microscopy (STEM) Analysis

This reduction route yielded nanoparticles with morphologies which varied according to the third surfactant type (OLEA, TOA or DOA), which are noted as suffixes to PtNi. Figure 4.1 shows bright field STEM micrographs (first column) with corresponding HAADF micrographs (second column), HR-STEM micrographs (third column) and the corresponding fast Fourier-transform (FFT) pattern (fourth column) of (**a**) PtNi-OLEA, (**b**) PtNi-TOA and (**c**) PtNi-DOA. All nanoparticles are seen to exhibit good dispersion and no agglomeration.

Figure 4.1(**a**) shows that PtNi-OLEA has a high degree of crystallinity with lattice fringes visible, and well-defined morphologies which are cuboidal and triangular with internal rings. When substituting OLEA with TOA (Fig. 4.1 (**b**)), nanoparticles exhibit cuboidal (~70%) and elongated polyhedral with single twin region (~30%) morphologies with clear rings. Figure 4.1(**c**) shows that PtNi-DOA has dominant morphologies which are cuboidal (hexagonal in projection) (~60%) and elongated polyhedral (~40%). The equiaxed PtNi-OLEA nanoparticles

are seen in Figure 4.1(**a**) to be smaller than the Pt-DOA and Pt-TOA nanoparticles; measurements are shown in Figure 4.2.

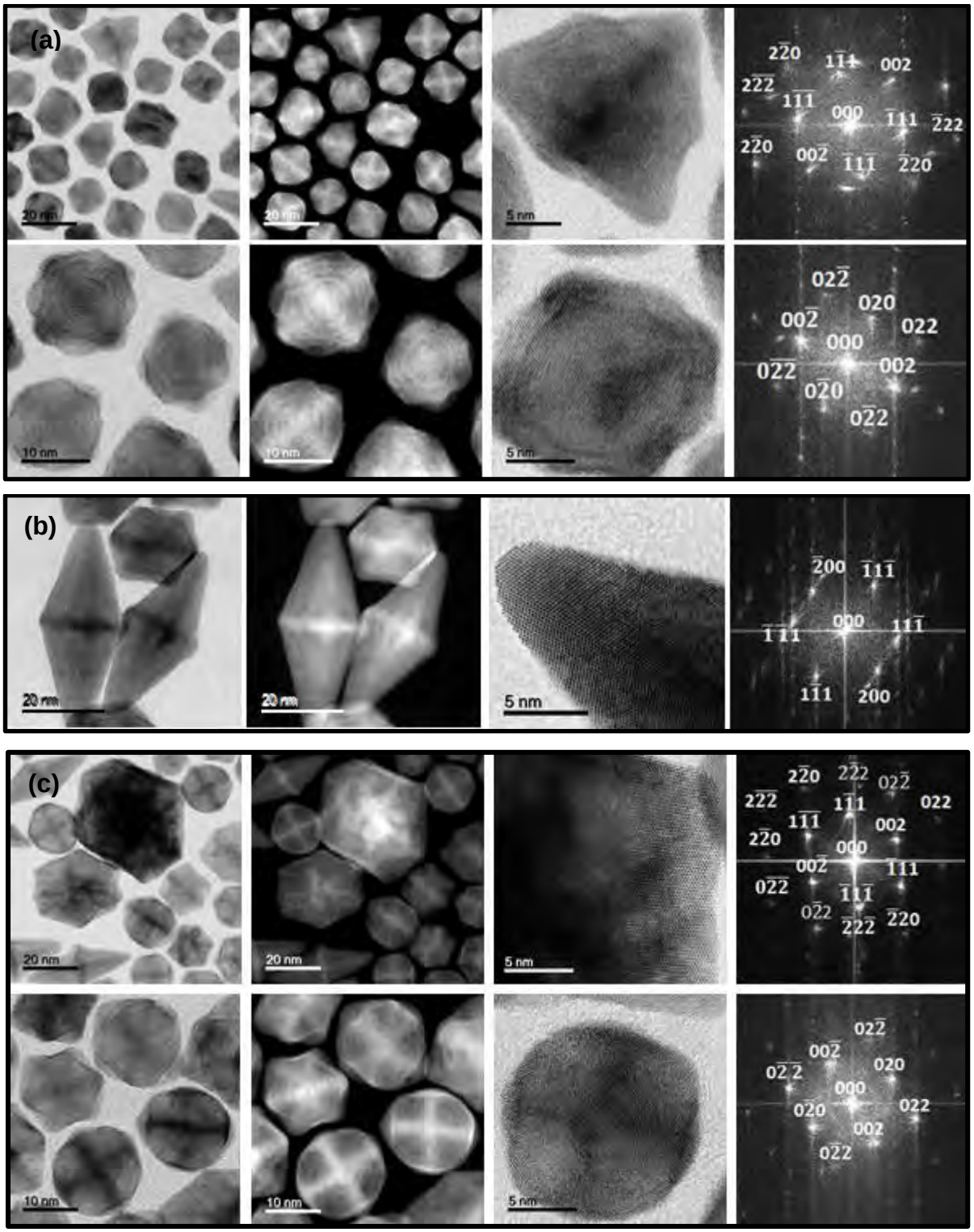

Figure 4.1*: Bright field (BF) STEM micrographs and the corresponding HAADF micrographs, HR-STEM (BF) images and FFT diffractograms of (**a**) PtNi-OLEA, (**b**) PtNi-TOA and (**c**) PtNi-DOA nanoparticles.

*Images acquired with the expert assistance of Dr David Mitchell, University of Wollongong

Figure 4.2 shows histograms of particle size distributions for the nanoparticles. PtNi-OLEA, which is seen to have regularly-shaped particles, has an average particle size of 17.6 ± 1.9 nm (Fig. 4.2(**a**)). PtNi-TOA and PtNi-DOA have both cuboidal (bounded by {100} and {110} facets) and elongated polyhedral (enclosed by {111} facets) nanoparticles; the average size for these two morphologies is shown separately in Figures 4.2(**b**) and (**c**). The PtNi-TOA and PtNi-DOA nanoparticles accordingly exhibit a larger particle size and a broader particle size distribution than PtNi-OLEA.

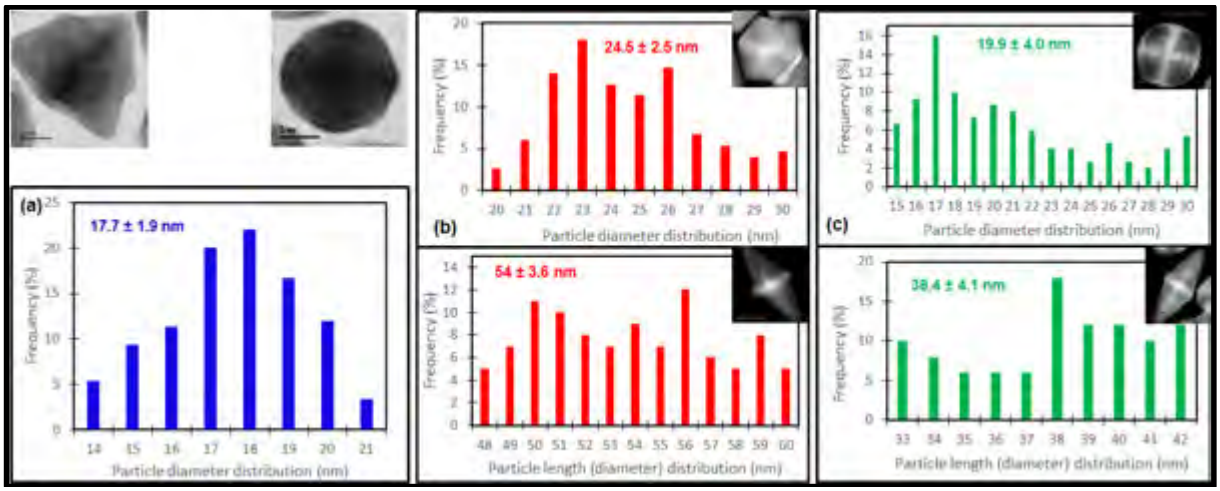

Figure 4.2: Particle size distribution (nm) histograms of (**a**) PtNi-OLEA, (**b**) PtNi-TOA and (**c**) PtNi-DOA alloy nanoparticles.

The elemental distributions within single particles of PtNi-OLEA, PtNi-TOA and PtNi-DOA were determined using high-angle annular dark-field scanning transmission electron microscopy with energy dispersive spectroscopy (HAADF-STEM-EDS). Figures 4.3(**a**)-(**c**) show HAADF-STEM micrographs (first column) and the corresponding X-ray elemental maps for the nanoparticles (second and third columns). All three types of nanoparticles show a (~2-nm) Pt-rich shell with a core slightly rich in Ni, indicating that the final structures are core-shell nanoparticles.

*Images acquired with the expert assistance of Dr David Mitchell, University of Wollongong

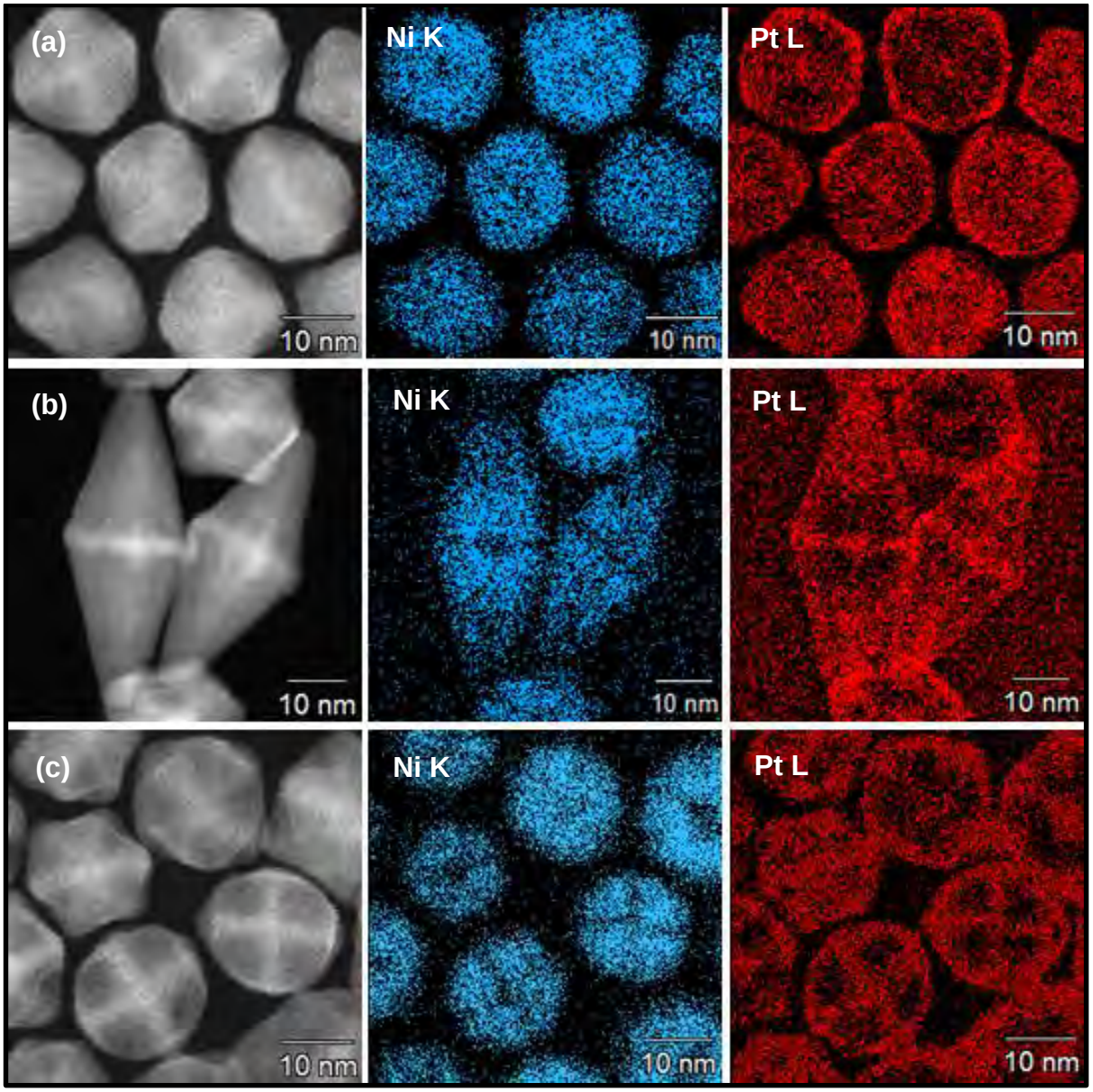

Figure 4.3*: HAADF-STEM-EDS elemental mapping for (**a**) PtNi-OLEA, (**b**) PtNi-TOA and (**c**) PtNi-DOA alloys, revealing elemental distribution within single crystalline particles.

The chemical compositions of the bimetallic nanoparticles were determined using scanning transmission electron microscope-energy dispersive X-ray (STEM-EDS), as shown in Table 4.1. The atomic compositions of the binary nanoparticles show the coexistence of Pt and Ni elements as solid solutions. The STEM-EDS measurements reveal overall average final compositions of $Pt_{68}Ni_{32}$-OLEA, $Pt_{46}Ni_{54}$-TOA and $Pt_{36}Ni_{64}$-DOA.

*Images acquired with the expert assistance of Dr David Mitchell, University of Wollongong

Table 4.1: Elemental compositions of Pt and Ni binary nanoparticles

Alloys	Element Line	Atom %
PtNi-OLEA	Ni K Pt L	32.42 67.58
PtNi-TOA	Ni K Pt L	54.15 45.85
PtNi-DOA	Ni K Pt L	63.81 36.19

4.1.2 X-ray Diffraction (XRD) Analysis

X-ray diffraction (XRD) spectra for the PtNi binary nanoparticles are shown in Figure 4.4. Four 2θ diffraction peaks were detected for all nanoparticles and were indexed to (111), (200), (220) and (311) planes. These patterns are characteristic of the face-centred cubic (fcc) phase; a slight shift of the peak positions toward higher angles, relative to the position of the diffraction peak of the pure fcc-Pt (not shown), shows that lattice spacings (*d*) were reduced due to partial replacement of Pt by Ni, which is a smaller atom. This is consistent with Vegard's law[318, 319] which predicts a peak position shift from a low angle for a Pt-enriched alloy to a higher angle for Ni-enriched alloys.

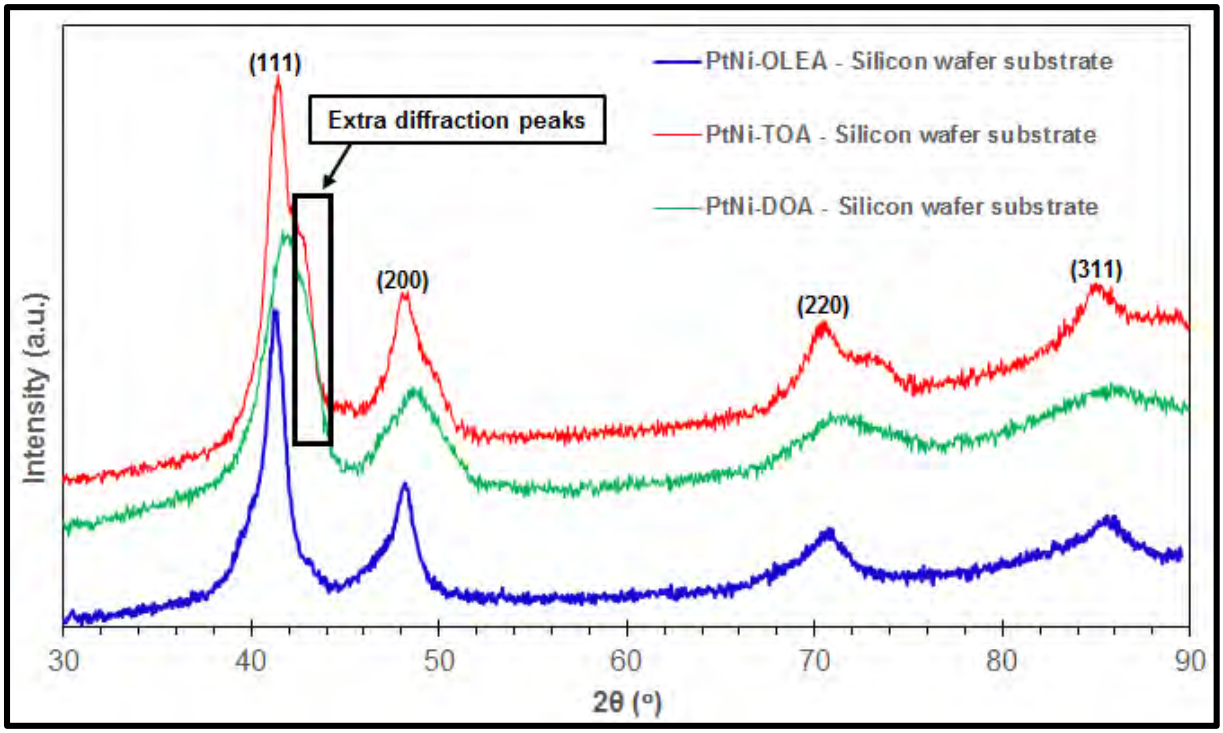

Figure 4.4: XRD diffractograms of PtNi-OLEA, PtNi-TOA and PtNi-DOA alloy nanoparticles.

Table 4.2 shows calculations of lattice constants based on the XRD results, together with published values for lattice constant; values for composition calculated (from Vegard's Law using XRD results), and composition values from STEM-EDS results. Examination of the XRD spectra in Figure 4.4 shows some splitting of the (111) diffraction peak for PtNi-TOA and PtNi-DOA, suggesting the coexistence of another fcc phase. For these two binary nanoparticles, two values are calculated for lattice constant and for composition, i.e. from each of the peaks. The calculated lattice constants of these three alloys were in reasonable agreement with the literature values[320] for PtNi, as shown in Table 4.2; the additional values for PtNi-TOA and PtNi-DOA are consistent with the lattice constant for $PtNi_3$. The compositions calculated using Vegard's law were in good agreement with the composition measured using STEM-EDS, which indicates the formation of Ni-Pt core-shell nanoparticles.

Table 4.2: PtNi binary nanoparticles: calculated lattice constants from XRD, and from the scientific literature; calculated composition from XRD and Vegard's law and measured composition from STEM-EDS analysis.

Nanoalloys	2θ Diffraction peaks (°)	hkl	d-spacing (nm)	Lattice constants (nm)	Literature values (Lattice constants) (nm)[318]	Vegard's equation (composition)	STEM-EDS Atomic composition
PtNi-OLEA	41.708	(111)	0.216	0.37476	PtNi: 0.3864	$Pt_{56}Ni_{44}$	$Pt_{60}Ni_{40}$
PtNi-TOA	41.404 42.595	(111) (111)	0.218 0.212	0.3774 0.3673	PtNi: 0.3864 $PtNi_3$: 0.3663	$Pt_{61}Ni_{39}$ $Pt_{37}Ni_{63}$	$Pt_{50}Ni_{50}$ $Pt_{39}Ni_{61}$
PtNi-DOA	41.823 42.723	(111) (111)	0.216 0.212	0.3738 0.3663	PtNi: 0.3864 $PtNi_3$: 0.3663	$Pt_{51}Ni_{49}$ $Pt_{39}Ni_{61}$	$Pt_{51}Ni_{49}$ $Pt_{36}Ni_{64}$

Nanoparticle sizes were also estimated from XRD data using the Debye-Scherrer equation[4]. The values obtained for the PtNi-OLEA (20.6 nm), PtNi-TOA (27.5 nm and 56.3 nm) and PtNi-DOA (25 nm and 42.8 nm) alloy nanoparticles, were slightly higher than STEM values (Fig. 4.2). This probably arises from the volume-based average crystallite sizes of diffracting crystals derived from XRD, which is expected to be larger rather than the particle size.

4.1.3 Electrochemical Surface Area and ORR Activity

To produce a usable catalyst for electrochemical testing, the as-prepared Pt-based nanoparticles were dispersed on a highly conductive and high surface area carbon support (Vulcan XC-72R) via a colloidal-deposition method. Bright field STEM images of carbon-supported nanoparticles are shown in Figures 4.5(**a**)-(**c**), indicating their good dispersity with no apparent change in microstructure.

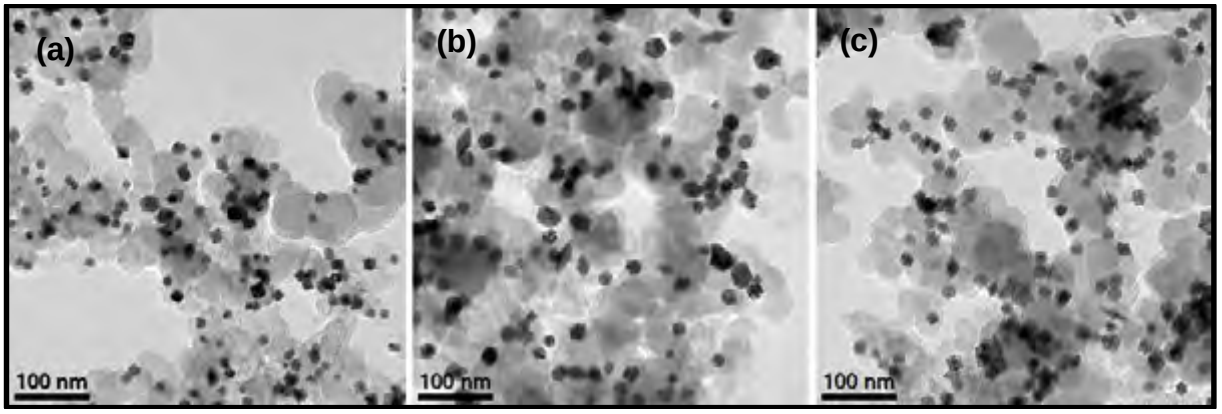

Figure 4.5: STEM micrographs of (**a**) PtNi-OLEA, (**b**) PtNi-TOA and (**c**) PtNi-DOA nanoparticles supported on high surface area carbon (Vulcan XC-72R).

Figure 4.6 shows results from electrochemical testing of PtNi nanoparticles. Figure 4.6(**a**) shows cyclic voltammograms, which exhibited both hydrogen desorption/adsorption peaks[2, 87] (~0.05 – 0.35 V) and oxide formation/reduction peaks[2, 87] (~0.7 – 1.0 V). The hydrogen desorption/adsorption peak current (H_{udp}) and oxide formation/reduction peak current of these nanoparticles, varied in the following sequence: PtNi-OLEA/C > PtNi-DOA/C > commercial Pt/C >> PtNi-TOA/C. The oxide regimes suggest the formation of Ni/Ni oxides and their subsequent gradual dissolution/dealloying with the cleaning of the nanostructure surface and hence formation of a Pt-enriched surface, consistent with other reports[321]. The ECSAs scaled as follows, relative to the commercial catalyst: Pt/C (162.6 $m^2g_{Pt}^{-1}$) > PtNi-OLEA/C (91.4 $m^2g_{Pt}^{-1}$) > PtNi-DOA/C (84.1 $m^2g_{Pt}^{-1}$) >> PtNi-TOA/C (54.7 $m^2g_{Pt}^{-1}$).

The $ECSA_{Hupd}$ was confirmed by conducting CO oxidative stripping ($ECSA_{CO}$) measurements, as shown in Fig 4.6 (b), resulting in the evolution of sharp and well-defined transient positive current CO peaks. All the CO-stripping oxidation peak positions for the three nanoparticles are located between +0.55 and +0.75 V. The substantial presence of Ni/Ni oxide on the Pt alloy surface resulted in the CO stripping peaks shifting to a more negative potential than the commercial Pt/C electrocatalyst[321] which exhibits two oxidative peaks at more positive potentials between +0.6 and +0.85 V (Fig. 4.6(**b**)). This indicates improved CO tolerance for the alloy materials. The $ECSA_{CO}$ investigated scale as follows: commercial Pt/C (175.6 $m^2g_{Pt}^{-1}$) > PtNi-OLEA/C (108 $m^2g_{Pt}^{-1}$) > PtNi-DOA/C (104.2 $m^2g_{Pt}^{-1}$) >> PtNi-TOA/C (62 $m^2g_{Pt}^{-1}$). This is consistent with the $ECSA_{Hupd}$, as shown in Fig. 4.4 (in section 4.1.4, Durability Measurements). The slightly higher $ECSA_{CO}$ values compared to $ECSA_{Hupd}$ are attributed to the contribution of the capacity of the carbon carrier substrate for the high surface area catalysts. The ratios determined between $ECSA_{CO}$ and $ECSA_{Hupd}$ ($ECSA_{CO}/ECSA_{Hupd}$) for all

the nanoparticles were approximately 1.1, indicative of negligible differences in terms of both H_{ads} and CO_{ads} surface coverage. The inherent anisotropic nature and the corresponding very high ECSAs of these three alloy nanoparticles provide more accessibility for reacting molecules to the surface structure toward ORR.

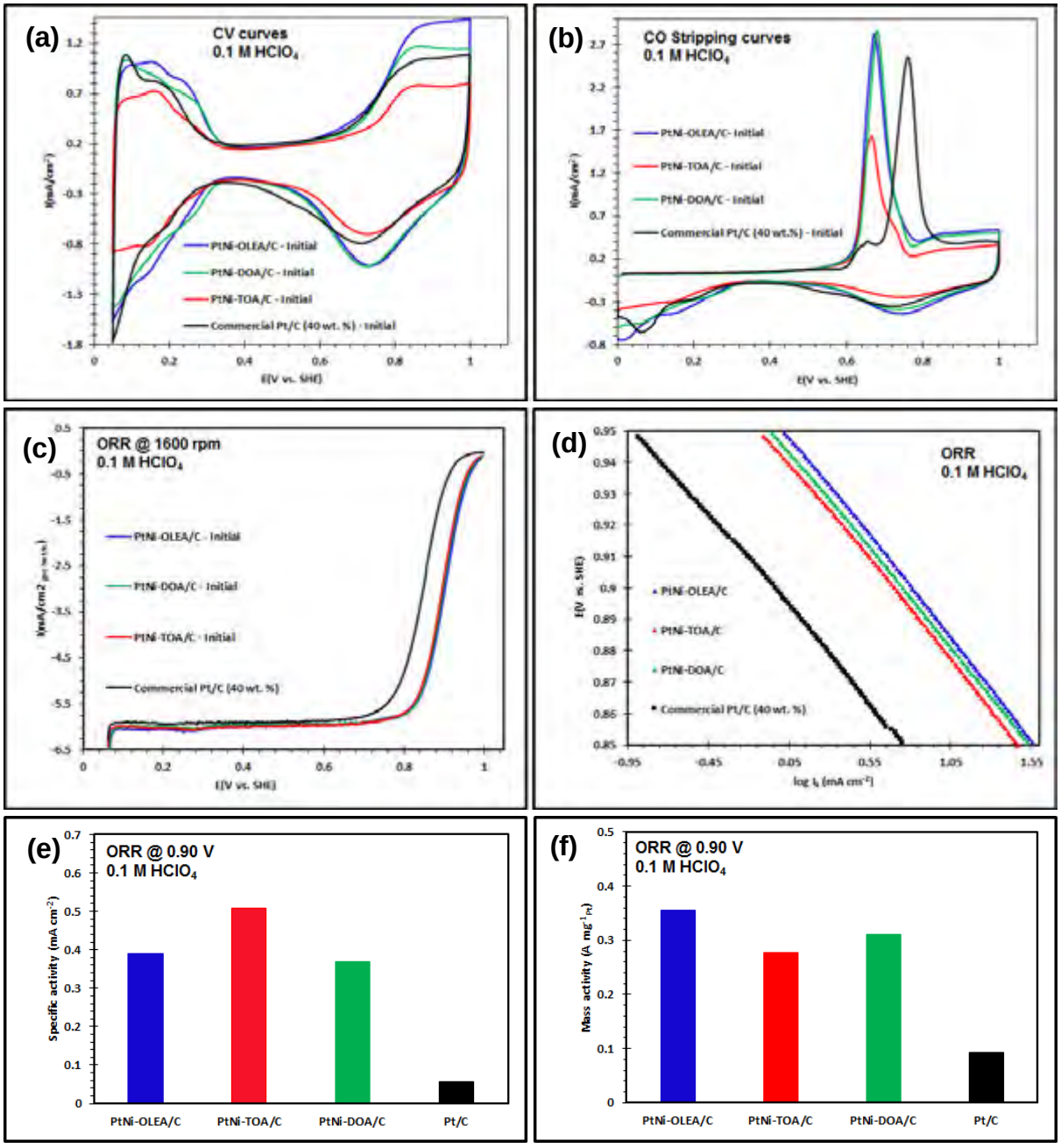

Figure 4.6: (**a**) Cyclic voltammograms of binary Pt-based alloys PtNi-OLEA/C (blue), PtNi-TOA/C (red), PtNi-DOA/C (green) and Pt/C (black)), (**b**) CO-stripping voltammograms, (**c**) ORR polarization curves, (**d**) the corresponding Tafel plots, (**e**) intrinsic area-specific activities and (**f**) mass-specific activities at +0.9 V after 100 cycles.

All the ORR polarization curves (Fig. 4.6(**c**)) reached the diffusion limited-current at ~ 6.0 mA cm^{-2}, and these experimental values are consistent with the reported theoretical value (5.7 - 6.02 mA cm^{-2}) [87, 309-311]. Tafel plots (Fig. 4.6(**d**)) obtained from the potentials in the range of +0.85 – 0.95 V, exhibit the following activity trend: PtNi-OLEA/C > PtNi-DOA/C > PtNi-TOA/C >> commercial Pt/C. Consequently, these plots indicate that PtNi-OLEA/C displays the most positive onset potential of all of the electrocatalysts, showing the superior catalytic performance of this binary alloy.

The Pt area-specific activities and mass-specific activities of these nanoparticles were benchmarked against the commercial Pt/C electrocatalysts (Figs. 4.6(**e**)-(**f**)). The Pt mass-specific activities for effective Pt utilisation at +0.9 V of PtNi-OLEA/C, PtNi-TOA/C and PtNi-DOA/C exhibit factors of ~4, 3 and 3.3- ORR enhancement, respectively, when compared with the commercial Pt/C electrocatalysts. In conjunction with the mass-specific activity evaluations, the area-specific activities to investigate the absolute value of the electrocatalyst intrinsic area-specific activity of PtNi-OLEA/C, PtNi-TOA/C and PtNi-DOA/C display ~7, 9 and 7-fold activity enhancement, respectively, compared with that of the commercial Pt/C catalyst.

4.1.4 Durability Measurements

The durability of a catalyst material is critically important for its functionality as a commercial catalyst. Characterisation was accordingly repeated after 5000 potential cycles. Figure 4.7 shows STEM imaging of (**a**) PtNi-OLEA/C, (**b**) PtNi-TOA/C and (**c**) PtNi-DOA/C nanoparticles which reveals the formation of voids, coalescence of the particles due to surface migration on the carbon support, deformed morphologies (crystal facets), possible particle surface oxidation and carbon corrosion. Elemental mapping shows the presence of both Ni and Pt. The STEM-EDS composition values shown in Table 4.3, however, reveal a decrease in Ni/Ni oxide content.

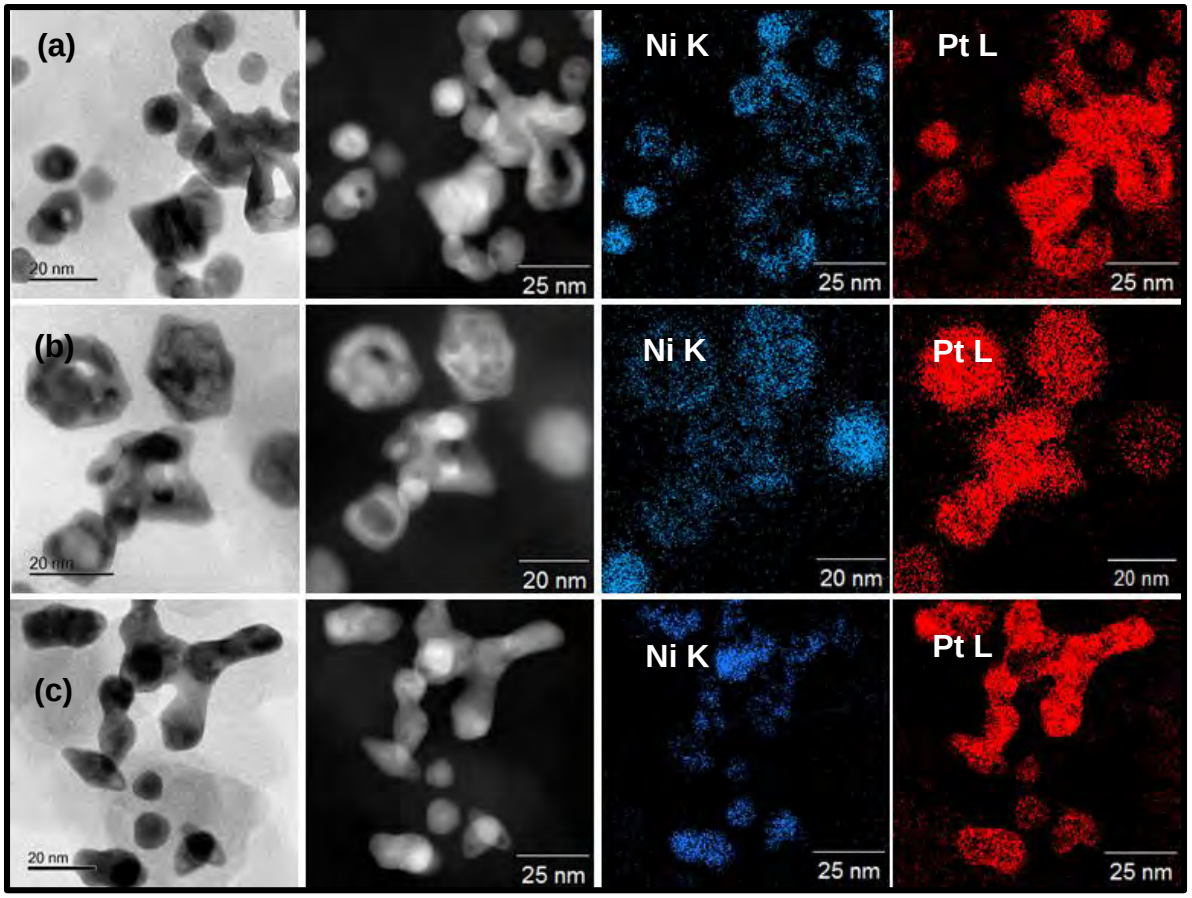

Figure 4.7*: BF (first column), HAADF (second column) and STEM-EDS elemental mapping results (third and fourth columns) for (**a**) PtNi-OLEA/C, (**b**) PtNi-TOA/C and (**c**) PtNi-DOA/C alloys, post 5000 cycles, showing elemental distribution within single crystalline particles of solid solutions.

Table 4.3: Elemental compositions of Pt and Ni binary nanoparticles after 5000 potential cycles.

Alloys	Element Line	Atom %
PtNi-OLEA	Ni K Pt L	15.45 84.55
PtNi-TOA	Ni K Pt L	15.22 84.78
PtNi-DOA	Ni K Pt L	11.31 88.69

Electrochemical testing results in Figure 4.8 show that two current peaks emerged with continual cycling to 5000 cycles. These can be ascribed to {100} and {110} surface sites (labelled in Fig. 4.8(**a**)), where hydrogen adsorption (H_{ads}) occurs. These surface sites are characteristic of pure polycrystalline Pt with the {110} surface sites binding the hydrogen more strongly than the {100} surface sites[293]. This indicates progressive leaching of Ni from the PtNi alloys, confirming the results obtained through elemental mapping.

*Images acquired with the expert assistance of Dr David Mitchell, University of Wollongong

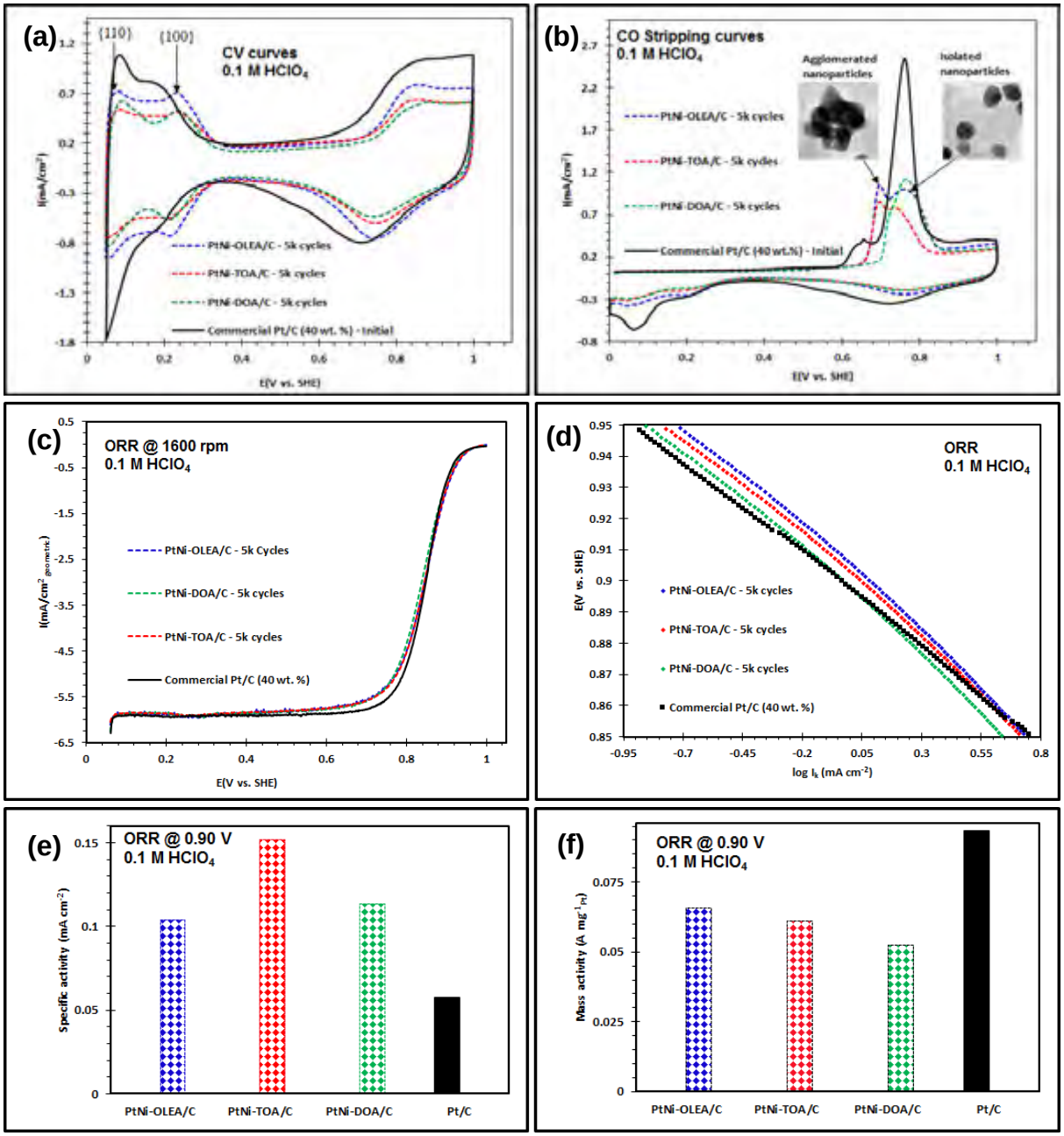

Figure 4.8: (**a**) Cyclic voltammograms of binary Pt-based alloys PtNi-OLEA/C (blue), PtNi-TOA/C (red), PtNi-DOA/C (green) and commercial Pt/C (black), (**b**) CO-stripping voltammograms, (**c**) ORR polarization curves, (**d**) the corresponding Tafel plots, (**e**) intrinsic area-specific activities and (**f**) mass-specific activities at +0.9 V after 5000 cycles, respectively. Durability measurements for the commercial Pt/C electrocatalysts were not conducted.

The $ECSA_{Hupd}$ reduction with prolonged potential cycling was confirmed by conducting CO oxidative stripping ($ECSA_{CO}$) measurements (Fig. 4.8(**b**)), dashed lines). These show a decline in CO current peaks and a positive shift from lower to higher potentials due to Ni/Ni oxide disintegration leading to less CO tolerance of the nanoparticles, and the appearance of double peaks with increasing potential cycling. The latter could be due to particle agglomeration and the existence of defects (more negative peak), segregated particles (more positive peak) [316, 322]

(labels and inserts in Fig. 4.8(**b**)), preferential/selective binding onto distinct facets[323], or the nature of the surface sites or particle size distribution[87, 316].

After 5000 potential cycles, all the three binary alloys showed significant reductions in the ORR activity, with the polarization curves shifting from higher (positive) to lower (negative) potentials (Fig. 4.8(**c**), dashed lines). In terms of area-specific activity the binary nanoparticle catalysts presented here still show at least a doubling in performance, while in terms of mass-specific activity all catalysts now show activities similar to pure Pt. The latter results again suggest the loss of the Ni from the alloys (Figs. 4.8(**e**)-(**f**)).

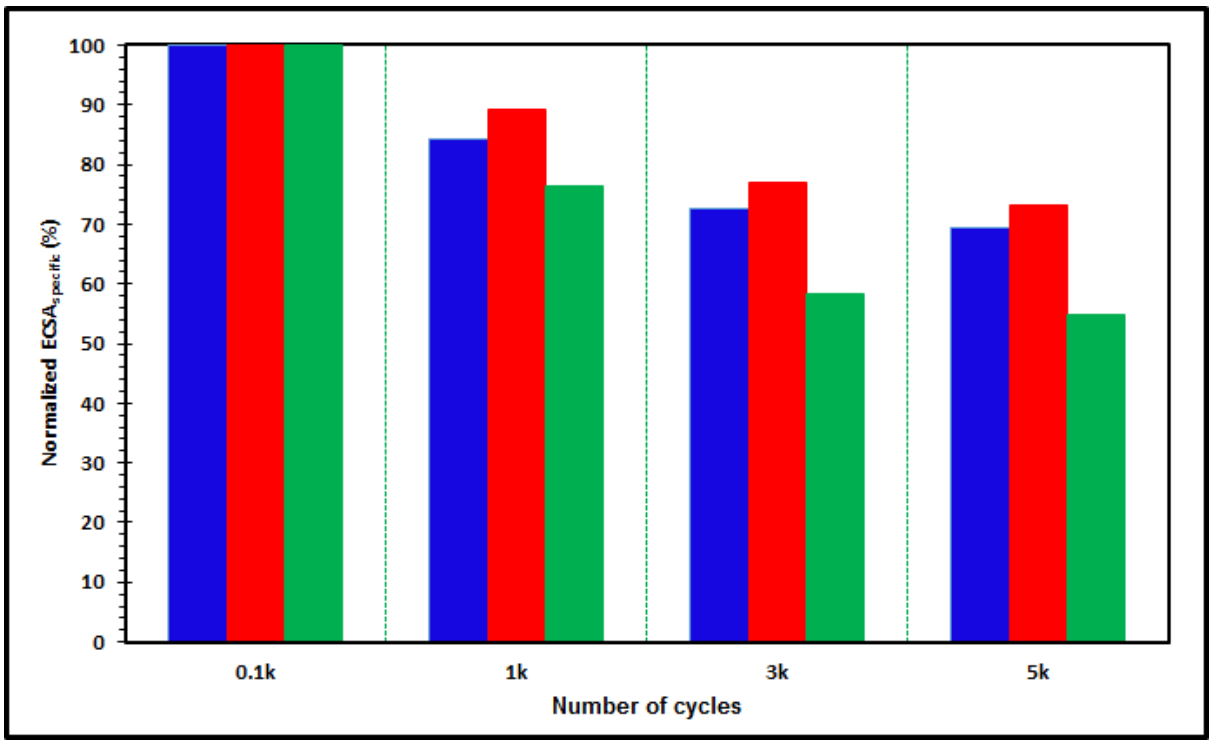

Figure 4.9: ECSA decay as a function of the continual potential cycling (up to 5000 cycles) of PtNi-OLEA/C (blue), PtNi-TOA/C (red) and PtNi-DOA/C (green) nanoparticles.

The $ECSA_{Hupd}$ after 5000 cycles (as a percentage of the initial value) decreased as follows: PtNi-DOA/C (45%) > PtNi-OLEA/C (31%) > PtNi-TOA/C (27%), as shown in Figure 4.9. The $ECSA_{Hupd}$ decay could arise from Ni/Ni oxide dissolution; particle surface migration on carbon support followed by coalescence; metal alloy oxide formation as a result of potential cycling; or morphological deformations[293, 324, 325].

Table 4.4: Comparisons of the methods, morphology, particle size diameter, $ECSA_{Hupd}$, $ECSA_{CO}$, $ECSA_{CO}/ECSA_{Hupd}$, mass-specific and area-specific activities at 0.9 V of PtNi binary nanoparticles.

Nanoalloy	Nanoalloy morphologies	Particle diameter (nm)	ECSA (m^2/g_{Pt}) (CV)	ECSA (m^2/g_{Pt}) loss (%)	ECSA (m^2/g_{Pt}) (CO stripping)	ECSA (m^2/g_{Pt}) (CO stripping) loss (%)	Mass activity (A/mg_{Pt})	Mass activity loss (%)	Specific activity (mA/cm^2_{Pt})	Specific activity loss (%)
PtNi-OLEA/C (40 wt.%)	Cubic and Triangular	17.6 ± 1.9	0.1K Cycles: 91.4	31	0.1K Cycles: 108	35	0.36	82	0.39	73
			5K Cycles: 47.5		5K Cycles: 52.7		0.07		0.104	
PtNi-TOA/C (40 wt.%)	cuboidal	24.5 ± 2.5	0.1K Cycles: 54.7	27	0.1K Cycles: 62	27	0.28	78	0.51	70
	Elongated polyhedral	53.9 ± 3.6	5K Cycles: 30.1		5K Cycles: 33.8		0.06		0.152	
PtNi-DOA/C (40 wt.%)	cuboidal	19.9 ± 4.0	0.1K Cycles: 84.1	45	0.1K Cycles: 104.2	48	0.31	83	0.37	69
	Elongated polyhedral	38.4 ± 4.1	5K Cycles: 34.5		5K Cycles: 40.4		0.05		0.113	
Commercial Pt/C (40 wt.%)	Spherical	4.8 ± 3.5	0.1K Cycles: 162.6	-	0.1K Cycles: 175.6	-	0.093	-	0.057	-

These shape-orientated, multi-faceted PtNi core-shell nanoparticles, required for enhancing the ORR functionality, were successfully synthesized via a co-reduction by thermolysis approach and by varying the surfactants while keeping the other reduction parameters unchanged. These nanoparticles displayed excellent functionality compared with the commercially available Pt/C electrocatalysts. The preliminary durability measurements showed activity decay comparable to the initial commercial Pt/C electrocatalyst measurements, suggesting Ni/Ni oxide dissolution, shape deformation and particle coalescence. This section accordingly defines a novel synthetic strategy for shape-dependent Ni-Pt core-shell nanoparticles for high performance ORR with considerable scope for further improvements to performance and durability.

4.2 Sequential Reduction by Thermolysis: PtNi Binary Nanoparticles

4.2.1 Scanning Transmission Electron Microscopy (STEM) Analysis

This high-temperature sequential thermolysis approach yielded nanoparticles with morphologies which varied according to the third surfactant type (OLEA, TOA or DOA), which are noted as suffixes to PtNi. Figure 4.10 shows PtNi nanoparticles: secondary electron (SE) images (first column), HAADF micrographs (second column) and the corresponding bright field images (third column), HR-HAADF (fourth column) and the corresponding BF-STEM micrographs (fifth column). Nanoparticle morphology varied as follows: PtNi-OLEA (Fig. 4.10 (a)) shows porous irregular and cubic shapes; PtNi-TOA (Fig. 4.10 (b)) shows mostly

irregular shapes; and PtNi-DOA (Fig. 4.10 (c)) shows cubo-octahedral and elongated polyhedral shapes. Inserts in the HR-HAADF-STEM images are fast Fourier-transform (FFT) patterns, indicating that the nanoparticles are single crystals. In all cases, they are highly monodisperse.

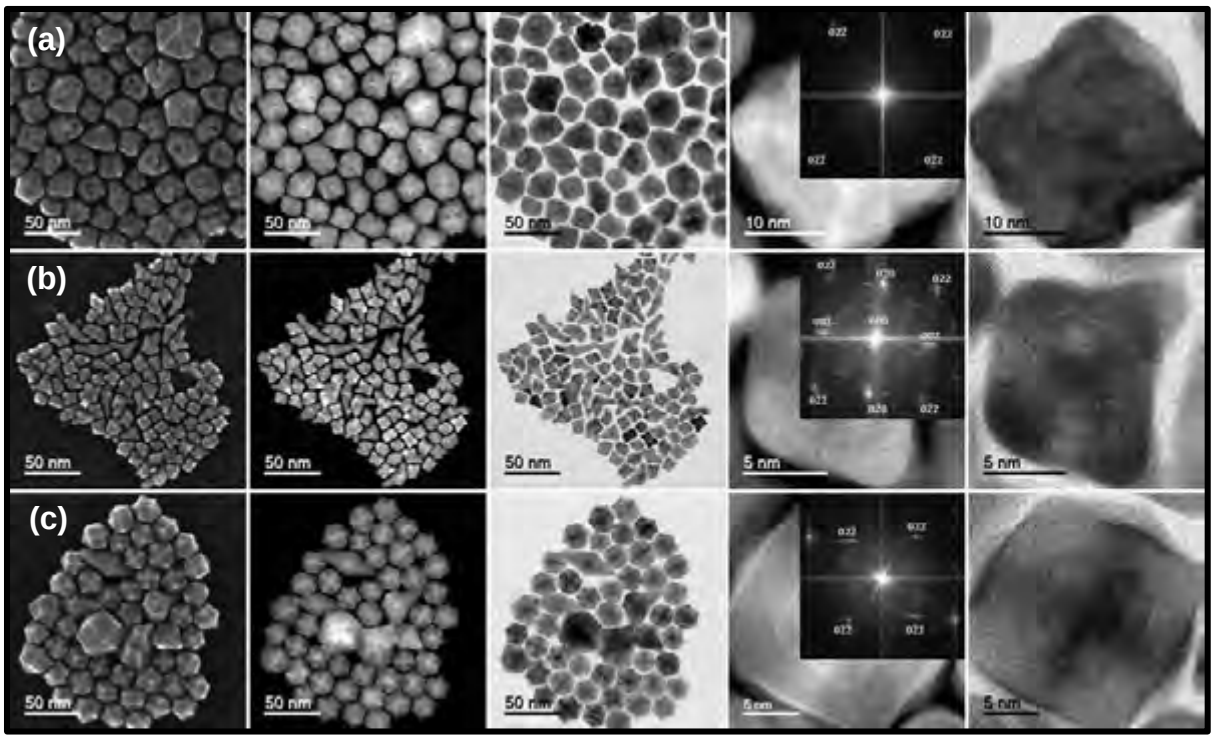

Figure 4.10*: Left to right: Secondary electron (surface topography), HAADF and BF STEM micrographs, high resolution HAADF and the corresponding HR-BF STEM images of binary (**a**) PtNi-OLEA, (**b**) PtNi-TOA and (**c**) PtNi-DOA nanoparticles. Insets are FFTs of the HR-HAADF-STEM micrographs.

Figures 4.11(**a**)-(**c**) show article size distribution histograms of the PtNi nanoparticles. On the basis of the TEM images, the average particle diameters of the nanoparticles were determined as 32.9 ± 2.8 nm, 16.7 ± 1.8 nm and 26.6 ± 2.1 nm for binary (**a**) PtNi-OLEA, (**b**) PtNi-TOA and (**c**) PtNi-DOA nanoparticles, respectively.

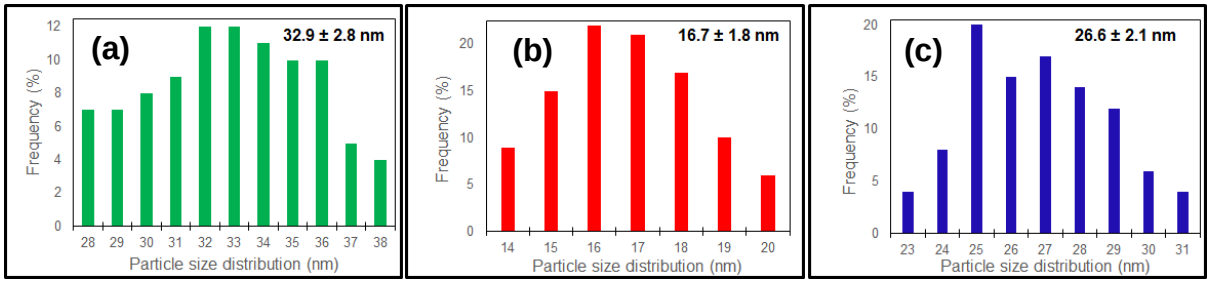

Figure 4.11: Particle size distribution histograms of (**a**) PtNi-OLEA, (**b**) PtNi-TOA and (**c**) PtNi-DOA alloy nanoparticles.

The elemental distributions of single crystal particles of PtNi-OLEA, PtNi-TOA and PtNi-DOA were determined using HAADF-STEM-EDS. Figures 4.11(**a**)-(**c**) show HAADF-STEM micrographs (first column) and the corresponding X-ray elemental maps for the nanoparticles (second and third columns). Elemental mapping of the three nanoparticles shows a Ni-rich core and a (~2-nm) Pt-rich shell, suggesting that the final structures are core-shell nanoparticles. EDS analysis reveals an average overall composition of $Pt_{61}Ni_{39}$-OLEA, $Pt_{96}Ni_{4}$-TOA and $Pt_{30}Ni_{70}$-DOA nanoparticles, as shown in Table 4.5.

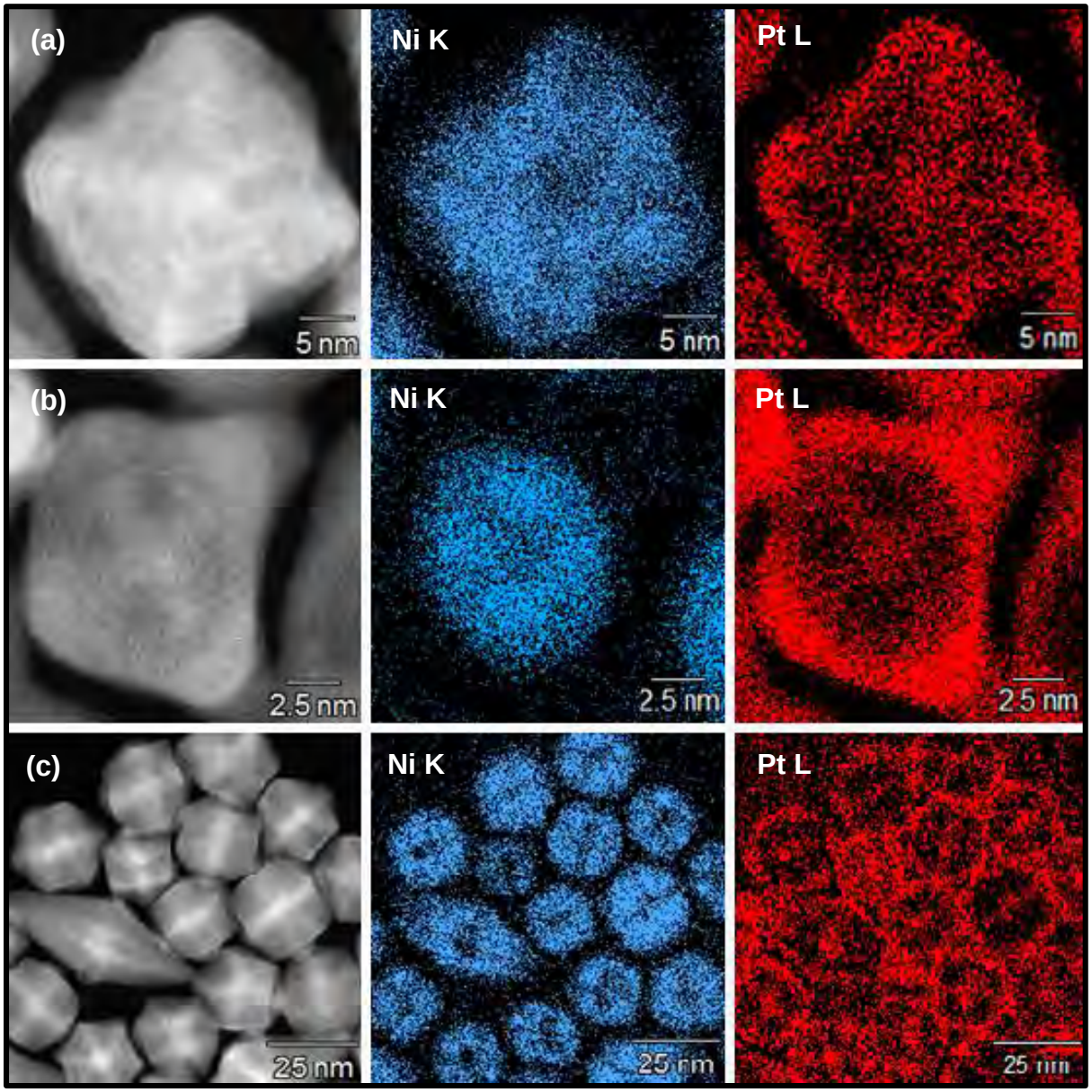

Figure 4.11*: HAADF-STEM-EDS elemental mapping for (**a**) PtNi-OLEA, (**b**) PtNi-TOA and (**c**) PtNi-DOA nanoparticles, revealing elemental distribution within single crystalline particles.

*Images acquired with the expert assistance of Dr David Mitchell, University of Wollongong

Table 4.5: Elemental compositions of (**a**) PtNi-OLEA, (**b**) PtNi-TOA and (**c**) PtNi-DOA alloy nanoparticles.

Alloys	Element Line	Atom %
PtNi-OLEA	Ni K Pt L	38.84 61.16
PtNi-TOA	Ni K Pt L	4.39 95.61
PtNi-DOA	Ni K Pt L	70.37 29.63

4.2.2 Electrochemical Surface Area and ORR Activity

The as-prepared nanoparticles were dispersed on Vulcan XC-72R. Bright field STEM images of carbon-supported nanoparticles are displayed in Figures 4.12(**a**)-(**c**), indicating their good dispersity with no apparent change in microstructure.

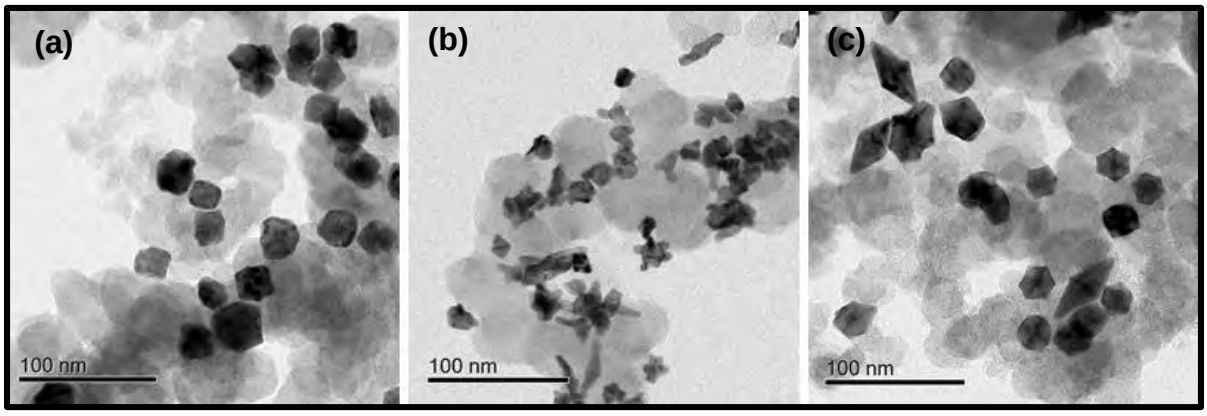

Figure 4.12: STEM images of (**a**) PtNi-OLEA, (**b**) PtNi-TOA and (**c**) PtNi-DOA nanoparticles supported on high surface area carbon (Vulcan XC-72R).

Electrochemical testing results are shown in Figures 4.13(**a**)-(**f**). The $ECSA_{Hupd}$ scaled as follows: PtNi-DOA/C (104.3 $m^2g_{Pt}^{-1}$) > PtNi-TOA/C (87.5 $m^2g_{Pt}^{-1}$) > PtNi-OLEA/C (73.4 $m^2g_{Pt}^{-1}$) >> commercial Pt/C (71 $m^2g_{Pt}^{-1}$). The $ECSA_{CO}$ was determined as follows: commercial Pt/C (198.0 $m^2g_{Pt}^{-1}$) > PtNi-DOA/C (117.6 $m^2g_{Pt}^{-1}$) > PtNi-TOA/C (110.0 $m^2g_{Pt}^{-1}$) >> PtNi-OLEA/C (89.5 $m^2g_{Pt}^{-1}$) as shown in Table 4.6. The high $ECSA_{Hupd}$ values are a result of: contributions from the deformed and porous nature of PtNi-OLEA; mostly dominant irregular and elongated shapes with sharp edges/corners of PtNi-TOA; and cubo-octahedral and elongated polyhedral with sharp edges of PtNi-DOA nanoparticles.

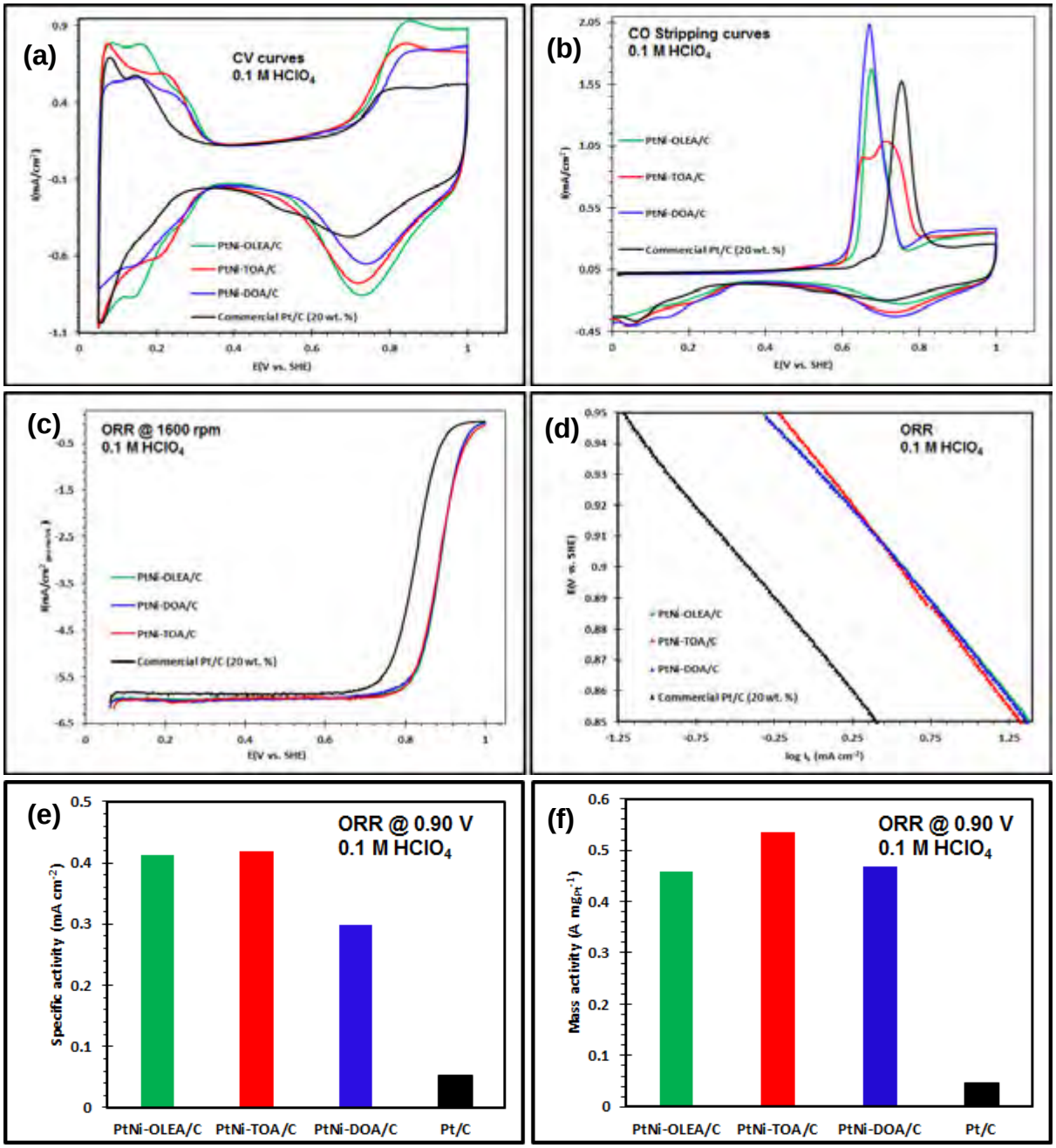

Figure 4.13: (**a**) Cyclic voltammograms of binary Pt-based alloys (PtNi-OLEA/C (green), PtNi-TOA/C (red), PtNi-DOA/C (blue) and Pt/C (black)), (**b**) CO-stripping voltammetry curves, (**c**) ORR polarization curves, (**d**) the corresponding Tafel plots, (**e**) intrinsic area-specific activities and (**f**) mass-specific activities at +0.9 V.

Carbon monoxide (CO) electro-oxidation was also used to investigate the ECSA of Pt alloy nanoparticle surfaces, as shown in Figure 4.13(**b**), to detect the presence of particle agglomerates or isolated nanoparticles[316, 322]. All the alloys show a more negative potential shift relative to commercial Pt/C, supporting the possible dominance of Ni in the Pt-alloy surface, and rendering these nanoparticles more CO tolerant. The single CO oxidation peaks of PtNi-OLEA/C and PtNi-DOA/C indicate that the particles are homogeneously dispersed on

carbon support with no traces of agglomeration, while the double current peak for the PtNi-TOA suggests the possible co-existence of segregated and agglomerated particles. This agrees well with the observations from the STEM micrographs (Fig. 4.12(**b**)).

Polarization curves were obtained from the three alloy nanoparticles and the commercial Pt/C electrocatalysts, as shown in Figure 4.13(**c**). All the ORR polarization curves reached their diffusion limited-current at ~ 6.0 mA cm^{-2}[87, 309-311], suggesting complete mass transfer of oxygen species to the working electrode surface. Figure 4.13(**d**) shows that the Tafel plots obtained from the potentials in the range of 0.85 – 0.95 V, exhibit different functionalities with all the alloys >> commercial Pt/C electrocatalysts. Consequently, these plots indicate that PtNi-OLEA/C displays the more positive onset potential of all the electrocatalysts, showing the remarkable catalytic performance of this binary alloy. The area-specific activities (Fig. 4.13(**e**)) and the mass-specific activity values (Fig. 4.13(**f**)) at + 0.9 V of PtNi-OLEA/C, PtNi-TOA/C and PtNi-DOA/C nanoparticles display ~12, 14 and 13-fold, and ~8, 8 and 6-fold activity enhancement, respectively, compared with the commercial Pt/C electrocatalysts.

Table 4.6: Comparisons of the methods, morphology, particle size diameter, $ECSA_{Hupd}$, $ECSA_{CO}$, $ECSA_{CO}/ECSA_{Hupd}$, mass-specific and area-specific activities at 0.9 V of four nanoparticles.

Nanoalloy	Nanoalloy morphologies	Particle diameter (nm)	ECSA (m^2/g_{Pt}) (CV)	ECSA (m^2/g_{Pt}) (CO stripping)	Mass activity (A/mg_{Pt})	Specific activity (mA/cm^2_{Pt})
PtNi-OLEA/C (20 wt.%)	Porous irregular and cubic	32.9 ± 2.8	0.1K Cycles: 73.4	0.1K Cycles: 89.5	0.46	0.41
PtNi-TOA/C (20 wt.%)	Mostly irregular and cubic	16.7 ± 1.8	0.1K Cycles: 87.5	0.1K Cycles: 110	0.53	0.42
PtNi-DOA/C (20 wt.%)	Hexagonal and elongated polyhedral	26.6 ± 2.1	0.1K Cycles: 104.3	0.1K Cycles: 117.6	0.47	0.3
Commercial Pt/C (20 wt.%)	Spherical	3.3 ± 2.4	0.1K Cycles: 71.0	0.1K Cycles: 198.0	0.037	0.052

This synthetic approach accordingly yielded Pt-based nanoparticles of different surface morphologies; the electrochemical findings indicate that the ORR functionality is strongly regulated by the surface facets of the nanoparticles. The preliminary results from the carbon-supported nanoparticles demonstrate that the as-synthesized nanoparticles are more effective in the ORR than the commercially available Pt/C electrocatalysts.

4.3 Co-reduction by Reductant: PtNi Binary Nanoparticles

4.3.1 Scanning Transmission Electron Microscopy (STEM) Analysis

High-temperature co-reduction by tetrabutylammonium borohydride (TBAB), yielded nanoparticles with morphologies that varied according to the third surfactant type (OLEA or TOA), which are noted as suffixes to PtNi.

Both PtNi-OLEA and PtNi-TOA showed some degree of storage instability in organic dispersants such as toluene, hexane and chloroform. As a consequence of this effect, the deflocculating of the colloidal nanoparticles to restore and formulate a stable dispersion was achieved by the addition of OAm, which transformed the agglomerated particles into a homogeneous dispersion. Aging the nanoparticles in OAm for 2 days, followed by the addition of excess chloroform, purification by the addition of ethanol and finally, re-dispersing the particles in chloroform again (by vigorous sonication) improved the dispersion and stability of the nanoparticles. Although OAm serves as both the surfactant and dispersant, it etches the surface of the nanoparticles selectively and creates atypical (high-index) facets.

Figure 4.14 shows PtNi-OLEA (**a**) and PtNi-TOA (**b**) before and after ageing in OAm. The first column shows BF STEM micrographs before ageing; the last two columns show BF STEM and the corresponding HAADF images. SAED patterns, from large numbers of nanoparticles, are inset. The rings observed in SAED patterns correspond to the (111), (200), (220) and (311) face-centred cubic (fcc) planes in Pt-based nanoparticles. In all cases, the nanoparticles are highly monodisperse.

Figure 4.14 shows PtNi-OLEA (**c**) and PtNi-TOA (**d**) imaged using HR-STEM, which demonstrates that the nanoparticles have an excellent degree of crystallinity and the same orientation as the lattice fringes. PtNi-OLEA is seen to be cuboidal with pyramidal type faceting on the main 100 facets; PtNi-TOA exhibits elongated polyhedral and dominant cuboctahedral nanoparticles. The inserts in HR-HAADF micrographs are FFT patterns indicating that the nanoparticles are single crystals.

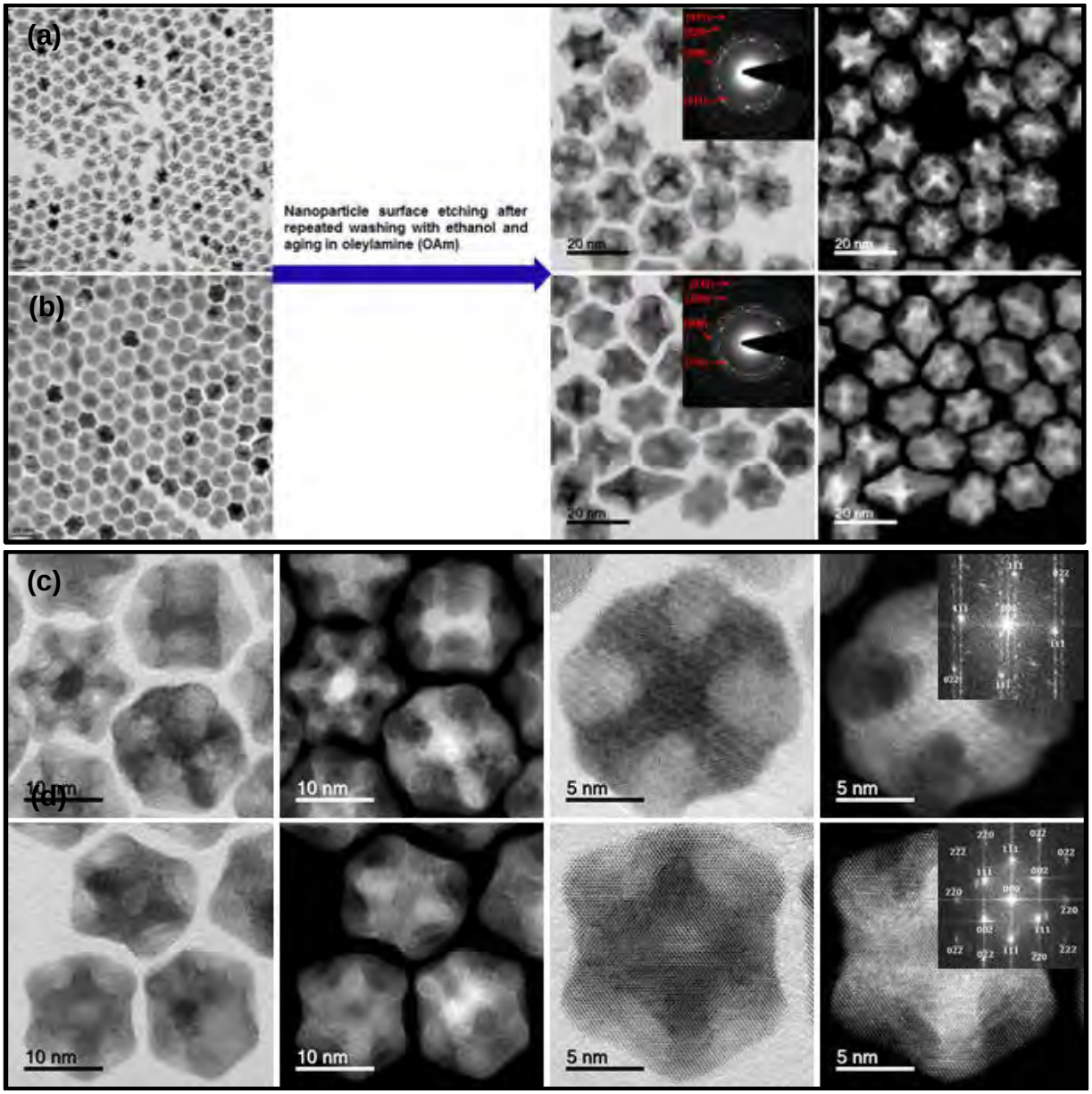

Figure 4.14*: Bright field STEM micrographs before aging in OAm (**a**-**b**, left column), after aging (**a**-**b**, right column) and the corresponding HAADF micrographs. The inserts in bright field STEM micrographs are SAED patterns. HR-STEM micrographs (**c**-**d**) and the respective FFT diffractograms of (**a**) PtNi-OLEA and (**b**) PtNi-TOA nanoparticles. The inserts in HR-HAADF micrographs (**c**-**d**, right column) are FFT patterns.

Figure 4.15 shows the particle distribution histogram of the PtNi nanoparticles. On the basis of the TEM images, the average particle diameters of the nanoparticles were determined as 18.3 ± 1.7 nm for PtNi-OLEA and 15.6 ± 1.1 nm for PtNi-TOA nanoparticles.

*Images acquired with the expert assistance of Dr David Mitchell, University of Wollongong

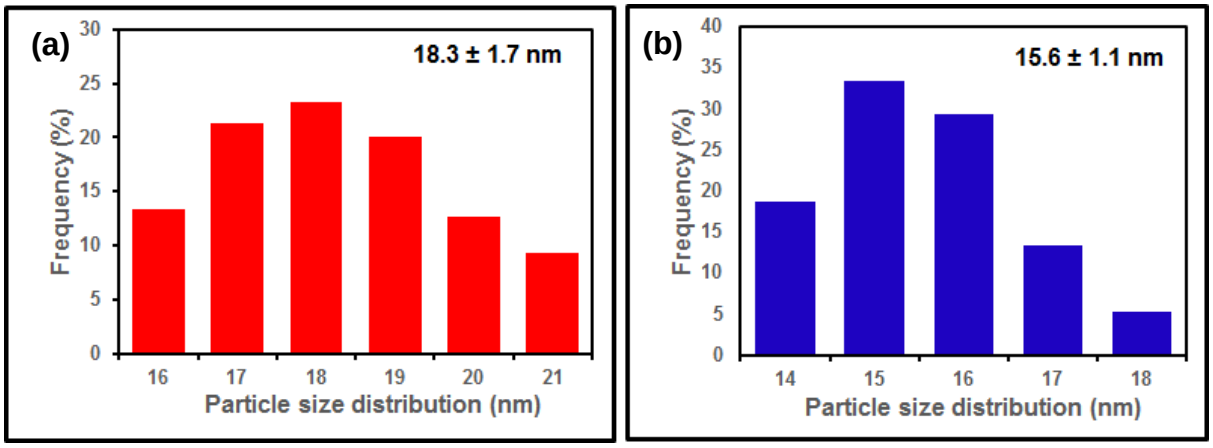

Figure 4.15: Particle size distribution (nm) histograms of (**a**) PtNi-OLEA and (**b**) PtNi-TOA.

Figure 4.16 shows HAADF-STEM-EDS elemental mapping for (**a**) PtNi-OLEA and (**b**) PtNi-TOA nanoparticles. All the nanoparticles show a random homogeneous distribution of both Ni and Pt within the single particle crystals, indicating that these are mixed alloy nanoparticles. There is also evidence of a substructure with Pt preferentially depositing on the facet apices and edges. The chemical compositions of the nanoparticles were determined using STEM-EDS. The overall average compositions are shown in Table 4.7.

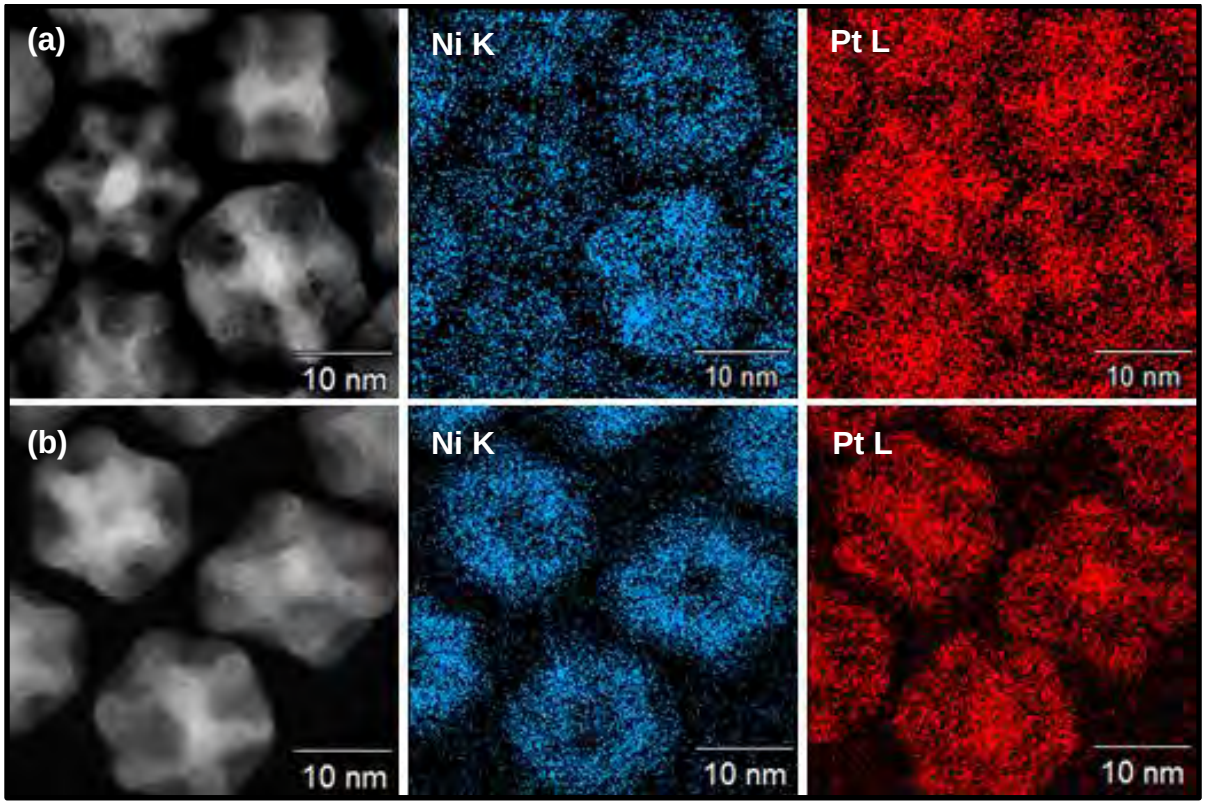

Figure 4.16*: HAADF-STEM-EDS elemental mapping for (**a**) PtNi-OLEA and (**b**) PtNi-TOA nanoparticles, revealing elemental distribution within single crystalline particles.

*Images acquired with the expert assistance of Dr David Mitchell, University of Wollongong

Table 4.7: Elemental compositions of (**a**) PtNi-OLEA and (**b**) PtNi-TOA alloy nanoparticles.

Alloys	Element Line	Atom %
PtNi-OLEA	Ni K Pt L	22.65 77.35
PtNi-TOA	Ni K Pt L	25.93 74.07

4.3.2 X-ray Diffraction (XRD) Analysis

X-ray diffraction (XRD) spectra for these PtNi nanoparticles are shown in Fig. 4.17. Five 2θ diffraction peaks were detected for both binary nanoparticles; these were both indexed to (111), (200), (220), (311) and (222) planes. The patterns are characteristic of a face-centred cubic (fcc) phase; as observed for PtNi alloys in 4.1, peak positions were shifted toward higher angles than pure Pt, showing incorporation of Ni in the nanoparticles and random elemental distribution. No other diffraction peaks were identified, further demonstrating that only a characteristic single phase solid solution of fcc PtNi exists in all the individual products. The measured *d*-spacings for (111) plane in both PtNi-OLEA and PtNi-TOA was 0.219 nm whereas for (200) plane in PtNi-OLEA and PtNi-TOA were 0.190 and 0.192 nm, respectively, all these values are consistent with the literature values for Pt_3Ni nanoparticles[27, 326] (Table 4.8).

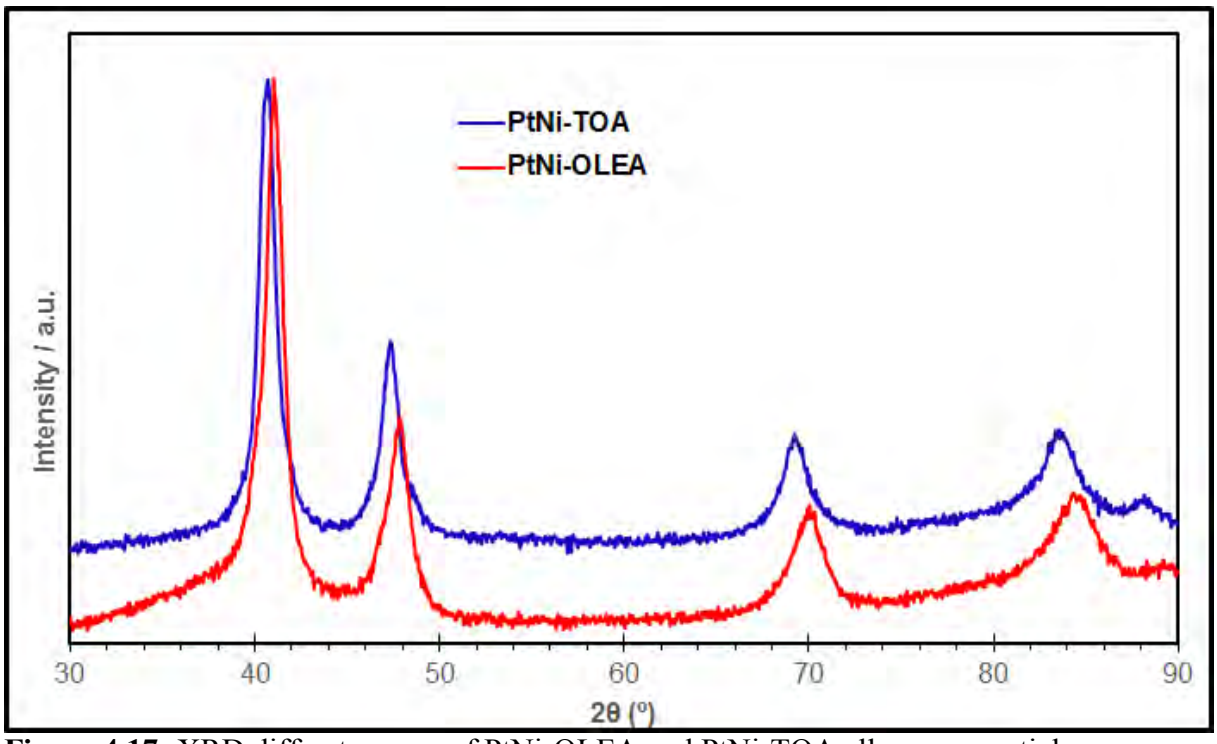

Figure 4.17: XRD diffractograms of PtNi-OLEA and PtNi-TOA alloy nanoparticles.

Table 4.8 shows calculations of lattice constants based on the XRD results, together with published values for lattice constant; calculated values for composition (from Vegard's Law[318, 319] using XRD results), and composition values from STEM-EDS results. The calculated average compositions were consistent with the compositions measured by STEM-EDS. The mean diameters of the nanoparticles were estimated from XRD data using the Debye-Scherrer equation[4]. The calculated volume average values of PtNi-OLEA (19.4 nm) and PtNi-TOA (17.3 nm) nanoparticles were slightly higher than values obtained from the STEM analysis of average particle size, as noted in 4.1.

Table 4.8: Summaries of the d-spacings on the basis of XRD and literature values, the average atomic composition based on Vegard's equation and STEM-EDS analysis.

Nanoalloys	2θ Diffraction peaks (°)	hkl	*d*-spacings (nm)	Literature values (*d*-spacing) (nm)[325, 326]	Lattice constants (nm)	Vegard's equation (composition)	STEM-EDS average composition (at.%)
PtNi-OLEA	41.05 47.83	(111) (200)	0.219 0.190	Pt_3Ni: 0.216 Pt_3Ni: 0.194	0.381 0.380	$Pt_{71}Ni_{29}$	$Pt_{71}Ni_{29}$
PtNi-TOA	40.68 47.34	(111) (200)	0.219 0.192	Pt_3Ni: 0.216 Pt_3Ni: 0.194	0.384 0.384	$Pt_{78}Ni_{22}$	$Pt_{74}Ni_{26}$

4.3.3 Electrochemical Surface Area and ORR Activity

Prior to electrochemical investigations, the as-prepared Pt-based nanoparticles were dispersed on a highly conductive and high surface area carbon support (Vulcan XC-72R) via a colloidal-deposition method. Bright field STEM micrographs of carbon-supported nanoparticles are displayed in Figures 4.18(**a**)-(**b**), indicating their good dispersion with no apparent change in microstructure.

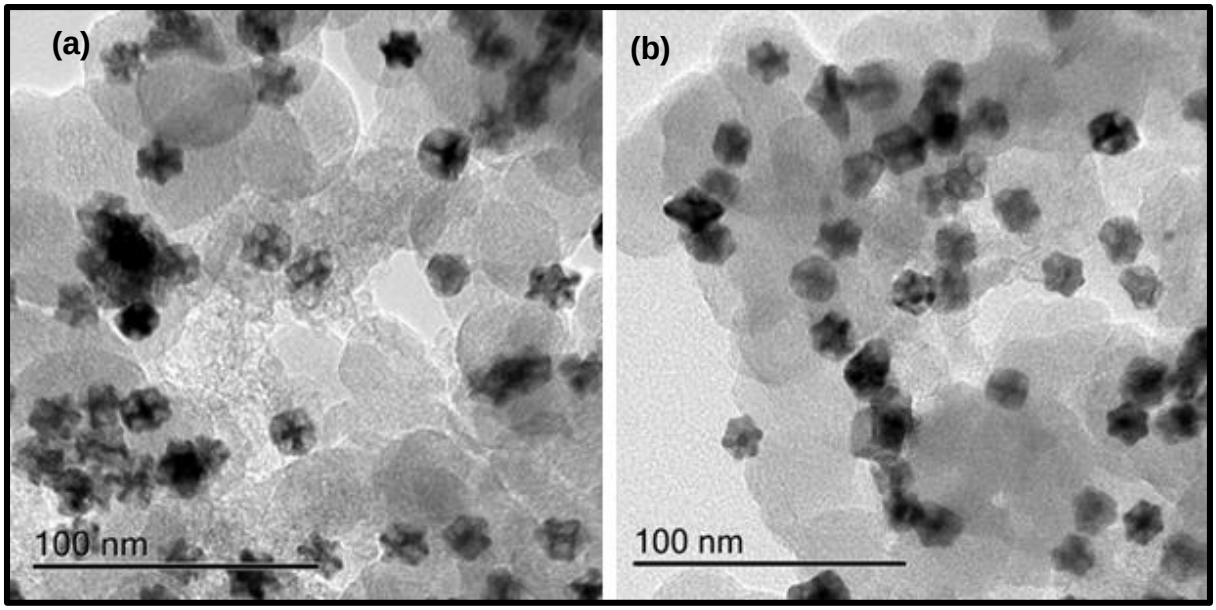

Figure 4.18: STEM micrographs of (**a**) PtNi-OLEA and (**b**) PtNi-TOA nanoparticles supported on high surface area carbon (Vulcan XC-72R).

Results from electrochemical testing are shown in Figure 4.19. Cyclic voltammetry (CV) (Fig. 4.19(**a**)) and carbon monoxide (CO) stripping voltammetry (Fig. 4.19(**b**)) were used to investigate the electrochemical surface area (ECSA) of these nanoparticles (Fig. 4.19(**a**)). The ECSAs scaled as follows: PtNi-TOA/C (162.6 $m^2g_{Pt}^{-1}$) > PtNi-OLEA/C (124.3 $m^2g_{Pt}^{-1}$) >> commercial Pt/C (70.9 $m^2g_{Pt}^{-1}$) whereas the $ECSA_{CO}$ investigated scale as follows: commercial Pt/C (198 $m^2g_{Pt}^{-1}$) > PtNi-TOA/C (187 $m^2g_{Pt}^{-1}$) > PtNi-OLEA/C (143.4 $m^2g_{Pt}^{-1}$), consistent with the $ECSA_{Hupd}$. The ratios determined between $ECSA_{CO}$ and $ECSA_{Hupd}$ ($ECSA_{CO}/ECSA_{Hupd}$) for the alloy nanoparticles were approximately 1.2, indicative of nominal differences in terms of both H_{ads} and CO_{ads} surface coverage.

The inherent anisotropic nature of the shapes and surface defects such as hollow edges/corners, interfaces, steps, kinks as well as different crystal planes, and the associated good ECSAs of these alloy nanoparticles, serve as the key building-blocks for more accessibility of reacting molecules to the catalyst surface structure for the ORR.

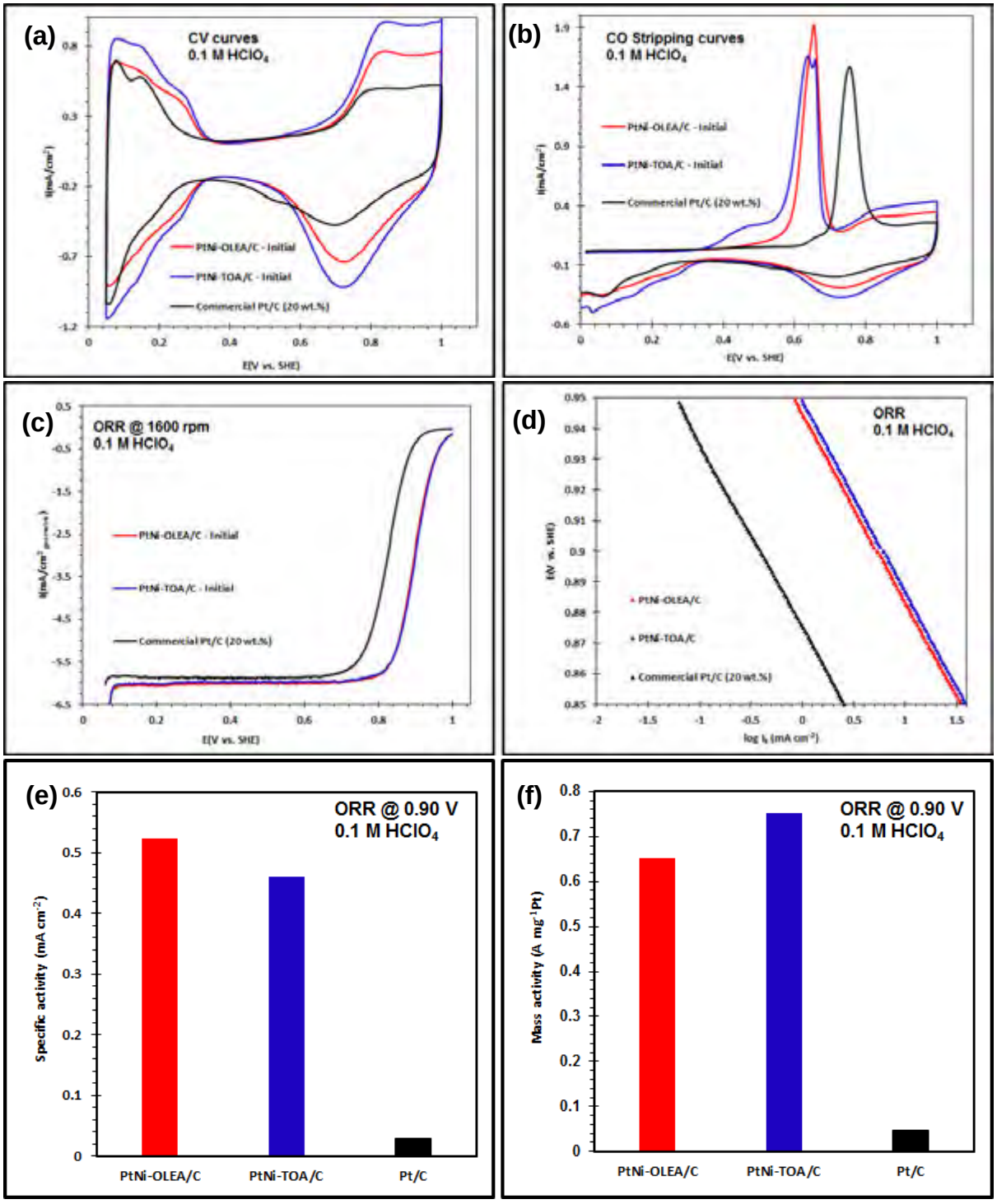

Figure 4.19: (**a**) Cyclic voltammograms of binary Pt-based alloys (PtNi-OLEA/C (red), PtNi-TOA/C (blue) and Pt/C (black)), (**b**) CO-stripping voltammetry curves, (**c**) ORR polarization curves, (**d**) the corresponding Tafel plots, (**e**) intrinsic area-specific activities and (**f**) mass-specific activities at +0.9 V (vs SHE).

All the ORR polarization curves reached the diffusion limited-current at ~ 6.0 mA cm^{-2} (Fig. 4.19(**c**)). These experimental values are consistent with the reported theoretical values (5.8 - 6.02 mA cm^{-2}) [87, 309-311]. The measured currents were corrected for mass transport to acquire

the true kinetic currents. Tafel plots (Fig. 4.19(**d**)) obtained from the potentials in the range of +0.85 – 0.95 V (vs SHE), exhibit the following activity trend: PtNi-TOA/C > PtNi-OLEA/C >> commercial Pt/C. Consequently, these plots indicate that both PtNi-OLEA and PtNi-TOA/C electrocatalysts display the most positive onset potential compared with the Pt/C electrocatalysts, indicating superior catalytic performance of these binary nanoparticles.

The Pt area-specific activities and mass-specific activities of these nanoparticles were benchmarked against the commercial Pt/C electrocatalysts (Figs. 4.19(**e**)-(**f**)). The Pt mass-specific activities for the effective Pt utilisation at +0.9 V (vs SHE) of PtNi-OLEA/C and PtNi-TOA/C exhibit ~18 and 20 ORR enhancement functionality, respectively, compared with the commercial Pt/C. In conjunction with the mass-specific activity evaluations, the specific activities to investigate the absolute value of the electrocatalyst intrinsic area-specific activity of PtNi-OLEA/C and PtNi-TOA/C display ~10 and 9-fold activity enhancement, respectively, compared with that of the commercial Pt/C catalyst.

4.3.4 Durability Measurements

The stability of these nanoparticles was also investigated after potential cycling to 5000 cycles (Fig. 4.20(**a**)). Two current peaks emerged with potential cycling, and can be attributed to {100} and {110} surface sites (labelled in Fig. 4.20(**a**)), where hydrogen adsorption (H_{ads}) occurs. Again, these surface sites are characteristics of pure polycrystalline Pt with the {110} surface sites binding the hydrogen more strongly than the {100} surface sites[293]. This indicates progressive leaching of Ni from the originally more Ni-rich alloys.

The $ECSA_{Hupd}$ reduction with prolonged potential cycling was also evaluated by deploying CO stripping (Fig. 4.20(**b**), dashed lines). The decline in CO current peaks and a positive shift from lower to higher potentials is possibly due to Ni/Ni oxide disintegration, leading to less CO tolerance of the nanoparticles, and the appearance of double peaks with increasing potential cycling. The latter suggest that this is due to particle agglomeration and the existence of defects (more negative peak), segregated particles (more positive peak) [316, 322] (labels and inserts in Fig. 4.20(**b**)), preferential/selective binding onto distinct facets[323], or the nature of the surface sites or particle size distribution[87, 316].

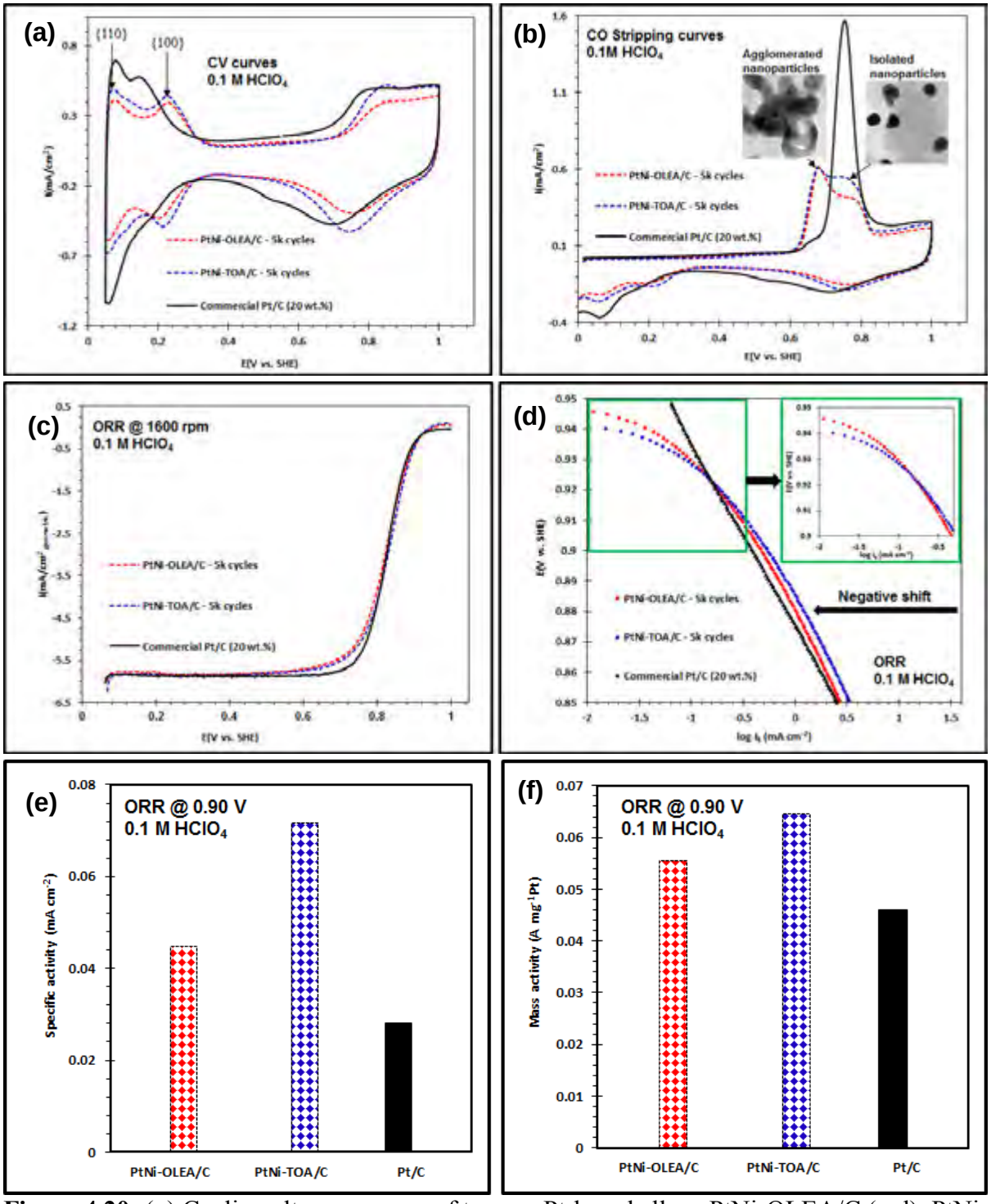

Figure 4.20: (**a**) Cyclic voltammograms of ternary Pt-based alloys PtNi-OLEA/C (red), PtNi-TOA/C (blue) and commercial Pt/C (black), (**b**) CO-stripping voltammograms, (**c**) ORR polarization curves, (**d**) the corresponding Tafel plots, (**e**) intrinsic area-specific activities and (**f**) mass-specific activities at +0.9 V after 5000 cycles, respectively. Durability measurements for the commercial Pt/C electrocatalysts were not conducted.

After prolonged potential cycling (up to 5000 cycles) all the nanomaterials showed significant decay in the ORR performance, with the polarization curves shifting from higher (positive) to lower (negative) potentials (Fig. 4.20(**c**)), dashed lines). This can also be seen from the

corresponding Tafel plots (Fig. 4.20(**d**)). The dissolution of Ni/Ni oxide and consequent formation of Pt and PtO surface layers at higher potentials (low current density region) shifted the onset potential. This yielded the Tafel slope < 60 mV/dec for potentials above 0.91 V vs SHE (insert in Fig. 4.20(**d**)). Since a smaller Tafel slope indicates a lower exchange current density, this suggests that the fractional formation of the oxide layer on Pt surface impedes the ORR mechanism.

In terms of area-specific activity the catalysts presented here still show slightly higher performance (by a factor of ~1) than commercial Pt/C while in terms of mass-specific activity all the catalysts show at least a doubling in activities relative to Pt/C (Figs. 4.20(**e**)-(**f**)). The latter results again suggest the dissolution of Ni from the Pt alloy nanoparticles, hence the degradation of the alloys nanostructure functionalities.

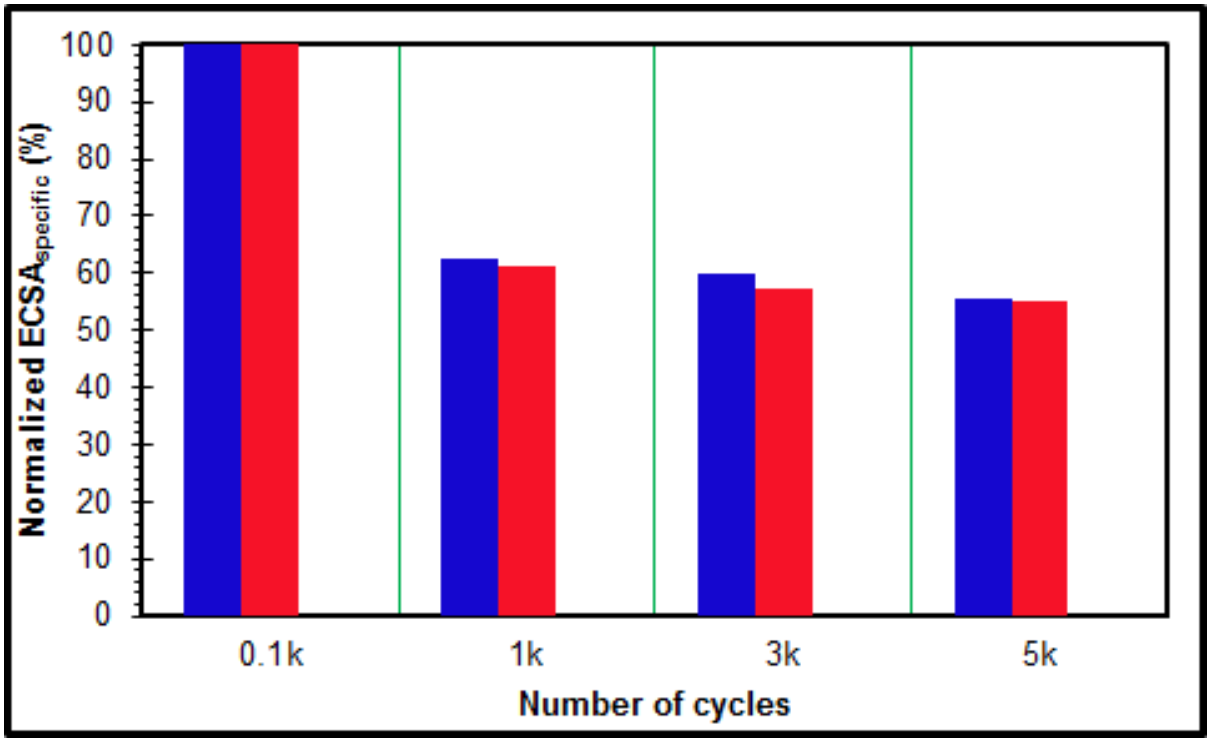

Figure 4.21: ECSA decay as a function of the continual potential cycling (up to 5000 cycles) of PtNi-OLEA/C (red) and PtNi-TOA/C (blue) binary nanoparticles.

The $ECSA_{Hupd}$ after 5000 cycles (as a percentage of the initial value) was 44% for PtNi-OLEA/C and 45% for PtNi-TOA/C. The decline in $ECSA_{Hupd}$ of these binary nanoparticles (Fig. 4.21) with respect to prolonged potential cycling could arise from any of the following changes: Ni/Ni oxide dissolution; particle surface migration on the carbon support followed by

coalescence; metal alloy oxide formation as a result of prolonged potential cycling and morphological deformations[293, 324, 325].

Table 4.9: Comparisons of the alloys, morphology, particle size diameter, $ECSA_{Hupd}$, $ECSA_{CO}$, $ECSA_{CO}/ECSA_{Hupd}$, mass-specific and area-specific activities at 0.9 V of two binary nanoparticles.

Nanoalloy	Nanoalloy shapes	Particle diameter (nm)	ECSA (m^2/g_{Pt}) (CV)	ECSA (m^2/g_{Pt}) loss (%)	ECSA (m^2/g_{Pt}) (CO stripping)	ECSA (m^2/g_{Pt}) (CO stripping) loss (%)	Mass activity (A/mg_{Pt})	Mass activity loss (%)	Specific activity (mA/cm^2_{Pt})	Specific activity loss (%)
PtNi-OLEA (20 wt.%)	Elongated polyhedral and cuboidal	18.3 ± 1.7	0.1K Cycles: 124.3	44	0.1K Cycles: 143.4	42	0.65	91	0.52	91
			5K Cycles: 69.1		5K Cycles: 82.7		0.056		0.045	
PtNi-TOA (20 wt.%)	Elongated polyhedral and Cuboctahedra	15.6 ± 1.1	0.1K Cycles: 162.6	45	0.1K Cycles: 187	47	0.75	91	0.46	84
			5K Cycles: 89.9		5K Cycles: 100.1		0.065		0.072	
Commercial Pt/C (20 wt.%)	Spherical	3.3 ± 2.4	0.1K Cycles: 71.0	-	0.1K Cycles: 198.0	-	0.037	-	0.052	-

The novel sequential solution-based synthetic approach reported herein resulted in the formation of highly monodisperse, crystalline and anisotropic nanoparticles of homogeneous PtNi solid solution. These binary nanoparticles, however, showed poor storage stability and flocculated. The surfactant OAm, used to transform the agglomerated particles into a homogeneous colloidal dispersion, etched the surface of the nanoparticles in a preferential/selective mode, creating novel crystal facets. As a result of these newly evolved morphologies and compositional changes, the surface etched nanoparticles exhibited an excellent electrocatalytic activity in the ORR compared with the commercial Pt/C electrocatalysts. The preliminary durability measurements showed activity decay to a value comparable to that of the initial commercial Pt/C electrocatalyst measurements.

4.4 Co-reduction by Thermolysis: Binary (PtNi and PtCo) and Ternary (PtNiCo) Nanoparticles

4.4.1 Scanning Transmission Electron Microscopy (STEM) Analysis

This co-reduction by thermolysis route yielded nanoparticles of dendritic morphologies, as revealed by STEM. Figure 4.22 shows SE images (first column), BF TEM images (second column), HR-STEM (third column) and the corresponding HAADF micrographs (final column) of binary (**a**) PtNi, (**b**) PtCo and ternary (**c**) PtNiCo nanoparticles. These nanoparticles were synthesised using identical experimental parameters. All the nanoparticles have surfaces which exhibit a large number of low-coordination edges, as seen in the open structures with large numbers of edges and corners. The FFT analyses (inserts in HAADF) show that the nanoparticles all exhibit polycrystalline, face-centred cubic (fcc) structures.

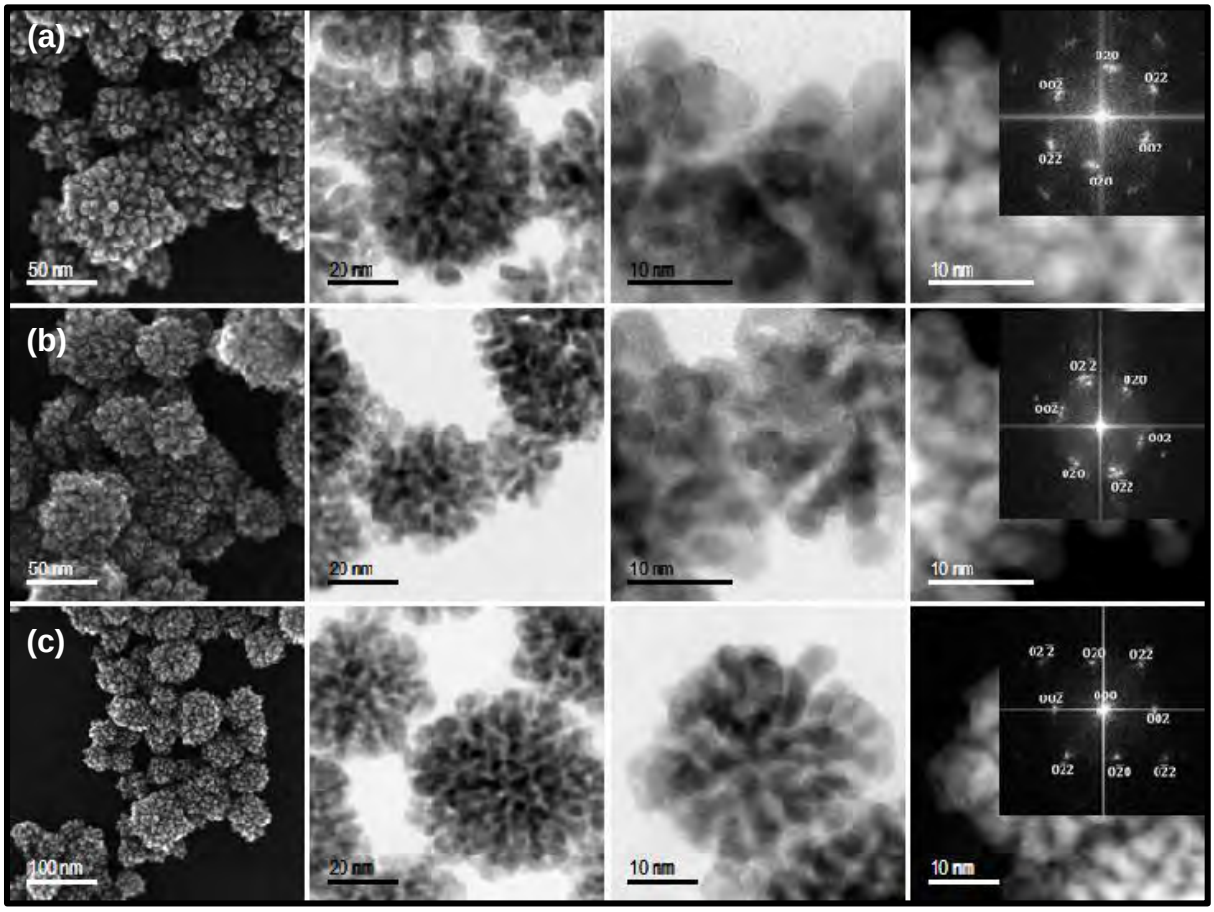

Figure 4.22*: SEM (left column), STEM micrographs, HR-STEM and the corresponding HAADF images of both binary (**a**) Pt_3Ni and (**b**) Pt_3Co, and ternary (**c**) Pt_3NiCo nanoparticles. FFTs are inserts in HAADF-STEM micrographs.

On the basis of the TEM images, the average particle diameters (not shown) of the nanoparticles were determined as 63 ± 5.4 nm, 59 ± 7.1 nm and 73 ± 8.8 nm for PtNi, PtCo and PtNiCo, respectively.

HAADF-STEM images and their corresponding X-ray elemental maps were acquired, as shown in Figure 4.23. The nanoparticles are all seen to exhibit a homogeneous atomic distribution of Pt and the alloying elements (Ni and/or Co). Compositional mapping of the phases carried out in STEM investigations show that the atomic compositions of the nanoparticles were as follows: $Pt_{71}Ni_{29}$, $Pt_{72}Co_{28}$ and $Pt_{72}(NiCo)_{28}$. These compositions agree well with the 3:1 initial molar ratios of Pt to Ni and/or Co in their respective precursor salts.

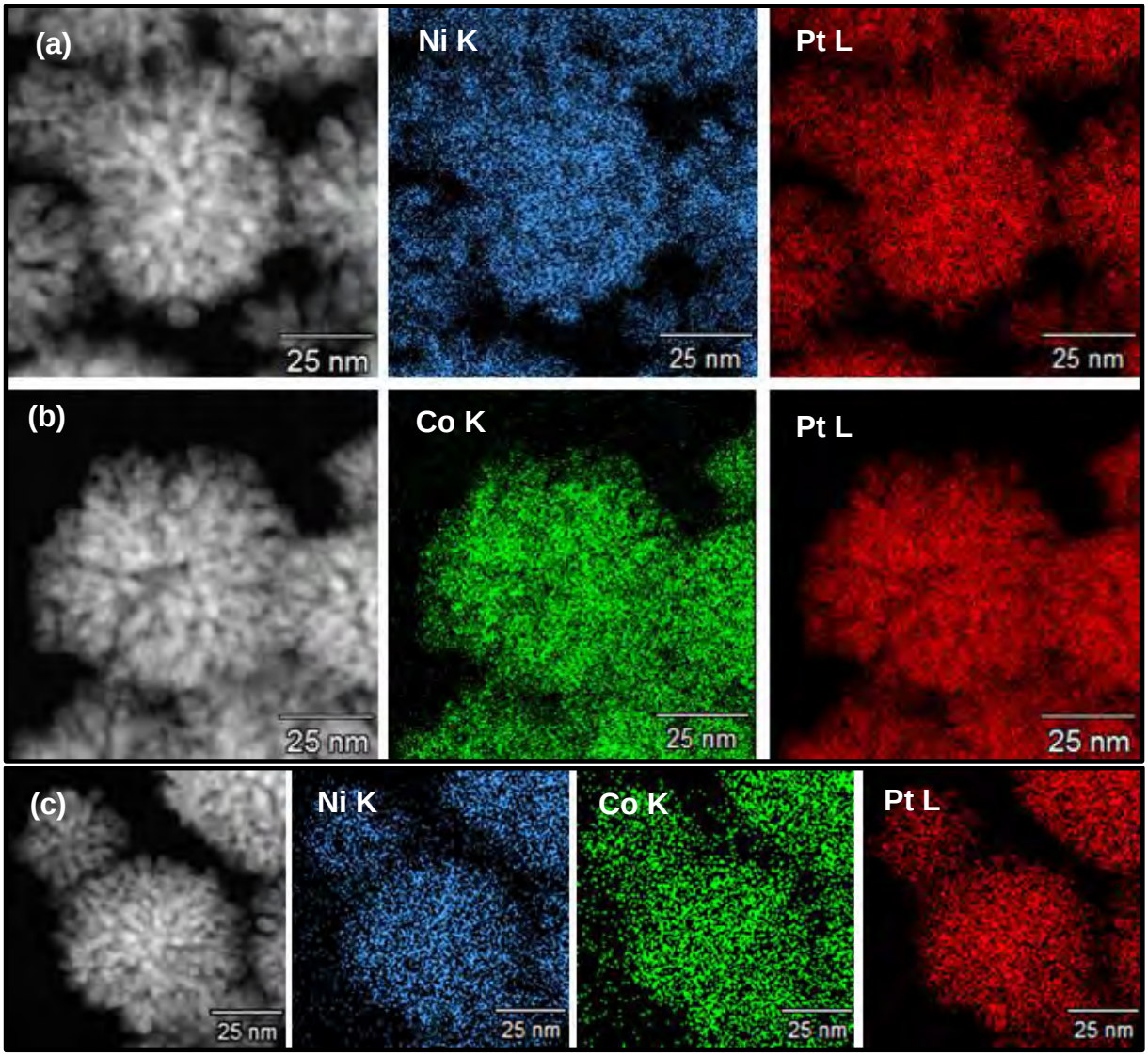

Figure 4.23*: HAADF-STEM-EDS elemental mapping results for both binary (**a**) PtNi and (**b**) PtCo, and ternary alloys (**c**) PtNiCo, exhibiting a homogeneous distribution of the elements within the nanoparticles.

*Images acquired with the expert assistance of Dr David Mitchell, University of Wollongong

4.4.2 X-ray Diffraction (XRD) Analysis

Figure 4.24 shows X-Ray Diffraction (XRD) spectra for the binary and ternary nanoparticles. Five 2θ diffraction peaks can be indexed to (111), (200), (220), (311) and (222) respectively, characteristic of a face-centred cubic (fcc) Pt-based solid solution. The slight shift of the peak positions toward higher angles, relative to pure Pt, suggests a decreased lattice parameter. This is consistent with a reduced lattice parameter due to Pt replacement by smaller atoms (in this case, Ni and/or Co) in the crystal lattice. There were no additional XRD peaks detected, indicating that the phase was a random solid solution. These results are in good agreement with the HAADF-STEM-EDS elemental mapping investigations.

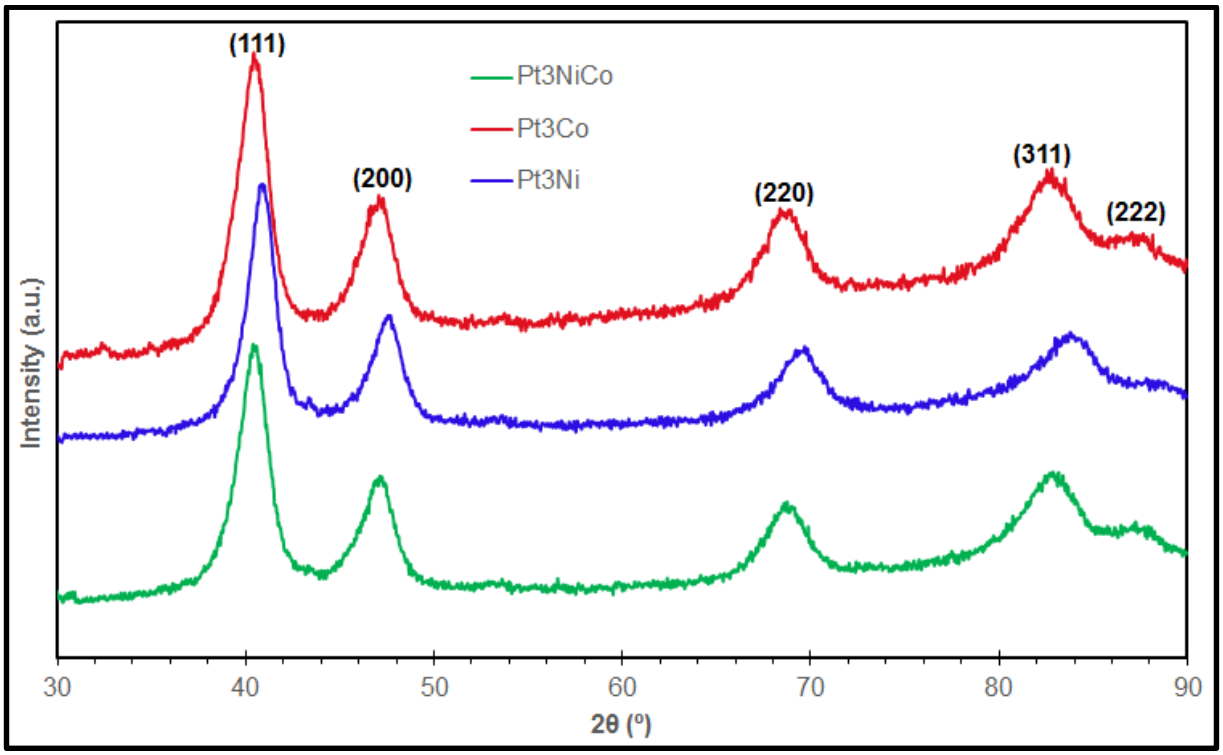

Figure 4.24: XRD patterns of Pt_3Ni, Pt_3Co and Pt_3NiCo alloy nanodendrites.

The measured *d*-spacings for (111) plane were 0.221, 0.223 and 0.223 for Pt_3Ni, Pt_3Co and Pt_3NiCo, respectively. The *d*-spacings for (200) plane were 0.191, 193 and 0.193 nm for Pt_3Ni, Pt_3Co and Pt_3NiCo, respectively, slightly different from the literature values[27, 326]. Table 4.10 summarizes the d-spacings on the basis of XRD and literature values, the average atomic composition based on STEM-EDS analysis.

Table 4.10: Pt_3Ni, Pt_3Co and Pt_3NiCo binary nanoparticles: calculated lattice constants from XRD, and from the scientific literature; calculated composition from XRD and Vegard's law and measured composition from STEM-EDS analysis.

Nanoalloys	2θ Diffraction peaks (°)	hkl	*d*-spacings (nm)	Literature values (*d*-spacing) (nm)[325, 326]	Lattice constants (nm)	STEM-EDS average composition (at.%)
Pt_3Ni	40.89 47.55	(111) (200)	0.221 0.191	0.216 0.194	0.382 0.382	$Pt_{71}Ni_{29}$
Pt_3Co	40.47 47.00	(111) (200)	0.223 0.193	0.218 0.192	0.386 0.386	$Pt_{72}Ni_{28}$
$Pt_3(NiCo)$	40.46 47.12	(111) (200)	0.223 0.193	- -	0.386 0.385	$Pt_{72}(NiCo)_{28}$

4.4.3 Electrochemical Surface Area and ORR Activity

Figures 4.25(**a**)-(**c**) show TEM images of the carbon-supported nanoparticles (Pt_3Ni/C, Pt_3Co/C and Pt_3NiCo/C) prior to electrochemical measurements. These highly dispersed particles show no apparent change in particle size or morphology following dispersion onto the support.

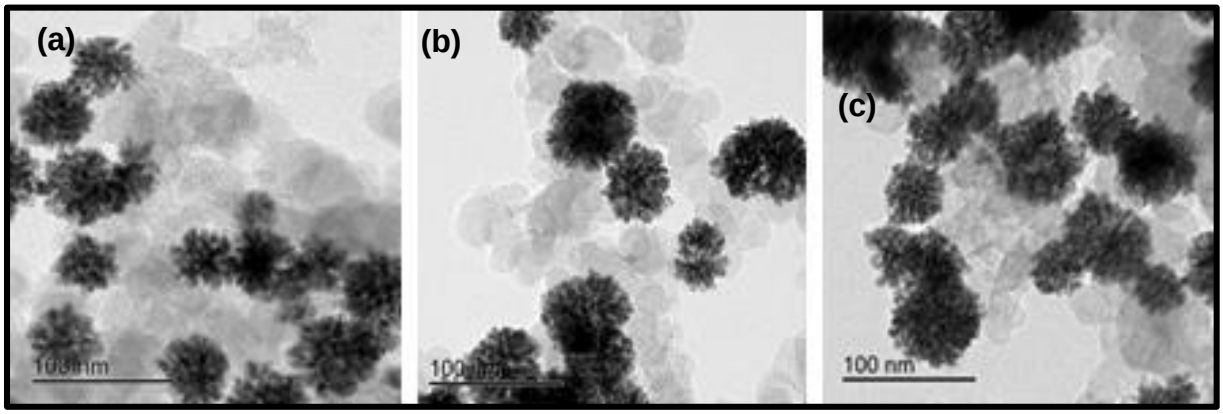

Figure 4.25: TEM micrographs of (**a**) Pt_3Ni, (**b**) Pt_3Co and (**c**) Pt_3NiCo nanoalloys supported on high surface area carbon (Vulcan XC-72R).

Figure 4.26(**a**) shows CV voltammograms of all the alloys and commercial Pt/C electrocatalysts. The hydrogen desorption/adsorption and oxide formation/reduction peak currents of these nanoalloys are seen to scale in intensity in the following order: Pt_3NiCo > Pt_3Ni > Pt_3Co>> commercial Pt/C. The oxide regimes suggest the possible formation of some Ni oxide and/or Co oxides and their subsequent dissolution with the cleaning of the nanostructure surface[87, 327]. The ECSAs evaluated by integrating in the H_{upd} region (further referred to as $ECSA_{Hupd}$), showed an increase in the following sequence: Pt_3NiCo (78.5 $m^2g_{Pt}^{-1}$) > Pt_3Ni (63.8 $m^2g_{Pt}^{-1}$) > Pt_3Co (52.5 $m^2g_{Pt}^{-1}$) >> commercial Pt/C (38.8 $m^2g_{Pt}^{-1}$) as shown in Table 4.11. The inherent dendritic anisotropic shapes and the remarkable ECSAs of these three

alloy nanoparticles demonstrate a high degree of accessibility of reacting molecules to the surface structure, rendering them superior electrocatalysts for the ORR.

In addition to determining $ECSA_{upd}$, carbon monoxide (CO) stripping was used to investigate the ECSA of the Pt alloy nanoparticle surfaces, to detect the presence of particle agglomerates or isolated nanoparticles[323]. The results obtained for CO-stripping are shown in Figure 4.26(**b**). The ECSA calculated by CO-stripping ($ECSA_{CO}$) showed an increase in the following sequence: commercial Pt/C (85.1 $m^2g_{Pt}^{-1}$) > Pt_3NiCo (80.1 $m^2g_{Pt}^{-1}$) > Pt_3Ni (65.1 $m^2g_{Pt}^{-1}$) >> Pt_3Co (53.5 $m^2g_{Pt}^{-1}$) as shown in Table 4.10, consistent with the $ECSA_{Hupd}$. The ratio determined between $ECSA_{CO}$ and $ECSA_{Hupd}$ ($ECSA_{CO}/ECSA_{Hupd}$) for all the nanoalloys is 1.02, indicative of insignificant differences in terms of both H_{ads} and CO_{ads} surface coverage. The evolution of multiple CO oxidation voltammetry peaks for individual alloys could be due to particle agglomeration and the existence of defects (more negative peak), segregated particles (more positive peak) [316, 322], preferential/selective binding onto distinct facets[323], and the nature of the surface sites or particle size distribution[87, 316].

Probing the ORR activity, polarization curves obtained from the three nanoalloys and commercial Pt electrocatalysts are displayed in Figure 4.26(**c**). All catalysts reached the theoretical limiting current density of 6.02 mA/cm^2[87, 309-311]. The Tafel plots obtained from the potentials in the range of 0.85 – 0.95 V are shown in Figure 4.26(**d**). The plots of these binary and ternary nanoalloys exhibit different functionalities which scale as follows: Pt_3NiCo/C > Pt_3Co/C >> Pt_3Ni/C >>> Pt/C. Consequently, the plots indicate that Pt_3NiCo/C displays the highest positive kinetic currents of all the electrocatalysts at any given potential, suggesting exceptional catalytic performance of these ternary branched nanomaterials.

The Pt area-specific activities and mass-specific activities of these nanostructured alloys were benchmarked against the commercial Pt/C electrocatalyst for Pt consumption (Table 4.11). The Pt mass-specific activities (Fig. 4.26(**e**)) and the area-specific activities (Fig. 4.26(**f**)) at 0.9 V of Pt_3NiCo/C, Pt_3Co/C, Pt_3Ni/C are approximately 5-fold and 3-fold higher than the reference commercial Pt/C electrocatalysts, respectively. These outstanding ORR functionalities can be attributed to the branched and open nature of the morphologies of the as-synthesized nanostructured alloys.

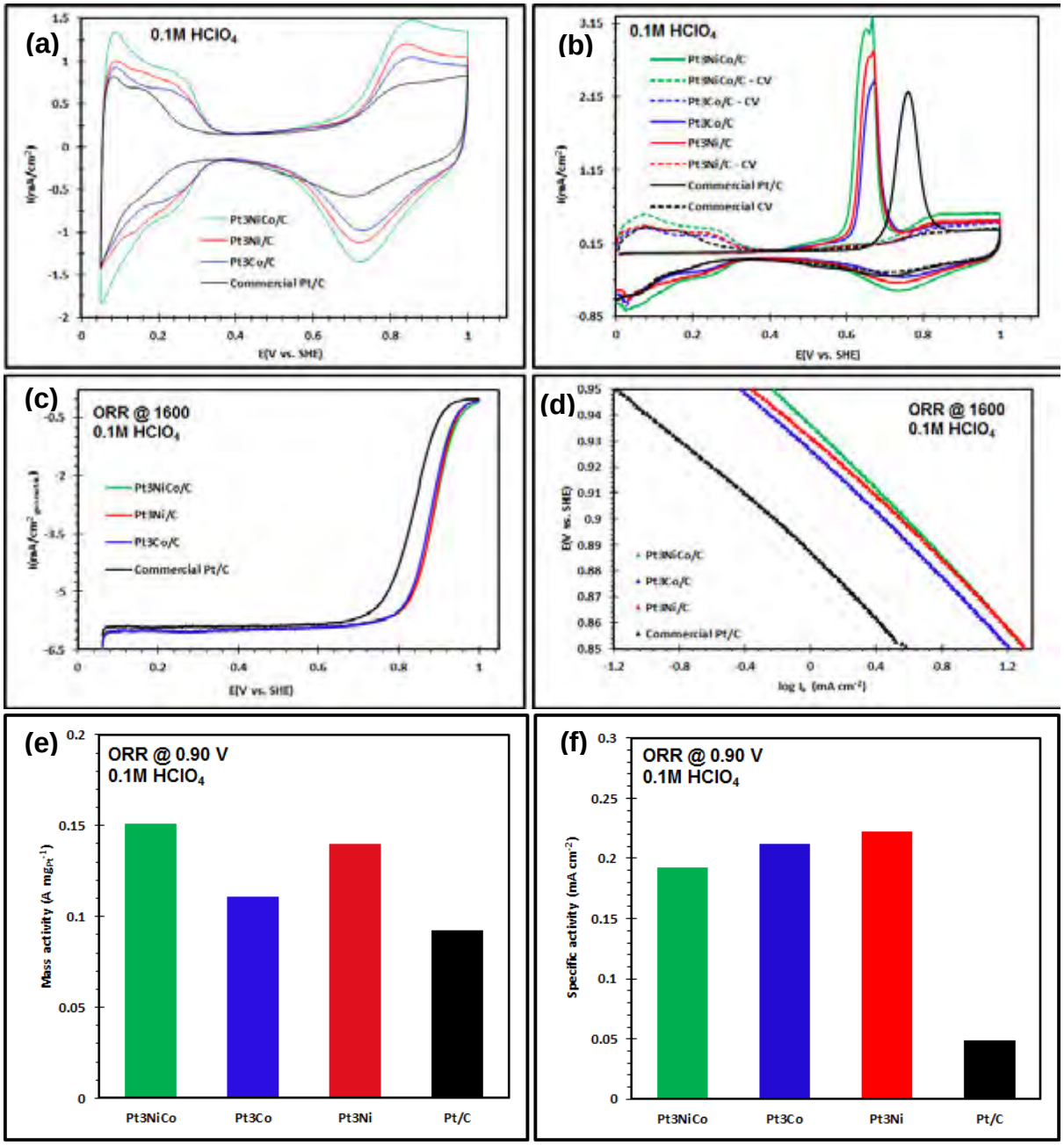

Figure 4.26: (**a**) Cyclic voltammograms of Pt/C, binary (Pt_3Ni/C and Pt_3Co/C) and ternary (Pt_3NiCo/C) Pt-based nanoalloys, (**b**) CO-stripping voltammetry (solid lines) and subsequent CV curves (dashed lines), (**c**) ORR polarization curves, (**d**) the corresponding Tafel plots, (**e**) mass-specific activities and (**f**) intrinsic area-specific activities at +0.9 V. Durability measurements for these three alloys and the commercial Pt/C electrocatalysts were not conducted.

Table 4.11: Comparisons of the morphology, particle size diameter, $ECSA_{Hupd}$, $ECSA_{CO}$, $ECSA_{CO}/ECSA_{Hupd}$, mass-specific and area-specific activities at 0.9 V of the binary and ternary nanoparticles.

Specimens	Nanoparticle morphologies	Particle diameter (nm)	ECSA (m^2/g_{Pt}) (CV)	ECSA (m^2/g_{Pt}) (CO stripping)	ECSA (CO_{ad})/ECSA (H_{upd})	Mass activity @ 0.9 V (A/mg_{Pt})	Specific activity @ 0.9 V (mA/cm^2_{Pt})
Pt_3Ni/C (60 wt.%)	Dendritic	63 ± 5.4	63.8	65.1	1.02	0.14	0.24
Pt_3Co/C (60 wt.%)	Dendritic	59 ± 7.1	52.5	53.5	1.02	0.11	0.21
Pt_3NiCo/C (60 wt.%)	Dendritic	73 ± 8.8	78.5	80.1	1.02	0.15	0.20
Commercial Pt/C (60 wt.%)	Spherical	7.3 ± 4.2	38.8	85.1	2.2	0.03	0.075

The use of the thermolysis protocol to synthesis binary and ternary Pt-based nanoalloys resulted in the formation of nanoparticles with a dendritic morphology. Electrochemical measurements show these nanoalloys to exhibit enhanced catalytic efficiencies toward the ORR compared to the state-of-the art commercial Pt/C electrocatalysts. The open-framework nature and unique branching of these alloys confers a high surface area, which can induce significant molecular accessibility. This in turn results in outstanding catalytic functonality for the sluggish ORR, providing new prospects for the rational design and engineering synthetic approaches of high performance dendritic multicomponet nanoparticles. It is worth noting that the long-term re-durability of these dendritic Pt alloy nanoparticles requires scrutiny.

4.5 Sequential Reduction by Thermolysis: PtNiV Ternary Nanoparticles

4.5.1 Scanning Transmission Electron Microscopy (STEM) Analysis

Zero-valent colloidal trimetallic PtNiV nanoparticles, stabilized by the surfactants OAm, ODA with or without OA, were synthesized by sequential thermolysis. Figure 4.27(**a**) shows the nanoparticles prepared in OAm and ODA as the surfactants (PtNiV) whereas Figure 4.27(**b**) exhibits nanoparticles synthesized in the presence of three stabilizers (PtNiV-OA): OAm, ODA and OA. The morphology, size and particle distribution were investigated by STEM, as seen in Figures 4.27(**a**)-(**b**). In both cases, there was no apparent particle agglomeration of the nanomaterials. HAADF and the corresponding bright-field STEM micrographs show highly monodisperse and faceted nanoparticles while HR-HAADF and the corresponding HR-STEM micrographs exhibit the highly crystalline nature of the nanoparticles with well resolved lattice fringes. Insets are FFTs.

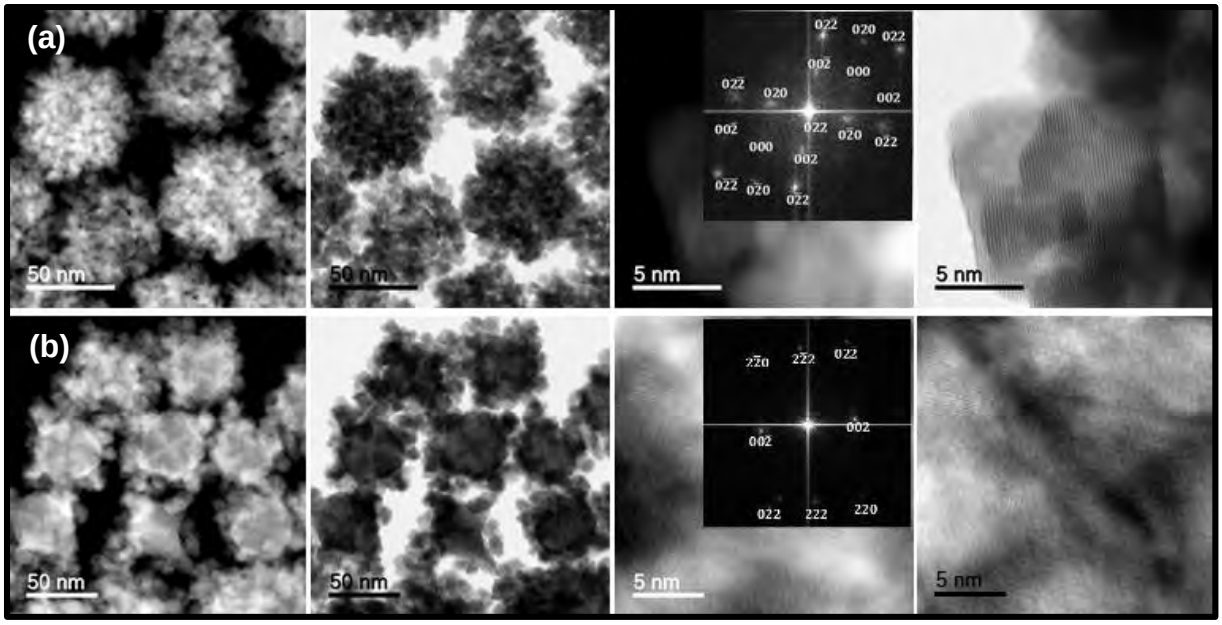

Figure 4.27*: (left to right) HAADF and STEM micrographs; HAADF and the corresponding HR-STEM images, of ternary (**a**) PtNiV and (**b**) PtNiV-OA nanoparticles. FFTs are inserts in HAADF-STEM micrographs.

Figures 4.28(**a**)-(**b**) shows the particle size distribution of these nanoparticles. On the basis of STEM micrographs, the mean particle diameters of about 300 – 350 nanoparticles were calculated as 69.5 ± 5.4 and 75.4 ± 4.5 nm for multi-stepped PtNiV and PtNiV-OA alloy nanoparticles, respectively.

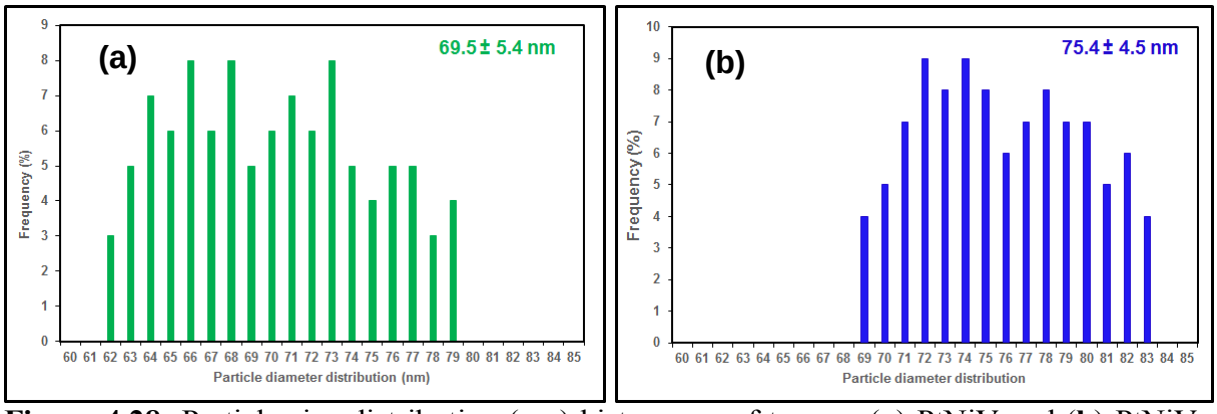

Figure 4.28: Particle size distribution (nm) histograms of ternary (**a**) PtNiV and (**b**) PtNiV-OA alloy nanoparticles.

The elemental distribution of single crystal nanoparticles of PtNiV and PtNiV-OA was determined using HAADF-STEM-EDS. Figures 4.29(**a**)-(**b**) show HAADF-STEM micrographs and the corresponding X-ray elemental maps for the as-synthesized ternary metallic nanoparticles. These nanoparticles exhibit a Ni-rich core which is small compared to

*Images acquired with the expert assistance of Dr David Mitchell, University of Wollongong

the homogeneous distribution of Pt and V; suggesting that the final structures are core-shell Ni-PtV nanomaterials.

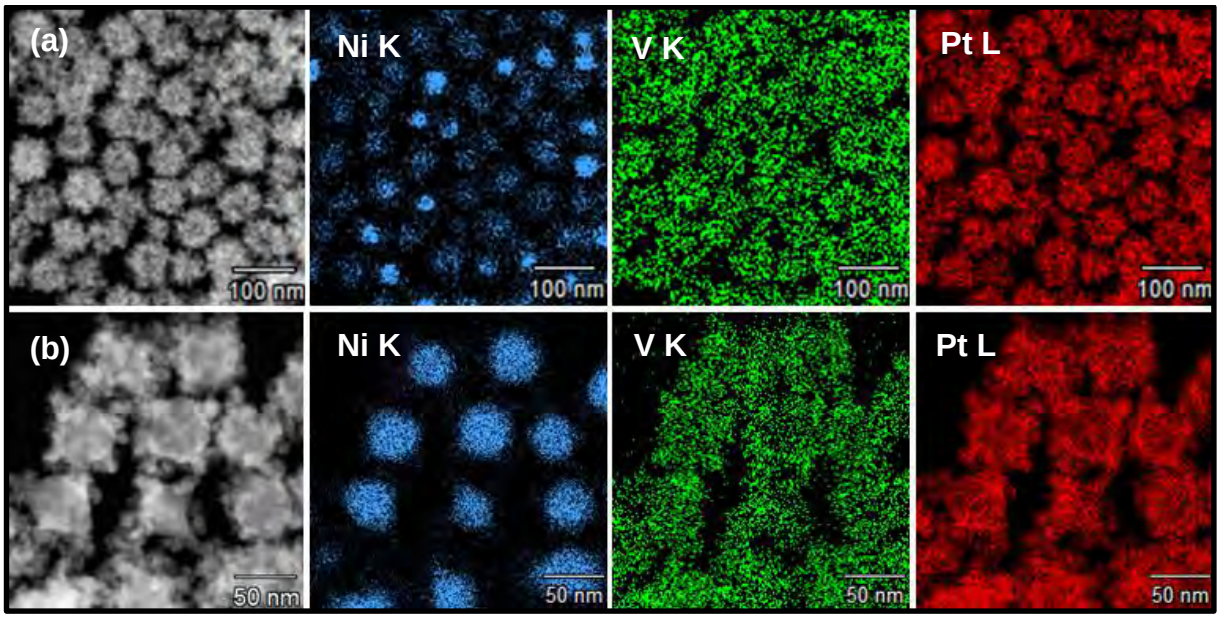

Figure 4.29*: HAADF-STEM-EDS elemental mapping for ternary (**a**) PtNiV and (**b**) PtNiV-OA alloy nanoparticles, revealing elemental distribution within single crystalline particles.

The chemical compositions of the corresponding branched ternary nanoparticles were determined using STEM-EDS (Table 4.12). STEM-EDS shows approximate compositions of $Ni_{11}V_5Pt_{84}$ for PtNiV, and $Ni_{20}V_4Pt_{76}$ for PtNiV-OA ternary nanoparticles. Although HAADF-STEM-EDS elemental mapping suggests core-shell Ni-PtV nanoparticles, STEM-EDS shows the composition for these alloys was close to $Pt_3(NiV)$.

Table 4.12: Elemental composition of (**a**) PtNiV and (**b**) PtNiV-OA ternary nanoparticles.

Alloys	Element Line	Atom %
PtNiV	V K	5.25
	Ni K	11.25
	Pt L	83.50
PtNiV-OA	V K	4.22
	Ni K	19.59
	Pt L	76.19

4.5.2 X-ray Diffraction (XRD) Analysis

Figure 4.30 shows X-Ray Diffraction (XRD) spectra for PtNiV ternary alloys. Five 2θ diffraction peaks detected were indexed to (111), (200), (220), (311) and (222) planes, characteristic of a face-centred cubic (fcc) phase. The slight shift of the peak positions toward

*Images acquired with the expert assistance of Dr David Mitchell, University of Wollongong

higher angles indicates a lower lattice parameter (*d*), due to partial replacement of Pt by Ni and V, both of which have a lower lattice parameter than Pt. The XRD results show no extra diffraction peaks for PtNiV nanoparticles whereas PtNiV-OA alloys show some splitting of the diffraction peaks, most notably the prominent (111) diffraction peak, suggesting the coexistence of two fcc phases.

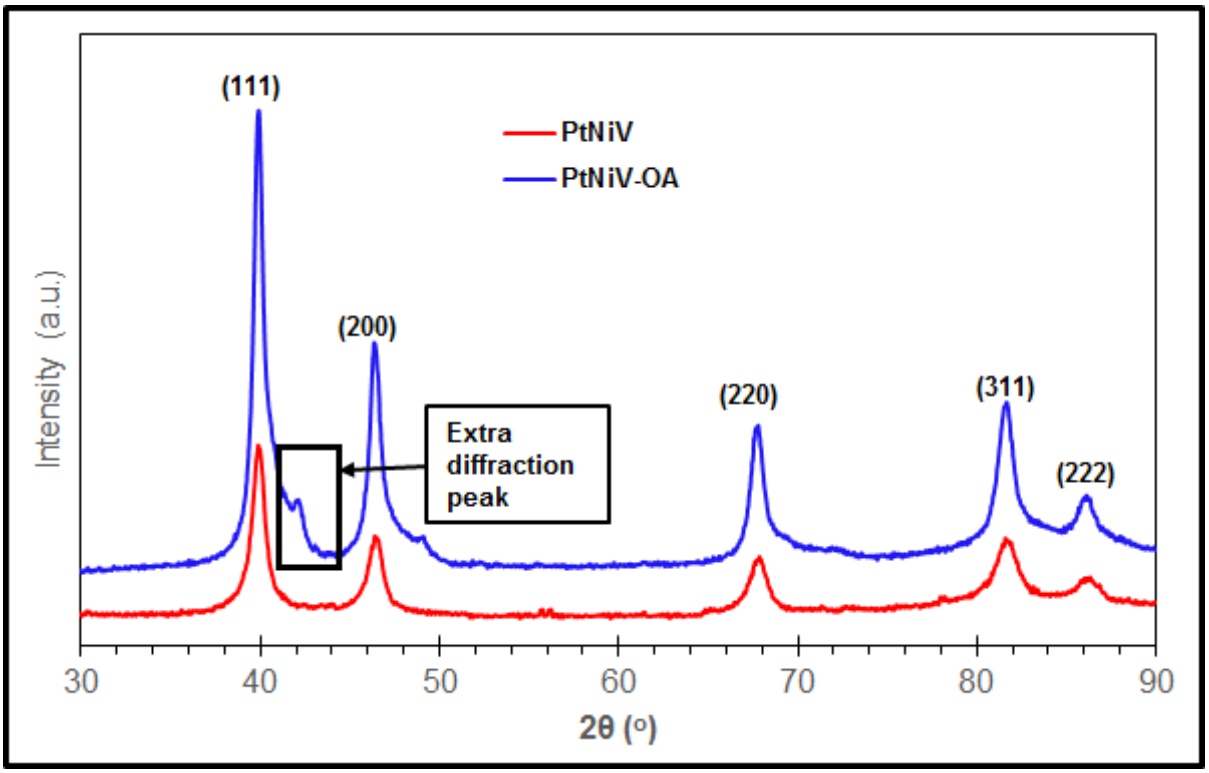

Figure 4.30: XRD diffractograms of PtNiV and PtNiV-OA ternary nanoparticles.

4.5.3 Electrochemical Surface Area and ORR Activity

Figures 4.31(**a**)-(**b**) display STEM micrographs of the carbon-supported ternary nanoparticles PtNiV and PtNiV-OA, respectively, prior to electrochemical evaluations. These highly dispersed particles show no apparent change in particle size or morphology of the nanoallys following dispersion onto the support. The surface electrochemical properties of these nanoalloys were then investigated using a rotating disk electrode (RDE).

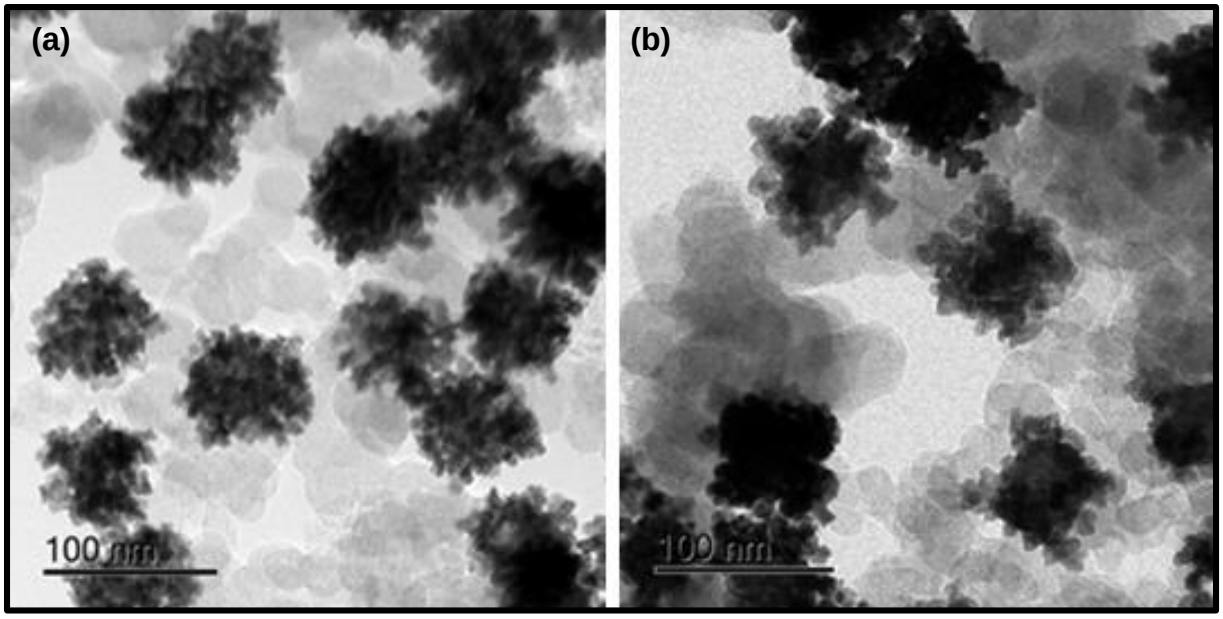

Figure 4.31: STEM micrographs of (**a**) PtNiV and (**b**) PtNiV-OA nanoparticles supported on high surface area carbon (Vulcan XC-72R).

Cyclic voltammograms (Fig. 4.32(**a**)) and CO-stripping voltammetry curves (Fig. 4.32(**b**)) were obtained to evaluate the ECSAs. The $ECSA_{Hupd}$ were calculated as follows: PtNiV-OA/C (140.1 $m^2g_{Pt}^{-1}$) > PtNiV/C (115.6 $m^2g_{Pt}^{-1}$) > commercial Pt/C (38.8 $m^2g_{Pt}^{-1}$) whereas the $ECSA_{CO}$ scaled as follows: PtNi-OA/C (148.8 $m^2g_{Pt}^{-1}$) > PtNiV/C (111 $m^2g_{Pt}^{-1}$) commercial Pt/C (85.1 $m^2g_{Pt}^{-1}$) as shown in Table 4.12, in good agreement with the $ECSA_{Hupd}$. The oxide formation/reduction peak currents of these nanoparticles became prominent in the following sequence: PtNiV-OA/C > PtNiV/C >> commercial Pt/C electrocatalysts, suggesting the influence of the alloying elements (Ni and V) in the evolution of the oxide peak currents. These oxide region currents suggest the formation of more NiV oxides.

The ratios determined between $ECSA_{CO}$ and $ECSA_{Hupd}$ ($ECSA_{CO}/ECSA_{Hupd}$) for all the nanoparticles were approximately 1 for both ternary alloys and 2.2 for the commercial Pt/C electrocatalyst, indicative of unsubstantial differences in terms of both H_{ads} and CO_{ads} surface coverage. The complex anisotropic nature of the shapes with more protruding surface defects such as branched edges/corners, stepped interfaces as well as distinct crystal planes and the superior corresponding ECSAs of these alloy nanoparticles serve as the key building-blocks for more accessibility of reacting molecules to the catalyst surface structure toward ORR.

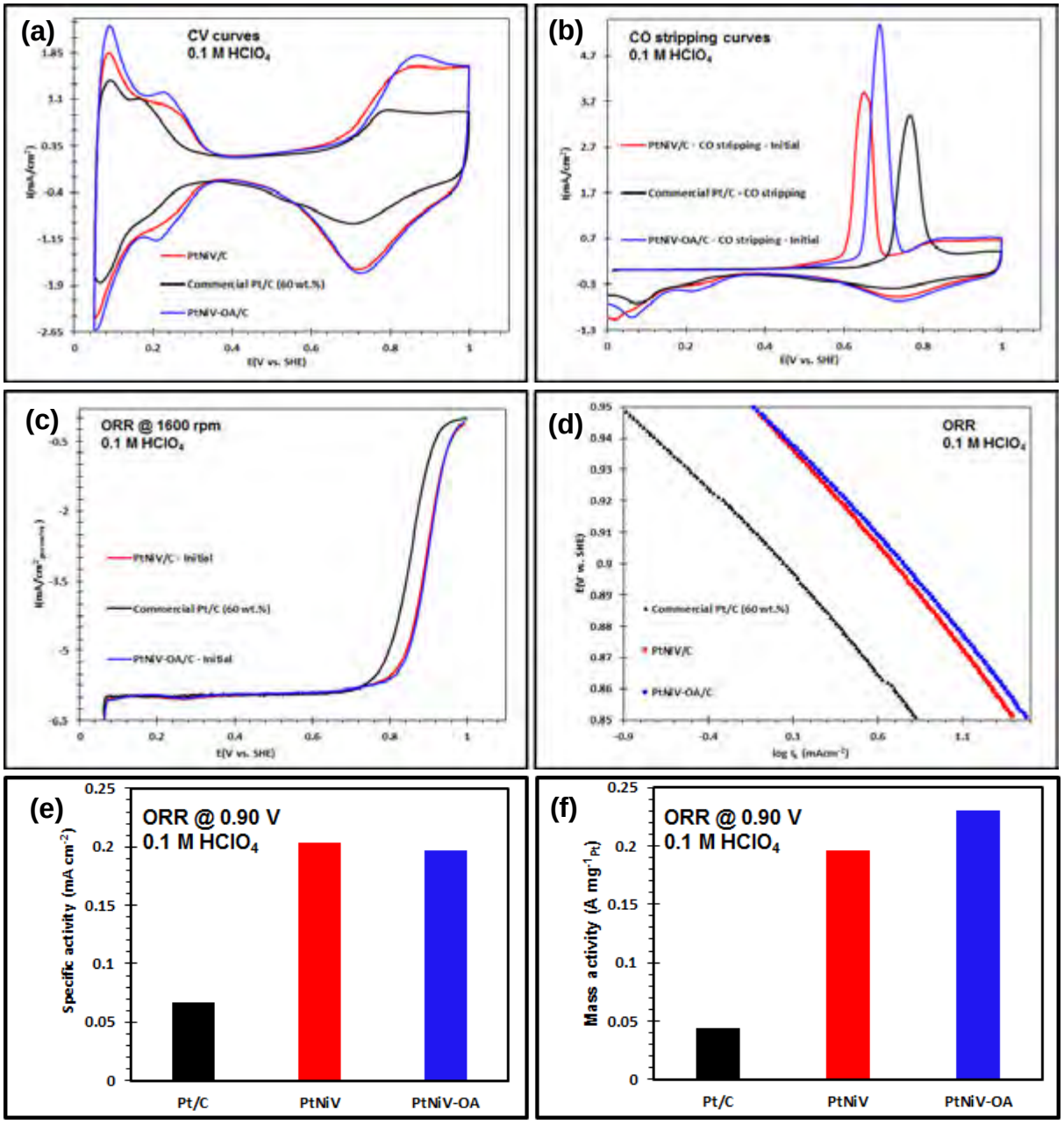

Figure 4.32: (**a**) Cyclic voltammograms of ternary Pt-based alloys (PtNiV/C (red), PtNiV-OA/C (blue)) and Pt/C (black), (**b**) CO-stripping voltammetry curves, (**c**) ORR polarization curves, (**d**) the corresponding Tafel plots, (**e**) intrinsic area-specific activities and (**f**) mass-specific activities at +0.9 V.

All the ORR polarization curves of the ternary nanoparticles, including the commercial Pt/C, reached their diffusion limited-current at ~ 6.0 mA/cm^2 (Fig. 4.32(**c**)), consistent with the reported theoretical value (5.7 - 6.02 mA/cm^2) [87, 309-311]. The measured currents were corrected for mass transport to acquire the true kinetic currents. The Tafel plots (Fig. 4.32(**d**)) obtained from the potentials in the range of 0.85 – 0.95 V, exhibit different functionalities which follow this trend: PtNiV-OA/C > PtNiV/C >> commercial Pt/C. Consequently, these plots indicate

that PtNiV-OA/C displayed more positive onset potential of all the electrocatalysts, suggesting enhanced catalytic performance of these ternary alloy nanoparticles.

The Pt mass-specific activities and area-specific activities of these two ternary nanoparticles were compared with the commercial Pt/C electrocatalysts (Figs. 4.32(**e**)-(**f**)). The Pt mass activities for the effective Pt utilization at 0.9 V of PtNiV-OA/C and PtNiV/C exhibit ~5.3 and 4.7 enhanced ORR functionality, respectively, compared with the commercial Pt/C. In conjunction with the mass activity evaluations, the specific activities to investigate the absolute value of the electrocatalyst intrinsic activity of PtNiV-OA/C and PtNiV/C display ~3 and 3-fold activity enhancement, respectively, to that of the commercial Pt/C electrocatalysts.

4.5.4 Durability Measurements

The cyclic voltamograms (Fig. 4.33(**a**)) and CO stripping voltammograms (Fig. 4.33(**b**)) after potential cycling (up to 5000 cycles) showed a decrease in ECSA. The $ECSA_{Hupd}$ loss calculated after 5000 potential cycles (as a percentage of the initial value) was as follows: PtNiV/C (66%) and PtNiV-OA/C (26%). The decline in CO current peaks and a slight positive shift from lower to higher potentials is possibly due to NiV/NiV oxide disintegration, leading to less CO tolerance of the nanoparticles, and the appearance of insignificant double peaks with increasing potential cycling (Fig. 4.33(**b**)). The slight shift of the peak positions from lower to higher potentials is due to the restricted surface movement of the large nature of the particles during prolonged potential cycling. After 5000 potential cycles, the ternary alloys showed a significant decrease in the ORR activity, with the polarization curves shifting from higher (positive) to lower (negative) potentials (Fig. 4.33(**c**)).

In terms of area-specific activity the catalysts presented here still show ~2.4 (PtNiV/C) and 1.13 (PtNiV-OA/C) improvement factor while in terms of mass-specific activity, PtNiV/C and PtNiV-OA/C still display ~1.2 and 1.5 better performance, respectively, compared with pure Pt/C (Figs. 4.33(**e**)-(**f**)). The latter results again suggest the loss of the alloying elements, Ni and V.

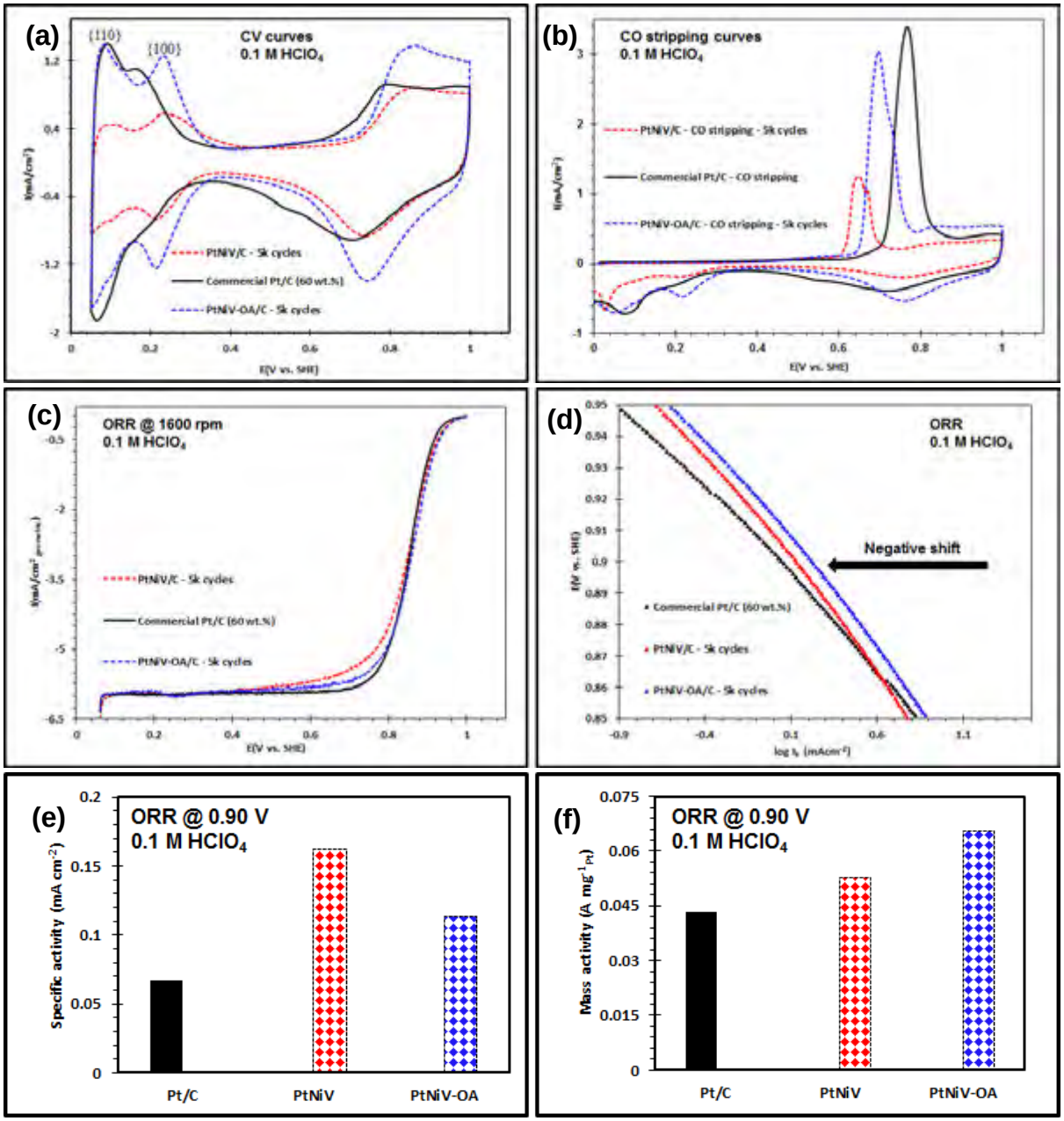

Figure 4.33: (**a**) Cyclic voltammograms of ternary Pt-based alloys PtNiV/C (red) and PtNi-OA/C (blue) (**b**) CO-stripping voltammograms, (**c**) ORR polarization curves, (**d**) the corresponding Tafel plots, (**e**) intrinsic area-specific activities and (**f**) mass-specific activities at +0.9 V after 5000 potential cycles, respectively. Durability measurements for the commercial Pt/C electrocatalysts were not conducted.

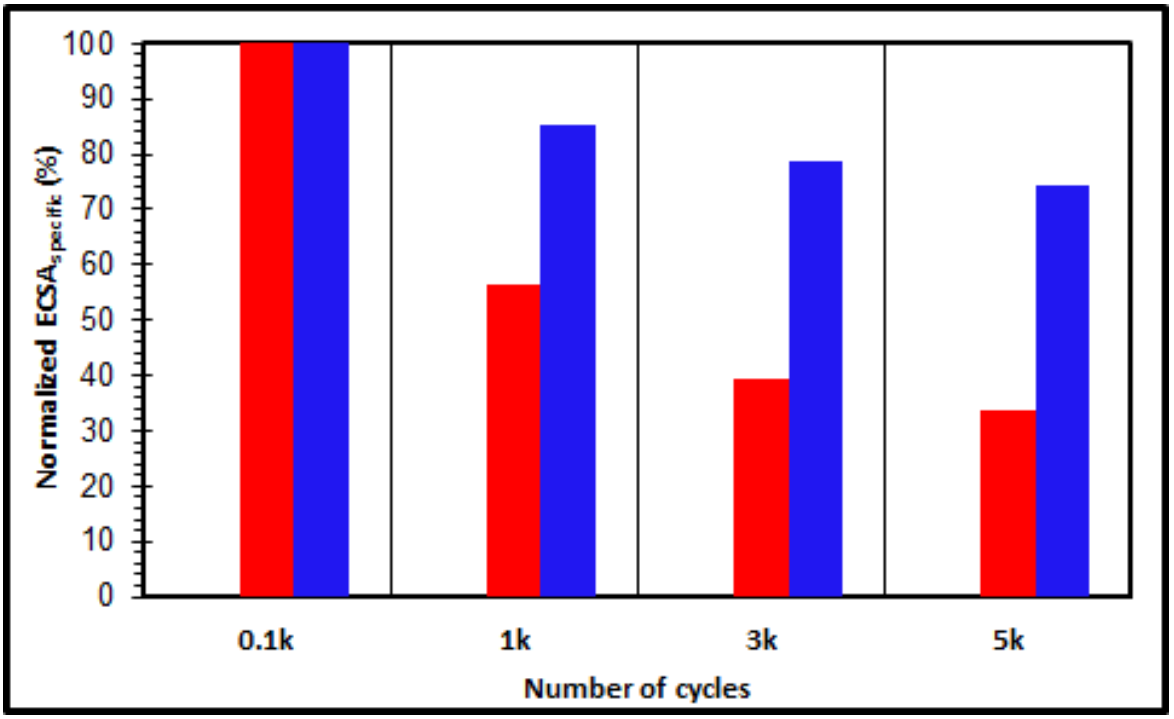

Figure 4.34: ECSA decay as a function of the continual potential cycling (up to 5000 cycles) of PtNiV/C (red) and PtNiV-OA/C (blue) nanoparticles.

Figure 4.34 shows the decay of $ECSA_{Hupd}$ of the ternary nanoparticles with prolonged potential cycling. The $ECSA_{Hupd}$ loss could arise from any of the following: NiV/NiV oxide dissolution; metal alloy oxide formation as a result of potential cycling and morphological transformations[293, 324, 325]. HAADF-STEM and STEM-EDS elemental mapping analysis were not conducted on these ternary nanoparticles post 5000 potential cycles.

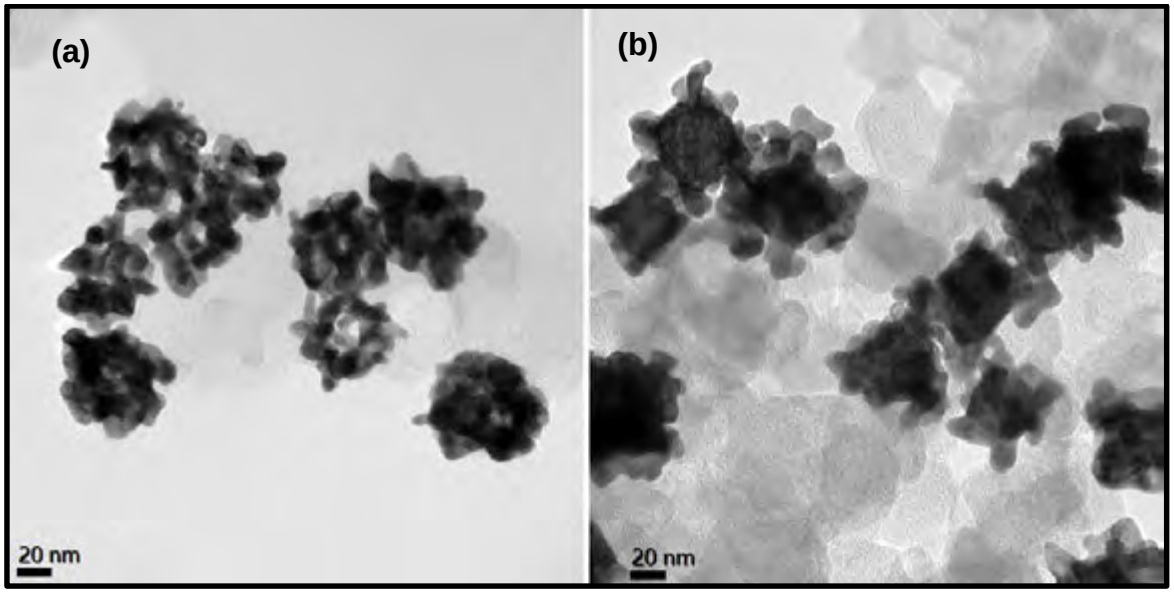

Figure 4.35: STEM micrographs of (**a**) PtNiV/C and (**b**) PtNiV-OA/C nanoparticles, post 5000 potential cycles of durability investigations.

Figure 4.35 shows TEM micrographs of the surface-deformed nanoparticles. PtNiV/C shows a significant morphological deformation and the evolution of more voids where Ni/Ni oxides were located within the individual nanoparticles compared with the PtNiV-OA/C electrocatalysts. The apparent morphological deformity of the PtNiV/C is evidenced by the large $ECSA_{Hupd}$ decay of 66% after 5000 potential cycles, indicating enormous loss of Ni/Ni oxide from the alloys and formation of apparent voids (Fig. 4.35(**a**)). The PtNiV-OA/C showed a 26% loss in $ECSA_{Hupd}$ and this can be attributed to minimal NiV/NiV oxide gradual leaching but rather the prominent decay of the outer surface layer of the nanoparticles (Fig. 4.35(**b**)).

Table 4.13: Summarizes the comparisons of the methods, morphology, particle size diameter, $ECSA_{Hupd}$, $ECSA_{CO}$, $ECSA_{CO}/ECSA_{Hupd}$, mass-specific and area-specific activities at 0.9 V of ternary nanoparticles.

Nanoalloys	Nanoalloy shapes	Particle diameter (nm)	ECSA (m^2/g_{Pt}) (CV)	ECSA (m^2/g_{Pt}) loss (%)	ECSA (m^2/g_{Pt}) (CO stripping)	ECSA (m^2/g_{Pt}) (CO stripping) loss (%)	Mass activity (A/mg_{Pt})	Mass activity loss (%)	Specific activity (mA/cm^2_{Pt})	Specific activity loss (%)
PtNiV/C (60 wt.%)	Multi-layered Ni-PtV	69.5 ± 5.4	0.1K Cycles: 115.6	66	0.1K Cycles: 111.1	74	0.196	73	0.20	20
			5K Cycles: 38.9		5K Cycles: 29.1		0.053		0.16	
PtNiV-OA/C (60 wt.%)	PtV-decorated Ni cubes	75.4 ± 4.5	0.1K Cycles: 140.1	26	0.1K Cycles: 148.7	32	0.23	72	0.20	43
			5K Cycles: 104.3		5K Cycles: 101		0.065		0.075	
Commercial Pt/C (60 wt.%)	Spherical	7.3 ± 4.2	0.1K cycles: 38.8		0.1K cycles: 85.1	-	0.030	-	0.075	-

The formulated sequential synthetic protocol resulted in the formation of multi-layered and decorated cuboidal Ni-PtV nanoparticles. These shape-orientated and multi-faceted Ni-PtV/C displayed excellent functionalities compared with the commercially available Pt/C electrocatalysts. The preliminary durability measurements showed activity decay comparable to the initial commercial Pt/C electrocatalyst measurements, suggesting NiV/NiV oxide dissolution and shape deformation. There is no obvious particle coalescence. The reported novel synthetic strategy for shape-dependent Ni-PtV core-shell nanoparticles for high performance ORR has the potential for high-yield particle synthesis, with considerable scope for further improvements to performance and durability.

CHAPTER 5 DISCUSSION

This chapter compares and discusses results from experimental investigations of different Pt-based alloy nanoparticles, synthesized using a range of protocols. The catalytic activity of these nanoparticles is seen to be dependent on their structure; their structure is in turn dependent on synthesis. The results of this study show that the performance of nanoparticles is sensitively dependent on their synthesis.

Consideration of the nanoparticle structures observed in this study shows that both the alloy system and the precursor salts used in synthesis, determine structure: i.e. the same reduction protocol, used to synthesize nanoparticles from different precursor salts, can produce different structure. Section 5.1 considers the synthesis parameters: the effect of precursor salts and their solvents selected in this work; the surfactants, and temperature. Section 5.2 then considers the reduction protocols, separately for different alloy nanoparticles and precursor salts. Finally section 5.3 considers the effect of structure on the catalytic performance of nanoparticles.

5.1 The Effect of Synthesis Parameters on Nanoparticle Structure

All nanoparticles in this work were prepared by solution-based synthetic methods. These are effective for the preparation of nanoparticles with well-controlled properties including composition, alloy structure (mixed or core-shell), size, and surface facets. The latter is particularly important since the functionality of catalysts is determined by the exposed crystal facets.

5.1.1 The Precursor Salts and Solvents

Unlike Pt, solute metals **M** (**M** = Ni, Co, V) have a low reduction potential and are susceptible to oxidation. The reduction of the **M** ions (metal precursor salts) to metal $\mathbf{M}^0$ can be achieved at elevated temperatures, provided that oxidation can be avoided. The reduction of **M** precursor salts together with Pt in a one-pot reaction is thus optimal in a water-free environment (to avoid oxidation) at elevated temperatures (to aid reduction). Solution of metal salts in high boiling point solvents was accordingly adopted. Some organic and high boiling point liquid surfactants such as oleylamine (OAm), oleic acid (OLEA) and oleyl alcohol (OA) were also used to serve as the solvents. In addition, all the metal precursor salts were selected on the basis of their

complete solubility in either long chain surfactants (amines, fatty acids and alcohols), solvents (1-OD and BE) and/or both. Table 5.1 shows the metal precursor salts, together with high boiling point solvents in which the salts were dissolved, selected for this work.

Table 5.1: Solubility of Pt and M metal salts in different organic solvents and surfactants.

Metal precursor salts[a]	**Organic solvents**[b]
$Pt(acac)_2$	1-OD, OAm, OLEA, BE, OA
H_2PtCl_6 (8 wt.% in water) (dried)	1-OD, OAm, BE, OA
$Ni(OAc)_2 \cdot 2\ H_2O$	1-OD, OAm, BE
$Co(OAc)_2 \cdot 4\ H_2O$	1-OD, OAm, BE
$V(acac)_3$	1-OD, OAm, OLEA, BE, OA

[a]$Pt(acac)_2$ = platinum (II) acetylacetonate; H_2PtCl_6 = chloroplatinic acid solution (8 wt.% in water); $Ni(OAc)_2 \cdot 2\ H_2O$ = nickel (II) acetate; $Co(OAc)_2 \cdot 4\ H_2O$ = cobalt (II) acetate; $V(acac)_3$ = vanadium (III) acetylacetonate; [b]OAm = oleylamine; 1-OD = 1-octadecene; BE = benzyl ether; OLEA = oleic acid; OA = oleyl alcohol

Heating a reaction solution of the solvent/solutes shown, to temperatures as high as 310 ºC for at least one hour, resulted in the synthesis of high quality monodisperse alloy nanoparticles, both mixed and core-shell.

5.1.2 The Surfactants

In order to achieve well-defined nanoparticles, metal precursor salts were mixed with surfactants before dissolving them in the same solvent. Generally, surfactants serve to regulate particle crystal growth by adhering reversibly to the growing crystal surfaces of nanoparticles to form a protective layer of molecules that mediates particle growth, forms stable colloids and minimizes the degree of oxidation of the particles during and after synthesis[27, 71, 73, 98, 174-181]. The origin and evolution of well-defined anisotropic nanostructures from solution grown synthetic approaches is convoluted and governed by the thermodynamic and kinetic parameters which dictate the nucleation and growth of crystallographic surface facets.

The driving mechanisms for anisotropic morphological development during crystal growth is generally believed to depend on the nature and strength of the surfactants used to stabilize the nanostructures in a wet chemical synthetic system. In most cases, the employment of a homogeneous mixture of two or more surfactants can direct and dictate anisotropic growth on specific metal surfaces as a result of preferential/selective binding/adsorption on different growing crystal facets. Crystal growth is restricted where surfactants adsorb strongly on certain crystal planes, encouraging crystal growth on weakly surfactant-bound metal surfaces and

hence leading to the creation of crystallographically facet-orientated nanostructures with surface defects.

In this project, nanoparticles with anisotropic morphology and faceted surfaces were synthesized by using a combination of two or more surfactants, to facilitate growth of more than one type of crystal facet. The on-and-off exchange of surfactants on the growing crystal surfaces allows the growth of nanocrystals in different orientations, whereby crystal growth is restricted on the crystal planes tightly bound by the surfactants and facilitated on the crystal planes where the surfactant-binding is feeble. These surfactants, which included oleylamine (OAm), octadecylamine (ODA), oleic acid (OLEA), dioctylamine (DOA), trioctylamine (TOA) and oleyl alcohol (OA), were chosen on the basis of their degree of solubility in high boiling point solvents BE and 1-OD and/or both. OAm was used in all experiments as it served to completely dissolve the metal precursor salts which were neither soluble in organic solvents nor in other surfactats (ODA, OLEA, DOA, TOA and OA).

The nature and binding strength of the surfactants on the growing crystals is different. The study of the effect of OAm and ODA was not conducted, but the addition of the third surfactant resulted in the formation of anisotropic, and two different types of, morphologies for PtNi-TOA and PtNi-DOA nanostructures (For instance, Section 4.1). It was, however, difficult to draw solid conclusions on the basis of the STEM results and correlate the role of the third surfactant on morphological- and compositional-evolutions. In the tables that follow, where more than two surfactants were used, the third surfactant is shown together with the nanoparticle composition (e.g. PtNi-OLEA).

5.1.3 The Reductants

In addition to thermal reduction protocols, synthetic protocols using chemical reductants were evaluated. Depending on the nature and reducing power of the reductant, nanoparticle growth may require aging of the reaction mixture until a desired particle size is reached. Mild reductants can thus require prolonged reaction times to complete the reduction of metal ions[52, 328]. Metal alloys of Pt and **M** present particular difficulties for reduction, requiring careful manipulation of the experimental conditions. Pt has a high standard reduction potential and its precursor salts reduce easily to Pt^0, requiring minimal control over the reaction conditions and reduction temperatures. In contrast, **M** precursor salts are difficult to reduce to $\mathbf{M}^0$ owing to

their lower reduction potentials and low stability against oxidation. To synthesize alloy nanoparticles from Pt and **M** ions, the use of powerful reductants such as TBAB to reduce metal ions with negative reduction potentials is necessary, in order to reduce two or more different metal precursor salts at similar rates. In this work, an effective approach was found to be a combination of strong reductants and an elevated reduction temperature, to reduce two or more different kinds of metal ions. This resulted in the formation of monodisperse nanoparticles with a range of morphologies and a narrow size distributions.

5.1.4 The Precursor-to-Surfactant Ratio

The metal precursor-to-surfactant ratio determines the size, morphology and size distribution of the nanoparticles. The lower the ratio of precursor-to-surfactant, the smaller the nuclei and as a result smaller nanoparticles are likely to form. The final particle size is however ultimately determined by the termination of particle growth (removing the colloidal solution from the heat source). During thermal reduction (heating the solution mixture to temperatures as high as 310 ºC), increasing the heating rate of the reaction mixtures can produce nanoparticles with smaller dimensions due to rapid formation of many nuclei, followed by fast crystal growth. The mean particle diameter can be increased with time, as the concentration of the particles in the solution drops. The correct ratio of precursor-to-surfactant precludes agglomeration and mediates particle growth during synthesis. A low precursor-to-surfactant ratio is seen to yield nanoparticles with small size and narrow size distribution.

5.1.5 The Temperature

In the present work, elevated temperatures were used in synthesis, because increasing the temperature of the reaction mixture has the beneficial effect of (a) ensuring that the chemical mixture remains homogeneous and (b) increasing the kinetics of the reduction of metal ions. Heating the mixtures to temperatures as high as 150 ºC with vigorous stirring ensured complete formation of homogeneous mixtures (i.e. no precipitates were observed). In most cases here, the nanoparticles were directly solution-grown by thermal reduction (did not require the use of chemical reductants) at temperatures determined by the boiling points of the solvents. The boiling point of solvents such 1-octadecene (1-OD, 315 ºC) and benzyl ether (BE, 297 ºC) determined the reduction temperature.

The degree of binding of the surfactants on the growing nanoparticle crystal surfaces is strongly dependent on the reduction temperature[52, 328]. Although increasing the reaction temperature improves the degree of reduction of the metal ion-surfactant complexes, hence favouring the nucleation and growth of the nanoparticles, overly high temperatures can lead to uncontrollable growth. Therefore the temperature range 200 °C – 310 °C was identified and selected, in order to avoid destabilizing the adhesion of surfactants to growing crystal surfaces. The thermal reduction of Pt precursor salts together with the precursors of highly reactive metals, was accordingly carried out by heating the reaction mixture to between 200 °C and 310 °C. Where chemical reductants were also used, the metal precursor-surfactant solution was heated to 300 °C – 310 °C in order to accelerate the reduction kinetics. This temperature range was selected as it is not sufficiently high to induce reduction prior to the introduction of the selected reductant into the solution.

Particle size range is influenced by heating rate and reaction time of the chemical reaction mixtures. Heating of the chemical reaction solution to high temperatures can result in rapid thermal reduction of the metal ion-surfactant complexes, consequently yielding concentrated nuclei in the reaction mixture. This is followed by fast crystal growth which favours the creation of particles with small dimensions, observed in the present work.

5.2 The Effect of Reduction Methods on Structure

Two reduction approaches were used in this project to circumvent the separate nucleation and growth of different metals: (a) thermal reduction (thermolysis) at high temperatures to induce the reduction of metal ions, and (b) the use of chemical reductants at elevated temperature. These synthetic approaches were successful in the preparation of well-defined nanoparticles. Table 5.2 summarises the outcome of these two reduction protocols. Where a third surfactant was added, the resultant alloys are distinguished and labelled with third surfactant. The following subsections show that, for a given alloy system and reduction protocol, the third surfactant has a significant effect on morphology.

Table 5.2: Summary of the sizes, morphologies and structures of the as-synthesized nanoparticles synthesized using reduction methods co-reduction (CR) and sequential reduction (SR).

Metal alloys	Methods[a]	Sizes (nm)	Morphologies[b]	Structures
PtNi-OLEA	CR	17.6 ± 1.9	C, T	Core-shell Ni-Pt
PtNi-TOA	CR	24.5 ± 2.5, C 53.9 ± 3.6, EP	C, EP	Core-shell Ni-Pt
PtNi-DOA	CR	19.9 ± 4.0, C 38.4 ± 4.1, EP	C, EP	Core-shell Ni-Pt
PtNi-OLEA	SR	32.9 ± 2.8	C, PI	Core-shell Ni-Pt
PtNi-TOA	SR	16.7 ± 1.8	C, EI	Core-shell Ni-Pt
PtNi-DOA	SR	26.6 ± 2.1	H, EP	Core-shell Ni-Pt
PtNi-OLEA	CR	18.3 ± 1.7	SS, EP	Mixed Pt_3Ni
PtNi-TOA	CR	15.6 ± 1.1	CO, EP	Mixed Pt_3Ni
PtNi	CR	63 ± 5.4	D	Mixed Pt_3Ni
PtCo	CR	73 ± 8.8	D	Mixed Pt_3Co
Pt(NiCo)	CR	59 ± 7.1	D	Mixed $Pt_3(NiCo)$
PtNiV	SR	69.5 ± 5.4	M-L	Core-shell Ni-VPt
PtNiV-OA	SR	75.4 ± 4.5	D-Ni	Core-shell Ni-VPt

[a]CR = co-reduction; SR = sequential reduction; [b]SS = star-shaped; EP = elongated polyhedral; S = spherical; C = cubic; PI = porous irregular; EI = elongated irregular; H = hexagonal; T = triangular; D = dendritic; M-L = multi-layered; D-Ni = decorated Ni

5.2.1 Co-Reduction by Thermolysis: PtNi Binary Nanoparticles

The reduction of two different metal precursor salts in a suitable solvent is the most common method for synthesizing bimetallic nanoparticles [25, 26, 73, 98]. PtNi nanoparticles were first synthesized by thermally co-reducing metal precursor salts in the presence of three different types of surfactants, as shown in Table 5.3. The influence of the third surfactant, with all other factors held constant, on the final morphology of the nanoparticles is seen to be significant. This novel preparative protocol, developed in the present work, yielded high quality and monodisperse nanoparticles, exhibiting excellent dispersion and crystallinity.

Table 5.3: PtNi nanoparticles, co-reduced by thermolysis: the influence of surfactant on morphology.

Alloys	Surfactant(s)	Reduction Mechanism(s)	Conditions	Morphologies
PtNi-OLEA	OAm + ODA + OLEA	Co-reduction by thermolysis	240 °C, 30 – 40 min	C, T
PtNi-TOA	OAm + ODA + TOA	Co-reduction by thermolysis	240 °C, 30 – 40 min	C, EP
PtNi-DOA	OAm + ODA + DOA	Co-reduction by thermolysis	240 °C, 30 – 40 min	C, EP

OAm = oleylamine; ODA = octadecylamine; OLEA = oleic acid; TOA = trioctylamine; DOA = dioctylamine; C = cubic; T = triangular; EP = elongated polyhedral

5.2.2 Sequential Reduction by Thermolysis: PtNi Binary Nanoparticles

Sequential- or seeded-growth is one of the most widely used wet-chemical strategies to prepare core-shell nanoparticles[25, 26, 67, 140-145]. PtNi nanoparticles were synthesized by this reduction mechanism, to coat the more reactive, less expensive Ni metal with Pt. A high-temperature sequential thermal reduction approach yielded nanoparticles with morphologies which varied according to the third surfactant type as seen in 5.4 (a) above; again all nanoparticles were highly monodisperse with a high degree of crystallinity. In this case however, nanoparticles exhibited a Ni-rich core and a (~2-nm) Pt-rich shell.

Table 5.4: PtNi nanoparticles, sequentially reduced by thermolysis: the influence of surfactant on morphology.

Alloys	Surfactant(s)	Reduction Mechanism(s)	Conditions	Morphologies
PtNi-OLEA	OAm + ODA + OLEA	Sequential reduction by thermolysis	240 °C, 30 – 40 min	PI, C
PtNi-TOA	OAm + ODA + TOA	Sequential reduction by thermolysis	240 °C, 30 – 40 min	EI, C
PtNi-DOA	OAm + ODA + DOA	Sequential reduction by thermolysis	240 °C, 30 – 40 min	S

OAm = oleylamine; ODA = octadecylamine; OLEA = oleic acid; TOA = trioctylamine; DOA = dioctylamine; PE = porous irregular; C = cubic; EI = elongated irregular; S = spherical

5.2.3 Co-Reduction by Reductant: PtNi Binary Nanoparticles

In order to reduce two different metal ions at a similar rate, TBAB was introduced as a chemical reductant, at elevated temperature as shown in Table 5.5. The only additional variable was the third surfactants used: as seen above, this affected the morphology of the final synthesized nanoparticle.

Table 5.5: PtNi nanoparticles, co-reduced by reductant: the influence of surfactant on morphology.

Alloys	Surfactant(s)	Reduction Mechanism(s)	Conditions	Morphologies
PtNi-OLEA	OAm + ODA + OLEA	Co-reduction by reductant	240 °C, 30 – 40 min	SS, EP
PtNi-TOA	OAm + ODA + TOA	Co-reduction by reductant	240 °C, 30 – 40 min	CO, EP

OAm = oleylamine; ODA = octadecylamine; OLEA = oleic acid; TOA = trioctylamine; SS = star-shaped; EP = elongated polyhedral; CO = cuboctahedra

5.2.4 Co-reduction by Thermolysis: Binary (PtNi and PtCo) and Ternary (PtNiCo) Nanoparticles

Pt-based binary (PtNi and PtCo) and ternary (PtNiCo) nanoparticles of dendritic morphology were successfully prepared by thermal co-reduction as shown in Table 5.6. In this case, surfactants are constant; and a dendritic morphology is achieved for three different alloy nanoparticle types. These nanoparticles show a broad particle size distribution, good dispersion and good crystallinity; and can be synthesized in a short period of time (15 – 20 minutes) at 300 ºC. Individual particles show varied branch lengths and widths. Although the degree of branching may be dependent on the concentration of the precursors in the reaction mixture, the growth kinetics of nanoparticles is directed by the surfactants. The dendritic nanoparticles are all seen to exhibit a homogeneous atomic distribution of Pt and the alloying elements (Ni and/or Co), suggesting the formation of homogeneously mixed solid solution phases.

Table 5.6: PtNi, PtCo and PtNiCo nanoparticles co-reduced by thermolysis, exhibiting a dendritic morphology.

Alloys	Surfactant(s)	Reduction Mechanism(s)	Conditions	Morphology
PtNi	OAm + TOA + OLEA	Co-reduction by thermolysis	300 °C, 15 – 20 min	D
PtCo	OAm + TOA + OLEA	Co-reduction by thermolysis	300 °C, 15 – 20 min	D
PtNiCo	OAm + TOA + OLEA	Co-reduction by thermolysis	300 °C, 15 – 20 min	D

OAm = oleylamine; TOA = trioctylamine; OLEA = oleic acid; D = dendritic

5.2.5 Sequential Reduction by Thermolysis: PtNiV Ternary Nanoparticles

Sequential thermolysis was used to develop V-NiPt core-shell nanoparticles by thermally reducing V metal ions to V^0 metal/metal oxide to serve as preformed overgrowth seeds, followed by thermal reduction of a mixture of Pt and Ni salts. Highly complex monodisperse nanoparticles, anisotropic and polycrystalline, with a broad size range, were successfully

synthesized. The presence of a third surfactant (OA) results in a change in morphology as shown in Table 5.7.

PtNiV nanoparticles prepared with OAm and ODA only, show a multi-layered shell and a core metal/metal oxide; whereas PtNiV-OA nanoparticles synthesized with the addition of OA, exhibit a core-decorated structure. In both cases, different nanoparticles of fcc phases with variable compositions were observed in nanoparticles. These nanoparticles were of a near spherical, cubic Ni-rich core decorated with a homogeneous solid solution of polycrystalline binary PtV-rich shell, suggesting that the final structures are core-shell Ni-PtV structures. The evolution of these multi-facet crystals suggests Ni salts were reduced first and acted as the basis for the epitaxial overgrowth at different crystal surface sites.

Table 5.7: PtNiV nanoparticles, sequentially reduced by thermolysis, showing the effect of OA addition on morphology.

Alloys	Surfactant(s)	Reduction Mechanism(s)	Conditions	Morphologies
PtNiV	OAm + ODA	Sequential reduction by thermolysis	310 °C, 30 – 40 min	M-L
PtNiV-OA	OAm + ODA + OA	Sequential reduction by thermolysis	310 °C, 30 – 40 min	D-Ni

OAm = oleylamine; ODA = octadecylamine; OA = oleyl alcohol; M-L = multi-layered; D-Ni = decorated cubic Ni.

5.3 The Effect of Size, Composition and Morphology on Catalytic Activity

The aim of this research was the design and synthesis of cost-effective Pt-based electrocatalysts with enhanced electro-activity for the oxygen reduction reaction (ORR) in fuel cells. In this section, the relationship between synthesis, structure and catalytic properties of the as-synthesized nanoparticles is considered. A wide range of high quality Pt-based nanoparticles (containing Ni, Co and V) of different morphology, surface structures, composition and size, were successfully synthesized by systematic manipulation of the synthesis conditions. The key factors that influenced the functionality of binary and ternary nanoparticles are (a) size, (b) composition and (c) surface morphology.

5.3.1 Size

A decrease in size is generally expected to result in an increase in catalytic activity as a result of this increased surface area, which provides more access for the reactants to more exposed atoms on the nanoparticle surface[67-70]. The latter effect is limited as particles smaller than a certain size do not exhibit properly developed surfaces anymore. The nanoparticles synthesized in the present work, however, were of highly anisotropic morphologies. The surface area is accordingly not always a function of size. The results in this work show that although catalytic activity is highest for nanoparticles less than 25 nm in size, catalytic activity for particles up to 75 nm is still several times greater than commercial Pt catalysts (< 10 nm in diameter). Although the size effect of alloy nanoparticles is complicated by the distribution of two or more metal atoms compared with monometallic nanoparticles, all the synthesized binary and ternary nanoparticles in this work, regardless of their larger dimensions, exhibited high surface area and functionality.

5.3.2 Composition

The incorporation of a second and third metal modifies the original surface properties of a Pt nanoparticle catalyst and hence its catalytic behaviour[40-44]. Overall, the addition of one or more highly reactive metal to Pt, to form mixed or core-shell alloy nanoparticles, was observed to enhance catalytic performance of the nanoparticles synthesized in this work.

In the current findings, nanoparticles that showed a Ni-rich core and a (~2-nm) Pt-rich shell, including Pt_3Ni, exhibited outstanding catalytic performance, and also the formation of more prominent oxide peaks in CV curves. This suggests a relationship between higher current density as a result of the particle oxide formation, and superior catalytic activity for the ORR. In this regard, it can be deduced that the shell thickness layer also plays a key role in determining the activity performance of the core-shell nanoparticles. It is therefore the central region (core) element that modifies the electronic properties of the shell/surface Pt. The alloying composition was observed not only to be associated with anisotropic growth and improved functionality of catalysts, but also to enhance tolerance to CO poisoning.

5.3.3 Surface Morphology

The key structural property of nanoparticles for enhanced catalytic activity is the surface morphology, because catalytic reactions take place on the catalyst surface[23, 24]. In this work, a range of faceted nanoparticles of hollow/porous structures, core-shell structures, mixed alloy structures and hyper-branched structures was synthesized. These morphologies exhibited surface sites such as multiple edges, corners, steps and interconnected branches; these provide high degree of accessibility of reacting molecules to the surface structure, rendering them the best nanocatalysts for the ORR Thus, optimal catalytic efficiency of electrocatalysts is surface-morphology dependent.

5.3.4 Summary

Dissolving precursor salts, together with a mixture of selected surfactants, in high boiling-point solvents allowed reduction to take place at elevated temperatures. These elevated temperatures, together with powerful reductants, led to the synthesis of nanoparticles with anisotropic morphology and high surface area. Agglomeration of particles can be avoided by selecting a low ratio precursor to surfactant. Among the synthesized nanoparticles, small size was associated with high catalytic activity. In comparison with commercial Pt catalysts however, even the largest synthesized nanoparticles provided good catalytic performance. This is attributed both to the addition of other elements to form alloys; and to the anisotropic morphology which allowed a high, faceted surface to be exposed for catalysis.

CHAPTER 6 CONCLUSIONS AND RECOMMENDATIONS

The work presented in this thesis, is an evaluation of the following hypothesis: Pt-based nanoalloys, containing around 75 at.% platinum and having high surface area with anisotropic morphology, will exhibit improved catalytic activity, and reduced need for Pt, in PEMFCs compared to standard Pt catalysts.

A systematic investigation of some novel high temperature, wet-chemical synthetic approaches for the fabrication of Pt-based alloy nanoparticles, was accordingly carried out. Nanoparticles were successfully synthesized which contained around 75 at.% platinum, with nickel (Ni), cobalt (Co) or vanadium (V). These nanoparticles were either mixed alloys, or core-shell alloys, with a high surface area and anisotropic morphology. Their composition, structure and catalytic activity are shown in Table 6.1. The synthesized alloys consistently exhibited superior activity, relative to the catalytic activity of standard Pt nanoparticles.

From these results, we can conclude the following:

1. Novel high temperature wet-chemical synthetic methods were successfully designed to systematically prepare both mixed and core-shell Pt-based nanoparticles containing Ni, Co and V.

2. A range of anisotropic morphologies of nanoparticles were obtained by using different synthetic routes, metal precursor salts, surfactants and reductants, in different high boiling point solvents.

3. All the synthesized nanoparticles with composition around 75 at.% Pt, exhibit improved catalytic activity relative to a standard commercial Pt/C electrocatalysts.

4. Core-shell ternary nanoparticles (PtNiV and PtNiV-OA) exhibit better mass-specific activities than $Pt_3(NiCo)$.

5. Catalytic activity consistently decreases from low to high metal loadings (wt.%). *Considering only the nanoparticles with the lowest loadings (20 wt.%).*

6. Alloyed nanoparticles have a higher catalytic activity than core-shell nanoparticles.

7. Pt_3Ni nanoparticles with SS/EP or C/EP morphologies, and hence high-area faceted surfaces, display enhanced catalytic performance.

Table 6.1: Alloys of different metal loadings, structure, morphologies, area-specific activities, mass-specific activities and improvement factors.

Alloys and metal loadings (%)	**Structure**	**Morphology**	**I_s (mA/cm^2_{Pt})**	**I_F (I_s)**	**I_m (A/mg_{Pt})**	**I_F (I_m)**
Pt_3Ni-OLEA/C (20 wt.%)	Alloyed	SS, EP	0.52	~ 10	0.65	~ 18
Pt_3Ni-TOA/C (20 wt.%)	Alloyed	CO, EP	0.46	~ 9	0.75	~ 20
Pt/C (20 wt.%)		S	0.052	-	0.037	-
PtNi-OLEA/C (20 wt.%)	Core-shell	C, PI	0.41	~ 8	0.46	~ 12
PtNi-TOA/C (20 wt.%)	Core-shell	C, EI	0.42	~ 8	0.57	~ 14
PtNi-DOA/C (20 wt.%)	Core-shell	H, EP	0.30	~ 6	0.47	~ 13
Pt/C (20 wt.%)		S	0.052	-	0.037	-
PtNi-OLEA/C (40 wt.%)	Core-shell	C, T	0.39	~ 7	0.36	~ 4
PtNi-TOA/C (40 wt.%)	Core-shell	C, EP	0.51	~ 9	0.28	~ 3.3
PtNi-DOA/C (40 wt.%)	Core-shell	C, EP	0.37	~ 6	0.31	~ 3
Pt/C (40 wt.%)		S	0.093	-	0.057	-
Pt_3Ni/C (60 wt.%)	Alloyed	D	0.24	~ 8	0.14	~ 1.9
Pt_3Co/C (60 wt.%)	Alloyed	D	0.21	~ 7	0.11	~ 1.5
$Pt_3(NiCo)$/C (60 wt.%)	Alloyed	D	0.20	~ 6.7	0.15	~ 2
Pt/C (60 wt.%)		S	0.030	-	0.075	-
PtVNi/C (60 wt.%)	Core-shell	M-L	0.20	~ 7	0.20	~ 2.7
PtVNi-OA/C (60 wt.%)	Core-shell	D-Ni	0.20	~ 7	0.23	~ 3.1
Pt/C (60 wt.%)		S	0.030	-	0.075	-

SS = star-shaped; EP = elongated polyhedral; S = spherical; C = cubic; PI = porous irregular; EI = elongated irregular; H = hexagonal; T = triangular; D = dendritic; M-L = multi-layered; D-Ni = decorated Ni; I_s = area-specific activity; I_m = mass-specific activity; I_F = improvement factor

Durability measurements show that after prolonged cycling, the synthesized nanoparticles exhibit a decrease in surface area (relative to volume), catalytic activity and CO tolerance. In all cases, the catalytic activity after prolonged cycling remained similar to (or greater than) that

of commercial Pt/C nanoparticles after short-to medium-term cycling. In other words, prolonged cycling reduced the catalytic activity to that of Pt after medium cycling.

This research work has accordingly developed and tested protocols for synthesis of nanoparticles which are outstanding catalysts. Three areas are recommended for further work:

- The coating thickness of the as-synthesized core-shell (particularly Ni-Pt) nanoparticles showed a rich Ni-core and a (~2-nm) Pt-rich shell. The thickness of the Pt-shell can be increased by increasing the ratio of Pt-to-Ni precursor salts by orders of magnitude. **It is therefore recommended to investigate the effect of both sequential and co-reduction synthetic approaches on the evolution of Pt shell thickness on Ni-core and evaluate the influence of shell thickness on the catalytic activity.**

- The nature of the support determines the interaction of the nanoparticles with the support. This can, in turn, affect the electrochemical results. In the present study, carbon black (Vulcan XC-72R, the current industry standard) was used as a support for all electrochemical testing of nanoparticles**.** It remains a good basis for comparison of nanoparticles with potential application in PEMFCs. **It is however recommended to evaluate the effect of different supports (carbon and non-carbon based) on the measured catalytic activity of synthesized nanoparticles.**

- The synthesized nanoparticles showed outstanding catalytic activity after short- to medium-term cycling; but showed some activity degradation after prolonged potential cycling. Improving the long-term lifespan of these nanoparticles will accordingly require attention. Long term durability can be achieved via heat treatments at elevated temperatures, leading to improved catalyst stability and activity. **It is therefore recommended to evaluate the effect of heat treatment, on the catalytic activity and durability/stability of the synthesized nanoparticles.**

CHAPTER 7 REFERENCES

1. Zhong, C.-J., Luo, J., Njoki, P.N., Mott, D., Wanjala, B., Loukrakpam, R., Lim, S., Wang, L., Fang, B., Xu, Z. *Energy Environ. Sci.* **1** (2008) 454 - 466.
2. Stamenkovic, V.R., Mun, B.S., Arenz, M., Mayhofer, K.J.J., Lucas, C.A., Wang, G.F., Ross, P.N., Markovic, N.M. *Nat. Mater.* **6** (2007) 241.
3. Wang, Y., Chen, K.S., Mishler, J., Cho, S.C., Adroher, X.C. *Appl. Energy* **88** (2011) 981 - 1007.
4. Zhang, J.-J., PEM Fuel Cell Electrocatalysts and Electrocatalyst Layers: *Fundamentals and Applications;* Springer, 2008.
5. Swider-Lyons, K.E., Campbell, S.A. *J. Phys. Chem. Lett.* **4** (2013) 393 - 401.
6. Debe, M.K., *Nature* **486** (2012) 43 - 49.
7. Hoogers, G., Thomsett, D. *Cat. Tech.* **3** (1999) 106.
8. Dresselhause, M.S., Thomas, I.L. *Nature* **414** (2001) 332 - 337.
9. http://www.physics.nist.gov/MajResFac/NIF/pemFuelCells.html>NIST. PEM Fuel Cells.
10. Bing, Y., Liu, H., Zhang, L., Ghosh, D., Zhang, J. *Chem. Soc. Rev.* **39** (2010) 2184 - 2202.
11. Bard, A.J., Faulkner, L.R. Electrochemical Methods: *Fundamentals and Applications;* Wiley, 2001.
12. Burda, C., Chen, X.B., Narayanan, R., El-Sayed, M.A. *Chem. Rev.* **105** (2005) 1025 - 1102.
13. Liu, Z., Ling, X.Y., Su, X., Lee, J.Y. *J. Phys. Chem.* B **108** (2004) 8234.
14. Liu, Z., Ling, X.Y., Lee, J.Y., Su,.X., Gan, L.M. *J. Mater. Chem.* **13** (2003) 3049.
15. Liu, Z., Lee, J.Y., Ling, X.Y., Chen, W., Han, M., Gan, L.M. *Langmuir* **20** (2004) 181.
16. Chen, S., Kucernak, A. *J. Phys. Chem.* B **108** (2004) 3262.
17. Anderson, M.L., Stroud, R.M., Rolison, D.R. *Nano Lett.* **2** (2002) 235.
18. Pietron, J.J., Stroud, R.M., Rolison, D.R. *Nano Lett.* **2** (2002) 235.
19. Bulushev, D.A., Yuranov, I., Suvorova, E.I., Buffat, P.A., Kiwi-Minsker, L. *J. Catal.* **224** (2004) 8.
20. Balogh, L., Tomalia, D.A. *J. Am. Chem. Soc.* **120** (1998) 7355.
21. Carrettin, S., McMorn, P., Johnston, P., Griffin, K., Kiely, C.J., Hutchings, G. *J. Chem. Chem. Phys.* **5** (2003) 1329.
22. Ralph, T.R., Hogarth, M.P. *Platinum Met. Rev.* **46** (2002) 3 - 14.
23. Libuda, J., Freund, H.-J. *Surf. Sci. Rep.* **57** (2005) 157.
24. Libuda, J., *ChemPhysChem.* **5** (2004) 625.
25. Wang, D., Li, Y. *Adv. Mater.* **23** (2011) 1044 - 1060.
26. Ferrando, R., Jellinek, J., Johnston, R.L. *Chem. Rev.* **108** (2008) 846 - 904.
27. Wu, J., Gross, A., Yang, H. *Nano Lett.* **11** (2011) 798 - 802.
28. Stamenkovic, V., Schmidt, T.J., Ross, P.N., Markovic, N.M. *J. Phys. Chem.* B **106** (2002) 11970 - 11979.
29. Paulus, U.A., Wokaun, A., Scherer, G.G., Schmidt, T.J., Stamenkovic, V., Radmilovic, V., Markovic, N.M., Ross, P.N. *J. Phys. Chem.* B **106** (2002) 4181 - 4191.
30. Wang, D.S., Peng, Q., Li, Y.D. *Nano Res.* **3** (2010) 574.
31. Kang, Y.J., Murray, C.B. *J. Am. Chem. Soc.* **132** (2010) 7568.
32. Peng, Z., Yang, H. *Nano Today* **4** (2009) 143 - 164.
33. Chen, A., Holt-Hindle, P. *Chem. Rev.* **110** (2010) 3767 - 3804.
34. Zhang, J., Yang, H., Fang, J., Zou, S. *Nano Lett.* **10** (2010) 638 - 644.
35. Kim, J., Lee, Y., Sun, S. *J. Am. Chem. Soc.* **132** (2010) 4996 - 4997.
36. Wang, L., Yamauchi, Y. *Chem. Asian J.* **5** (2010) 2493 - 2498.
37. Yuan, Q., Zhou, Z., Zhuang, J., Wang, X. *Chem. Commun.* **46** (2010) 1491 - 1493.
38. Liu, L., Scholz, R., Pippel, E., Gosele, U. *J. Mater. Chem.* **20** (2010) 5621 - 5627.
39. Huang, X., Zhang, H., Guo, C., Zhou, Z., Zheng, N. *Angew. Chem. Int. Ed.* **48** (2009) 4808 - 4812.
40. Meunier, F.C., *ACS Nano* **2** (2008) 2441 - 2444.

41. Ressler, T., Jentoft, R.E., Wienold, J., Girgsdies, F., Neisius, T., Timpe, O. *Nucl. Instr. and Meth. in Phys. Res.* B **200** (2003) 165.
42. Tao, A.R., Habas, S., Yang, P. *Small* **4** (2008) 310 - 325.
43. Dahl, J.A., Maddux, B.L.S., Hutchison, J.E. *Chem. Rev.* **107** (2007) 2228 - 2269.
44. Moshfegh, A.Z., *J. Phys. D: Appl. Phys*. **42** (2009) 233001.
45. Hwang, B.-J., Sarma, L.S., Chen, J.-M., Chen, C.-J., Shih, S.-C., Wang, G.-R., Liu, D.G., Lee, J.-F., Tang, M.-T. *J. Am. Chem. Soc.* **127** (2005) 11140 - 11145.
46. Altman, M.S., *Science* **327** (2010) 789.
47. Somorjai, G.A., *Appl. Surf. Sci.* **121**/**122** (1997) 1.
48. Tao, F., Dag, S., Wang, L.W., Liu, Z., Butcher, D.R., Bluhm, H., Salmeron, M., Somorjai, G.A. *Science* **327** (2010) 850.
49. Kamigaito, M., Ando, T., Sawamoto, M. *Chem. Rev.* **101** (2001) 3689.
50. Murray, R.W., *Chem. Rev.* **108** (2008) 2688.
51. Corma, A., Garcia, H., Xamena, F.X.L. *Chem. Rev.* **110** (2010) 4606.
52. Talapin, D.V., Lee, J.-S, Kovalenko, M.V., Shevchenko, E.V. *Chem. Rev.* **110** (2010) 389 - 458.
53. Hyeon, T., *Chem. Commun.* (2003) 927.
54. Sun, S.H., Murray, C.B., Weller, D., Folks, L., Moser, A. *Science* **287** (2000) 1989.
55. Han, J., Liu, Y., Guo, R. *J. Am. Chem. Soc.* **131** (2009) 2060.
56. Zhao, M., Crooks, R.M. *Adv. Mater.* **11** (1999) 217.
57. Aiken, J.D., Finke, R.G. *Chem. Mater.* **11** (1999) 1035.
58. Lu, P., Teranishi, T., Asakura, K., Miyake, M., Toshima, N. *J. Phys. Chem.* B **103** (1999) 9673.
59. Lewis, L.N., *Chem. Rev.* **93** (1993) 2693.
60. Shan, S., Luo, J., Yang, L., Zhong, C-J. *Catal. Sci. Technol.* **4** (2014) 3570 - 3588.
61. Thomas, J.M., Johnson, B.F., Raja, R., Sankar, G., Midgley, P.A. *Acc. Chem. Res.* **36** (2003) 20 - 30.
62. Kamat, P.V., *J. Phys. Chem.* B **106** (2002) 7729 - 7744.
63. Shibata, S.J., Hanawa, F., Nakahara, M. *Electron. Lett.* **21** (1985) 1145.
64. Shibata, S.J., *Non-Cryst. Solids* **178** (1994) 272.
65. Seker, F., Malenfant, P.R.L., Larsen, M., Alizaden, A., Conway, K., Kulkarni, A.M., Goddard, G., Garaas, R. *Adv. Mater.* **17** (2005) 1941.
66. Teng, X., Black, D., Watkins, N.J., Gao, Y., Yang, H. *Nano lett*. **3** (2003) 261 - 264.
67. Xiong, Y., Wiley, B.J., Xia, Y. *Angew. Chem. Int. Ed.* **46** (2007) 7157.
68. Guczi, L., Petõ, G., Beck, A., Pászti, Z. *Top. Catal.* **29** (2004) 129 - 138.
69. Lin, Y., Huber, G.W. *Energy Environ. Sci.* **2** (2009) 71.
70. Narayanan, R., El-Sayed, M.A. *J. Phys. Chem.* B **107** (2003) 12416 - 12424.
71. Bönnemann, H., Nagabhushana, K.S. *J. New. Mat. Electrochem. Systems* **7** (2004) 93 - 108.
72. Gopalakrishnan, J., *Chem. Mater.* **7** (1995) 1265.
73. Toshima, N., Yonezawa, T. *New J. Chem.* (1998) 1179 - 1200.
74. Moriarty, P., *Rep. Prog. Phys.* **64** (2001) 297 - 381.
75. Schmid, G., Nanoparticles: *From Theory to Application;* Wiley, 2004.
76. Rogach, A.L., Talapin, D.V., Shevchenko, E.V., Kornowski, A., Haase, M., Weller, H. *Adv. Funct. Mater.* **12** (2002) 653.
77. Yu, J., Ho, W., Lin, J., Yip, H., Wong, P. *Environ. Sci. Technol.* **37** (2003) 2296.
78. Yang, H., *Angew. Chem. Int. Ed.* **50** (2011) 2674 - 2676.
79. Lee, Y.W., Kim, M., Kim, Z.H., Han, S.W. *J. Am. Chem. Soc.* **131** (2009) 17036.
80. Lee, Y.W., Kim, M., Kim, Y., Kang, S.W., Lee, J.-H., Han, S.W. *J. Phys. Chem.* C **114** (2010) 7689.
81. Porter, N.S., Wu, H., Quan, Z., Fang, J. *Acc. Chem. Res.* **46** (2013) 1867 - 1877.
82. Kolmakov, A., Chen, X., Moskovits, M. *J. Nanosci. Nanotechnol.* **8** (2008) 111.
83. Wang, S., Xu, Q., Zhang, X., Liu, G. *Electrochem. Commun.* **10** (2008) 411.
84. Luo, X., Morrin, A., Killard, P.J., Smyth, M.R. *Electroanalysis* **18** (2006) 319.
85. Sealy, C., *Mater. Today* **11** (2008) 65 - 68.
86. Liu, X., Wang, D., Li, Y. *Nano Today* **7** (2012) 448 - 466.

87. Stamenkovic, V.R., Fowler, B., Mun, B.S., Wang, G.F., Ross, P.N., Lucas, C.A., Markovic, N.M. *Science* **315** (2007) 493 - 497.
88. Chen, C., Kang, Y., Huo, Z., Zhu, Z., Huang, W., Xin, H.L., Snyder, J.D., Li, D., Herron, J.A., Mavrikakis, M., Chi, M., More, K.L., Li, Y., Markovic, N.M., Somorjai, G.A., Yang, P., Stamenkovic, V.R. *Science* **343** (2014) 1339 - 1343.
89. Sinfelt, J.H., Bimetallic Catalysts: Wiley, 1983.
90. Szanyr, J., Anderson, S., Paffett, M.T. *J. Catal.* **149** (1994) 438.
91. Sinfelt, J.H., *Acc. Chem. Res.* **20** (1987) 134.
92. Sinfelt, J.H., *J. Catal.* **29** (1973) 308.
93. Sinfelt, J.H., *Acc. Chem. Res.* **10** (1977) 15.
94. Bertolini, J.C., Massardier, J. *Catal. Lett.* **9** (1991) 183.
95. Liu, X.Y., Wang, A.Q., Wang, X.D., Mou, C.Y., Zhang, T. *Chem. Commun.* (2008) 3187 - 3189.
96. Chen, C.-H., Sarma, L.S., Chen, J.-M., Shih, S.-C., Wang, G.-R., Liu, D.-G., Tang, M.-T., Lee, J.-F., Hwang, B.-J. *ACS Nano* **1** (2007) 115 - 124.
97. Toshima, N., Harada, M., Yonezawa, T., Kushibashi, K., Asakura, K. *J. Phys. Chem.* **95** (1991) 7448.
98. Roucoux, A., Schulz, J., Patin, H. *Chem. Rev.* **102** (2002) 3757 - 3778.
99. Habas, S.E., Lee, H., Radmilovic, V., Somorjai, P., Yang, P. *Nature Mater.* **6** (2007) 692.
100. Harada, M., Asakura, K., Ueki, Y., Toshima, N. *J. Phys. Chem.* **95** (1992) 9730.
101. Wang, Y., Liu, H. *Polym. Bull.* **25** (1991) 139.
102. Liu, H., Mao, G., Meng, S. *J. Mol. Catal.* **74** (1992) 275.
103. Eswaramoorthi, I., Lingappan, N. *Appl. Catal. A: Gen.* **319** (2003) 119.
104. Chen, J.G., Menning, C.A., Zellner, M.B. *Surf. Sci. Rep.* **63** (2008) 201 - 254.
105. Burch, R., Garla, L.C. *J. Catal.* **71** (1981) 360 - 372.
106. Enache, D.I., Edwards, J.K., Landon, P., Solsona-Espriu, B., Carley, A.F., Herzing, A.A., Watanabe, M., Kiely, C.J., Knight, D.W., Hutchings, G.J. *Science* **311** (2006) 362.
107. Bligaard, T., Nørskov, J.K., Rossmeisl, J., Christensen, C.H. *Nat. Chem.* **1** (2009) 37.
108. Nørskov, J.K., Bligaard, T., Rossmeisl, J., Christensen, C.H. *Nature Chemistry* **1** (2009) 37 - 46.
109. Nørskov, J.K., Christensen, C.H. *Science* **312** (2006) 1322.
110. Schmid, G., Lehnert, A., Malm, J.-O., Bovin, J.-O. *Angew. Chem. Int. Ed. Engl.* **30** (1991) 874.
111. Mavrikakis, M., Hammer, B., Nørskov, J.K. *Phys. Chem. Rev.* **81** (1998) 2819 - 2822.
112. Gauthier, Y., Schmid, M., Padovani, S., Lundgren, E., Bus, V., Kresse, G., Redinger, J., Varga, P. *Phys. Rew. Lett.* **120** (2001) 36103.
113. Nørskov, J.K., *Nature* **414** (2001) 405.
114. Besenbroek, F., Chorkendorff, I., Clausen, B.S., Hammer, B., Molenbroek, A.M., Nørskov, J.K. Stensgaard, I. *Science* **279** (1998) 1913.
115. Hoffmann, R., *Rev. Mod. Phys.* **60** (1988) 601 - 628.
116. Liu, P., Nørskov, J.K. *Phys. Chem. Chem. Phys.* **3** (2001) 3814 - 3818.
117. Hammer, B., Nørskov, J.K. *Adv. Catal.* **45** (2000) 71 - 129.
118. Stassi, A., D'Urso, C., Baglio, V. Di Blasi, A., Antonucci, V., Arico, A.S., Castro Luna, A.M., Bonesi, A., Triaca, W.E. *J. Appl. Electrochem.* **36** (2006) 1143 - 1149.
119. Bagotsky, V.S., Fundamentals of Electrochemistry: Wiley, 2006.
120. Serov, A., Kwak, C. *Appl. Catal.* B **90** (2009) 313 - 320.
121. Taufany, F., Pan, C.-J., Chou, H.-L., Rick, J., Chen, Y.-S., Liu, D.-G., Lee, J.-F., Tang, M.-T., Hwang, B.-J. *Chem. Eur. J.* **17** (2011) 10724 - 10734.
122. Antolini, E., *Mater. Rev. and Phys.* **78** (2003) 563 - 573.
123. Hsu, N.-Y., Chien, C.-C., Jeng, K.-T. *Appl. Catal.* B **84** (2008) 196.
124. Zhao, Y., Fan, L., Zhong, H., Li, Y., Yang, S. *Adv. Funct. Mater.* **17** (2007) 1537.
125. Kitchin, J.R., Nørskov, J.K., Bareau, M.A., Chen, J.G. *J. Chem. Phys.* **120** (2004) 10240.
126. Wang, D., Xie, T., Li, Y. *Nano Res.* **2** (2009) 30 - 46.
127. Sun, S., Anders, S., Thomson, T., Baglin, J.E.E., Toney, M.F., Hamann, H.F., Murray, C.B., Terris, B.D. *J. Phys. Chem.* B **107** (2003) 5419.

128. Vasquez, Y., Luo, Z., Schaak, R.E. *J. Am. Chem. Soc*. **130** (2008) 11866.
129. Leonard, B.M., Bhuvanesh, N.S.P., Schaak, R.E. *J. Am. Chem. Soc*. **127** (2005) 7326.
130. Vasquez, Y., Sra, A.K., Schaak, R.E. *J. Am. Chem. Soc*. **127** (2005) 12504.
131. Sra, A.K., Schaak, R.E. *J. Am. Chem. Soc*. **126** (2004) 6667.
132. Lim, B., Wang, J., Camargo, P.H.C., Cobley, C.M., Kim, M.J., Xia, Y. *Angew. Chem. Int. Ed.* **48** (2009) 6304.
133. Xie, J., Peng, S., Brower, N., Pourmand, N., Wang, S.X., Sun, S. *Pure Appl. Chem.* **78** (2006) 1003 - 1014.
134. Sun, S., *Adv. Mater.* **18** (2006) 393.
135. Chen, M., Kim, J., Liu, J.P., Fan, H., Sun, S. *J. Am. Chem. Soc.* **128** (2006) 7132.
136. Chen, M., Liu, J.P., Sun, S. *J. Am. Chem. Soc.* **126** (2004) 8394.
137. Robinson, I., Zacchini, S., Tung, L.D., Maenosono, S., Thanh, N.T.K. *Chem. Mater.* **21** (2009) 3021.
138. Rutledge, R.D., Morris, W.H., Wellons, M.S., Gai, Z., Shen, J., Bentley, J., Wittig, J.E., Lukehart, C.M. *J. Am. Chem. Soc.* **128** (2006) 14210.
139. Park, J., Joo, J., Kwon, S.G., Jang, Y., Hyeon, T. *Angew. Chem. Int. Ed.* **46** (2007) 4631 - 4656.
140. Mazumder, V., Chi, M.F., More, K.L., Sun, S.H. *J. Am. Chem. Soc.* **132** (2010) 7848.
141. Wang, C., Peng, S., Chan, R., Sun, S. *Small* **5** (2009) 567.
142. Peng, Z., Yang, H. *J. Am. Chem. Soc.* **131** (2009) 7542.
143. Ding, Y., Fan, F., Tian, Z., Wang, Z.L. *J. Am. Chem. Soc.* **132** (2010) 12480.
144. Lim, B., Jiang, M., Yu, T., Camargo, P.H.C., Xia, Y. *Nano Res*. **3** (2010) 69.
145. Cho, E.C., Camargo, P.H.C., Xia, Y. *Adv. Mater.* **22** (2010) 744.
146. Peng, X.G., *Adv. Mater.* **15** (2003) 459.
147. Roduner, E., Nanoscopic Materials: *Size-dependent Phenomena;* RSC Publishing, 2006.
148. Skrabalak, S.E., Chen, J., Sun, Y., Lu, X., Au, L., Cobley, C.M., Xia, Y. *Acc. Chem. Res.* **41** (2008) 1587 - 1595.
149. Lu, X., Chen, J., Skrabalak, S.E., Xia, Y. *Proc. Inst. Mech. Eng. N.* **221** (2008) 1 - 16.
150. Cobley, C.M., Xia, Y. *Mater. Sci. Eng., R* **70** (2010) 44 - 62.
151. Xia, X., Wang, Y., Ruditskiy, A., Xia, Y. *Adv. Mater.* **25** (2013) 6313 - 6333.
152. Mandal, S., Krishnan, K.M. *J. Mater. Chem.* **17** (2007) 372.
153. Lu, Y., Zhao, Y., Yu, L., Dong, L., Shi, C., Hu, M.J., Xu, M.J., Wen, L.P., Yu, S.H. *Adv. Mater.* **22** (2010) 1407.
154. Sun, Y., Xia, Y. *J. Am. Chem. Soc*. **126** (2004) 3892.
155. Sun, Y., Wiley, B., Li, Z.Y., Xia, Y. *J. Am. Chem. Soc*. **126** (2004) 9399.
156. Dursun, A., Pugh, D., Corcoran, S. *J. Electrochem. Soc.* **150** (2003) B355 - B360.
157. Greeley, J., Norskov, J. *Electrochim. Acta* **52** (2007) 5829 - 5836.
158. Reetz, M.T., Helbig, W. *J. Am. Chem. Soc.* **116** (1994) 7401.
159. Reetz, M.T., Quaiser, S.A. *Angew. Chem. Int. Ed. Engl.* **34** (1995) 2240.
160. Reetz, M.T., Helbig, W., Quaiser, S.A. *Chem. Mater.* **7** (1995) 2227.
161. Ravishankar, N., *J. Phys. Chem. Lett.* **1** (2010) 1212 - 1220.
162. Schmid, G., Lehnert, A., Malm, J.-O., Bovin, J.-O. *Angew. Chem. Int. Ed. Engl.* **30** (1991) 874.
163. Harada, M., Asakura, K., Toshima, N. *J. Phys. Chem.* **98** (1994) 2653.
164. Voyles, P.M., Muller, D.A., Grazul, J.L., Citrin, P.H., Gossmann, H.-J.L. *Nature* **416** (2002) 826.
165. Cazayous, M., Langlois, C., Oikawa, T., Ricolleau, C., Sacuto, A. *Phys. Rev.* B **73** (2006) 113402.
166. Avoyan, A., Rupprechter, G., Eppler, A.S., Somorjai, G.A. *Top catal.* **10** (2000) 107.
167. Yonezawa, T., Toshima, N. *J. Chem. Soc., Faraday Trans.* **91** (1995) 4111.
168. Toshima, N., Yonezawa, T., Harada, M., Asakura, K., Iwasawa, Y. *Chem. Lett.* (1990) 815.
169. Maier-Borst, M., Cameron, D.B., Rokni, M., Parks, J.H. *Phys. Rev.* A **59** (1999) R3162.
170. Renouprez, A.J., Lebas, K., Bergeret, G., Rousset, J.L., Delichere, P. *Stud. Surf. Sci. Catal.* **101** (1996) 1105.
171. Russell, A.E., Rose, A. *Chem. Rev.* **104** (2004) 4613.

172. Torigoe, K., Esumi, K. *Langmuir* **9** (1993) 1664.
173. Touroude, R., Girard, P., Maire, G., Kizling, J., Boutonnet- Kizling, M., Stenius, P. *Colloids Surf.* **67** (1992) 9.
174. Husein, M.M., Nassar, N.N. *Curr. Nanosci.* **4** (2008) 370 - 378.
175. Colak, L., Hadjipanayis, G.C. *Nanotechnol.* **20** (2009) 485602.
176. Ung, D., Tung, L.D., Caruntu, G., Delaportas, Alexandrou, I., Prior, I.A., Thanh, N.T.K. *CrystEngComm.* **11** (2009) 1309 - 1316.
177. Niu, Z., Peng, Q., Gong, M., Rong, H., Li, Y. *Angew. Chem. Int. Ed.* **50** (2011) 6315 - 6318.
178. Mazumder, V., Sun, S. *J. Am. Chem. Soc.* **131** (2009) 4588.
179. Lim, S.I., Ojea~Jiménez, I., Varon, M., Casals, E., Arbiol, J., Puntes, V. *Nano Lett.* **10** (2010) 964 - 972.
180. Murray, C.B., Kagan, C.R., Bawendi, M.G. *Annu. Rev. Mater. Sci.* **30** (2000) 545 - 605.
181. Zhong, X., Feng, Y., Lieberwirth, I., Knoll, W. *Chem. Mater.* **18** (2006) 2468 - 2471.
182. Ozin, G.A., Arsenault, A.C. Nanochemistry: *A Chemical Approach to Nanomaterials;* RSC Publishing, 2005.
183. Peng, Z.A., Peng, X. *J. Am. Chem. Soc.* **123** (2001) 183.
184. Qu, L., Peng, Z.A., Peng, X. *Nano Lett.* **1** (2001) 333.
185. Ott, L.S., Finke, R.G. *Coord. Chem. Rev.* **251** (2007) 1081.
186. Li, Y., El-Sayed, M.A. *J. Phys. Chem.* B **105** (2001) 8938 - 8943.
187. Narayanan, R., El-Sayed, M.A. *J. Phys. Chem.* B **108** (2004) 5726.
188. Teranishi, T., Miyake, M. *Chem. Mater.* **10** (1998) 594.
189. Breiter, M.W., In Handbook of Fuel Cells: Fundamentals: *Technology and Applications;* Wiley, 2003.
190. Narayanan, R., El-Sayed, M.A. *J. Am. Chem. Soc.* **125** (2003) 8340.
191. Narayanan, R., El-Sayed, M.A. *J. Am. Chem. Soc.* **126** (2004) 7419.
192. Narayanan, R., El-Sayed, M.A. *Nano Lett.* **4** (2004) 1343.
193. Meguro, K., Nakamura, Y., Hayashi, Y., Torizuka, M., Esumi, K. *Bull. Chem. Soc. Jpn.* **61** (1988) 347.
194. Semagina, N.V., Bykov, A.V., Sulman, E.M., Matveeva, V.G., Sidorov, S.N., Dubrovina, L.V., Valetsky, P.M., Kiselyova, O.I., Khokhlov, A.R., Stein, B., Bronstein, L.M. *J. Molec. Catal. A: Chem.* **208** (2004) 273.
195. Lu, Z., Liu, G., Phillips, H., Hill, J.M., Chang, J., Kydd, R.A. *Nano Lett.* **1** (2001) 683.
196. Bronsten, L.M., Chernyshov, D.M., Volkov, I.O., Ezernitskaya, M.G., Valetsky, P.M., Matveeva, V.G., Sulman, E.M. *J. Catal.* **196** (2000) 302.
197. Sulman, E., Bodrova, Y., Matveeva, V., Semagina, N., Cerveny, L., Kurtc, V., Bronsten, L., Platonova, O., Valetsky, P. *Appl. Catal. A: Gen.* **176** (1999) 75.
198. Mevellec, V., Roucoux, A., Ramirez, E., Philippot, K., Chaudret, B. *Adv. Synth. Catal.* **346** (2004) 72.
199. Schulz, J., Roucoux, A., Patin, H. *Chem. Eur. J.* **6** (2000) 618.
200. Lin, Y., Finke, R.G. *J. Am. Chem. Soc.* **116** (1994) 8335.
201. Yonezawa, T., Toshima, N., Wakai, C., Nakahara, M., Nishinaka, M., Tominaga, T., Nomura, H. *Coll. Surf. A: Physicochem. Engin. Asp.* **169** (2000) 35.
202. Cheng, W.L., Dong, S.J., Wang, E.K. *Langmuir* **19** (2003) 9434 - 9439.
203. Esumi, K., Isono, R., Yoshimura, T. *Langmuir* **20** (2004) 237.
204. Pittelkow, M., Moth-Poulsen, K., Boas, U., Christensen, J.B. *Langmuir* **19** (2003) 7682.
205. Hayakawa, K., Yoshimura, T., Esumi, K. *Langmuir* **19** (2003) 5517.
206. Crooks, R.M., Zhao, M., Sun, L., Chechik, V., Yeung, L.K. *Acc. Chem. Res.* **34** (2001) 181.
207. Yeung, L.K., Crooks, R.M. *Nano Lett.* **1** (2001) 14.
208. Esumi, K., Suzuki, A., Aihara, N., Usui, K., Torigue, K. *Langmuir* **14** (1998) 3157.
209. Astruc, D., Lu, F., Aranzaes, J.R. *Angew. Chem. Int. Ed.* **44** (2005) 7852 - 7872.
210. Schmid, G., Pfeil, R., Boese, R., Bandermann, F., Meyer, S., Calis, G.H.M., van der Velden, J.A.W. *Chem. Ber.* **114** (1981) 3634.
211. Amiens, C., de Caro, D., Chaudret, B., Bradley, J.S. *J. Am. Chem. Soc.* **115** (1993) 11638.
212. Duteil, A., Schmid, G., Meyer-Zaika, W. *J. Chem. Soc. Chem. Commun.* **31** (1996).
213. Chen, S., Kimura, K. *J. Phys. Chem.* B **105** (2001) 5397.

214. Dassenoy, F., Philippot, K., Ould Ely, T., Amiens, C., Lecante, P., Snoeck, E., Mosset, A., Casanove, M.J., Chaudret, B. *New J. Chem.* **22** (1998) 703.
215. Schmid, G., Morun, B., Malm, J.O. *Angew. Chem. Int. Ed. Engl.* **28** (1989) 778.
216. Schmid, G., Maihack, V., Lantemann, F., Peschel, S. *J. Chem. Soc. Dalton Trans.* (1996) 589.
217. Schmid, G., Emde, S., Maihack, V., Meyer-Zaika, W., Peschel, S. *J. Mol. Catal. A: Chem.* **107** (1996) 95.
218. Wang, D., Li, Y. *Inorg. Chem.* **50** (2011) 5196 - 5202.
219. Sulman, E., Lakina, N., Sulman, M., Ankudinova, T., Matveeva, V., Sidorov, A., Sidorov, S. *Stud. Surf. Sci. Catal.* B **130** (2000) 1787.
220. Andres, R.P., Bielefeld, J.-D., Henderson, J.-I, Janes, D.-B., Kolagunta, V.-R., Kubink, C.-P., Mahoney, W., Osifchin, R.-G., Reifenberger, R. *Science* **273** (1996) 1690.
221. Hirai, H., Yakura, N. *Polym. Adv. Technol.* **12** (2001) 724 - 733.
222. Shon, Y.-S., Chuc, S., Voundi, P. *Coll. Surf. A: Physcochem. Eng. Asp.* **352** (2009) 12 -17.
223. Hwang, C.-B., Fu, Y.-S., Lu, Y.-L., Jang, S.-W., Chou, P.-T., Wang, C.R., Yu, S.J. *J. Catal.* **195** (2000) 336 - 341.
224. Coronado, E., Rebera, A., Garcìa-Martìnez, J., Linares, N., Liz-Marzán, L.M. *J. Mater. Chem.* **18** (2008) 5683.
225. Prabhuram, J., Wang, X., Hui, C.L., Hsing, I.-M. *J. Phys. Chem.* B **107** (2003) 11058.
226. Maye, M.M., Lim, I.-I.S., Luo, J., Rab, Z., Rabinovich, D., Liu, T., Zhong, C.-J. *J. Am. Chem. Soc.* **127** (2005) 1521.
227. Narayanan, R., Lipert, R.J., Porter, M.D. *Anal. Chem.* **80** (2008) 2267.
228. Ullah, M.H., Chung, W.-S., Kim, I., Ha, C.-S. *Small* **2** (2006) 872.
229. Huang, C.-J.W., Y.-H., Chiu, P.-H., Shih, M.-C., Meen, T.-H. *Mater. Lett.* **60** (2006) 1896 - 1900.
230. Petit, C., Taleb, A., Pileni, M.-P. *Adv. Mater.* **10** (1998) 259 - 261.
231. Zhang, J., Han, B., Liu, J., Zhang, X., He, J. Liu, Z., Jiang, T., Yang, G. *Chem. Eur. J.* **8** (2002) 3879 - 3882.
232. Marcianò, V., Minore, A., Liveri, V.T. *Coll. Poly. Sci.* **278** (2000) 250 - 252.
233. Kitchens, C.L., McLeod, M.C., Roberts, C.B. *Langmuir* **21** (2005) 5166 - 5173.
234. Zeng, Q., Jiang, X., Yu, A., Lu, G. *Nanotechnol.* **18** (2007) 1 - 7.
235. Jiang, X., Zeng, Q., Yu, A. *Langmuir* **23** (2007) 2218 - 2223.
236. Yuan, L., Hyodo, T., Shimizu, Y., Egashira, M. *Sensors* **11** (2011) 1261 - 1273.
237. Scott, R.W.J., Datye, A.K., Crooks, R.M. *J. Am. Chem. Soc.* **125** (2003) 3708 - 3709.
238. Niu, Y., Crooks, R.M., *C. R. Chimie* **6** (2003) 1049.
239. Zhang, H.-T., Ding, J., Chow, G.-M. *Langmuir* **24** (2008) 375 - 378.
240. Zhang, J., Fang, J. *J. Am. Chem. Soc.* **131** (2009) 18543 - 18547.
241. Wang, D., Li, Y. *Inorg. Chem.* **50** (2011) 5196 - 5202.
242. Murray, C.B., Norris, D.J., Bawendi, M.G. *J. Am. Chem. Soc.* **115** (1991) 8706.
243. Nur, H., *Akta Kimindo* **3** (2007) 1 - 10.
244. Zaera, F., *Chem. Rec.* **5** (2005) 133 - 144.
245. Corma, A., Garcia, H. *Top Catal* **48** (2008) 8 - 31.
246. Lin, Y., Huber, G.W. *Energy Environ. Sci.* **2** (2009) 68 - 80.
247. Astruc, D., Transition-metal Nanoparticles in Catalysis: *From Historical Background to the State-of-the Art;* Wiley, 2008.
248. Alivisatos, A.P., *Science* **271** (1996) 933 - 937.
249. Somorjai, G.A., Tao, F., Park, J. *Top. Catal.* **47** (2008) 1.
250. Zaera, F., *J. Phys. Chem.* B **106** (2002) 4043 - 4052.
251. Komatsu, T., Inaba, K., Uezono, T., Onda, A., Yashima, T. *Appl. Catal. A: Gen.* **251** (2003) 315.
252. Lang, H., May, R.A., Iversen, B.L., Chandler, B.D. *J. Am. Chem. Soc.* **125** (2003) 14832.
253. Anderson, K., Cortinas Fernandez, S., Hardacre, C., Marr, P.C. *Inorg. Chem. Comm.* **7** (2003) 73.
254. Yang, C., Kalwei, M., Schuth, F., Chao, K. *Appl. Catal. A: Gen.* **254** (2003) 289.
255. Khodakov, A.Y., Bechara, R., Griboval-Constant, A. *Appl. Catal. A: Gen.* **254** (2003) 273.

256. Marchetti, S.G., Cagnoli, M.V., Alvarez, A.M., Bengoa, J.F., Gallegos, N.G., Yeramian, A.A., Mercader, R.C. *Hyperfine Interact.* **139/140** (2002) 33.
257. Balint, I., Miyazaki, A., Aika, K. *Chem. Comm.* **10** (2002) 1044.
258. Balint, I., Miyazaki, A., Aika, K. *J. Catal.* **207** (2002) 66.
259. Miyazaki, A., Balint, I., Aika, K., Nakano, Y. *Chem. Lett.* **12** (2001) 1332.
260. Miyazaki, A., Balint, I., Nakano, Y. *J. Nano Res.* **5** (2003) 69.
261. Yoo, J.W., Hathcock, D.J., El-Sayed, M.A. *J. Catal.* **214** (2003) 1.
262. Yoo, J.W., Hathcock, D.J., El-Sayed, M.A. *J. Phys. Chem.* A **106** (2002) 2049.
263. Balint, I., Miyazaki, A., Aika, K. *Phys. Chem. Chem. Phys.* **6** (2004) 2000.
264. Takasu, Y., Itaya, H., Kawaguchi, T., Sugimoto, W., Murakami, Y. *Stud. Surf. Sci. Catal.* **145** (2003) 279.
265. Nakagawa, K., Yamagishi, M., Nishimoto, H., Ikenaga, N., Suzuki, T., Kobayashi, T., Nishitani-Gamo, M., Ando, T. *Chem. Mat.* **15** (2003) 4571.
266. Li, L., Xing, Y. *J. Phys. Chem.* C **111** (2007) 803.
267. Hsieh, C.-T., Lin, J.-Y. *J. Power Sources* **188** (2009) 347.
268. Konova, P., Naydenov, A., Venkov, Cv., Mehandjiev, D., Andreeva, D., Tabakova, T. *J. Mol. Catal. A: Chem.* **213** (2004) 235.
269. Bowker, M., Stone, P., Bennet, R., Perkins, N. *Surf. Sci.* **511** (2002) 435.
270. Claus, P., Hofmeister, H. *J. Phys. Chem.* B **103** (1999) 2766.
271. Park, K.H., Son, S.U., Chung, Y.K. *Org. Lett.* **4** (2002) 4361.
272. Eppler, A.S., Zhu, J., Anderson, E.A. *Top catal.* **13** (2000) 33.
273. Jacobs, P.W., Wind, S.J., Ribeiro, F.H., Somorjai, G.A. *Surf. Sci.* **372** (1997) L249.
274. Grunes, J., Zhu, J., Anderson, E.A., Somorjai, G.A. *J. Phys. Chem.* B **106** (2002) 11463.
275. Hirai, H., Ohtaki, M., Komiyama, M. *Chem. Lett.* **15** (1986) 269 - 272.
276. Hirai, H., Ohtaki, M., Komiyama, M. *Chem. Lett.* **16** (1987) 149 - 152.
277. Ohtaki, M., Toshima, N., Komiyama, M., Hirai, H. *Bull.Chem. Soc. Jpn.* **63** (1990) 1433.
278. Toshima, N., Ohtaki, M., Teranishi, T. *React. Polym.* **15** (1991) 135.
279. Suzuki, K., Yumura, T., Mizuguchi, M., Tanaka, Y., Chen, C.-W., Akashi, M. *J. Appl. Polym. Sci.* **77** (2000) 2678.
280. Chen, C.-W., Chen, M.-Q., Serizawa, T., Akashi, M. *Chem. Commun.* (1998) 831.
281. Chen, C.-W., Serizawa, T., Akashi, M. *Chem. Mater.* **11** (1999) 1381. .
282. Greci, M.T., Pathak, S., Mercado, K., Prakash, G.K.S., Thompson, M.E., Olah, G.A. *J. Nanosci. Nanotech.* **1** (2001) 3.
283. Chen, C.-W., Serizawa, T., Akashi, M. *Chem. Mater.* **11** (1999) 1381.
284. Garsany, Y., *Anal. Chem.* **82** (2010) 6321 - 6328.
285. Markovic, N.M., Gasteiger, H.A., Ross, P.N. *J. Phys. Chem.* **99** (1995) 3411 - 3415.
286. Markovic, N.M., Gasteiger, H.A., Grgur, B.N., Ross, P.N. *J. Electroanal. Chem.* **467** (1999) 157.
287. Stamenkovic, V., Markovic, N.M., Ross Jr., P.N., *J. Elecroanal. Chem.* **500** (2000) 44.
288. Markovic, N., Gasteiger, H., Ross, P.N. *J. Electrochem. Soc.* **144** (1997) 1591 - 1597.
289. Wanatabe, M., Makita, K., Usami, H., Motoo, S. *J. Electroanal. Chem.* **197** (1986) 195 - 208.
290. Savinell, R.F., Zeller, R.L., Adams, J.A. *J. Electrochem. Soc.* **137** (1990) 489 - 494.
291. Stevens, D.A., Dahn, J.R. *J. Electrochem. Soc.* **150** (2003) A770 - 775.
292. Jerkiewicz, G., Vatankhan, G., Lessard, J., Soriaga, M.P., Park, Y.-S. *Electrochim. Acta* **49** (2004) 1451 - 1459.
293. Will, F.G., *J. Electrochem. Soc.* **112** (1965) 451.
294. Bard, A.J., Faulkner, L.R. Electrochemical Methods: *Fundamentals and Applications;* Wiley, 1980.
295. Damjanovic, A., Dey, A., Bockris, J.O'M. *J. Electrochem. Soc.* **133** (1996) 739.
296. Vetter, K.J., Schultze, J. W. *J. Electroanal. Chem.* **34** (1972) 131.
297. Brett, D.J.L., Atkins, S., Brandon, N.P., Vesovic, V., Vasileiadis, N., Kucernak, A.R. *J. Power Sources* **133** (2004) 205 - 213.
298. Sugimoto, W., Aoyama, K., Kawaguchi, T., Murakami, Y., Takasu, Y. *Electroanal. Chem.* **576** (2005) 215 - 221.
299. Kucernak, A.R., Offer, G.J., *Phys. Chem. Chem. Phys.* **10** (2008) 3699 - 3711.

300. Gasteiger, H.A., Markovic, N., Ross, P.N., Cairns, E.J. *J. Phys. Chem.* **99** (1995) 8290.
301. Schmidt, T.J., Noeske, M.A., Gasteiger, H.A., Behm, R.J., Britz, P., Bönnemann, H. *J. Electrochem. Soc.* **145** (1998) 925.
302. Kuang, Y., Zhang, Y., Cai, Z., Feng, G., Jiang, Y., Jin, C., Luo., J., Sun, X. *Chem. Sci.* (2015) 1 - 8.
303. Rush, B.M., Reimer, J.A., Cairns, E.J. *J. Electrochem. Soc.* **148** (2001) A137 - 148.
304. Santiago, E.I., Batista, M.S., Assaf, E.M., Ticianelli, E.A. *J. Electrochem. Soc.* **151** (2004) A944 - 949.
305. Papageorgopoulos, D.C., de Heer, M.P., Keijzer, M., Pieterse, J.A.Z., de Bruijn, F.A. *J. Electrochem. Soc.* **151** (2004) A763 - 768.
306. Lu, G., Cooper, J.S., McGinn, P.J. *J. Power Sources* **161** (2006) 106 - 114.
307. Gasteiger, H.A., Kocha, S.S., B. Sompalli, B., Wagner, F.T. *Appl. Catal. B: Environ.* **56** (2005) 9 - 35.
308. Huang, X., Zhu, E., Chen, Y., Li, Y., Chiu, C.-Y., Xu, Y., Lin, Z., Duan, X., Huang, Y. *Adv. Mater.* **25** (2013) 2974 - 2979.
309. Kuzume, A., Herrero, E., Feliu, J. M. *J. Electroanal. Chem.* **599** (2007) 333.
310. Paulus, U.A., Schmidt, T.J., Gasteiger, H.A., Behm, R.J. *J. Electroanal. Chem.* **495** (2001) 134 - 145.
311. Mayrhofer, K.J.J., Strmcink, D., Blizanac, B.B., Stamenkovic, V., Arenz, M., Markovic, N.M. *Electrochim. Acta* **53** (2008) 3181.
312. Debe, M.K., Schmoeckel, A.K., Hendricks, S.M., Vernstrom, G.D., Haugen, G.M., Atanasoski, R.T. *ECS Trans.* **1** (2006) 51.
313. Ralph, T.R., Hards, G.A., Keating, J.E., Campbell, S.A., Wilkinson, D.P., Davis, M., St-Pierre, J., Johnson, M.C. *J. Electrochem. Soc.* **144** (1997) 3845 - 3857.
314. Shui, J.-I., Chen, C., Li, J.C.M. *Adv. Funct. Mater.* **21** (2011) 3357 - 3362.
315. Wu, J.F., Yuan, X.Z., Wang, H., Blanco, M., Martina, J.J., Zhang, J. *Int. J. Hydrogen Energ.* **33** (2008) 1735 - 1746.
316. Maillard, F., Schreier, S., Hanzlik, M., Savinova, E.R., Weinkauf, S., Stimming, U. *Phys. Chem. Chem. Phys.* **7** (2005) 385 - 393.
317. http://rsbweb.nih.gov/ij/.
318. Vegard, L., *Z. Phys.* **5** (1921) 17 - 26.
319. Denton, A.R., Ashcroft, N. W. *Phys. Rev. A* **43** (1991) 3161 - 3164.
320. XingLai, C., JiaHao, L., Ye, D., BaiXin, L. *Sci. China. Ser. E-Tech. Sci.* **52** (2009) 2681 - 2687.
321. Mayrhofer, K.J.J., Juhart, V., Hartl, K., Hanzlik, M., Arenz, M. *Angew. Chem. Int. Ed.* **48** (2009) 3529 - 3531.
322. Ciapina, E.D., Santos, S.F., Gonzalez, E.R. *J. Electroanal. Chem.* **644** (2010) 132 - 143.
323. Solla-Gullon, J., Vidal-Iglesias, F.J., Herrero, E., Feliu, J.M., Aldaz, A. *Electrochem. Commun.* **8** (2006) 189 - 194.
324. Wang, X., Li, W., Chen, Z., Waje, M., Yan, M. *J. Power Sources* **158** (2006) 154 - 159.
325. Wilson, M.S., Garzon, F.H., Sickafus, K.E., Gottesfeld, S. *J. Electrochem. Soc.* **140** (1993) 2872 - 2877.
326. Ahrenstorf, K., Heller, H., Kornowski, A., Broekaert, J.A.C., Weller, H. *Adv. Funct. Mater.* **18** (2008) 3850 - 3856.
327. Chen, S., Gasteiger, H.A., Kayakawa, K., Tada, T., Shao-Horn, Y. *J. Electrochem. Soc.* **157** (2010) A82.
328. Yin, Y., Alivisatos, A.P. *Nature* **437** (2005) 664 - 670.